

Measurement of the Top Quark Mass in the Dilepton Channel at the CMS Experiment

by

Aram Avetisyan

M.A., Boston University, 2007

B.A., Harvard University, 2005

Thesis

Submitted in partial fulfillment of the requirements for
the Degree of Doctor of Philosophy
in the Department of Physics at Brown University

Providence, Rhode Island

May 2012

© Copyright
by
Aram Avetisyan
2012

This dissertation by Aram Avetisyan is accepted in its present form by
the Department of Physics as satisfying the
dissertation requirement for the degree of
Doctor of Philosophy

Date
Meenakshi Narain, Advisor

Recommended to the Graduate Council

Date
David Cutts, Reader

Date
Gerald Guralnik, Reader

Approved by the Graduate Council

Date
Peter M. Weber
Dean of the Graduate School

The Vita of Aram Avetisyan

CERN

e-mail: aram.avetisyan@cern.ch

Mailbox L05000

Phone: +41 22 76 76332

CH-1211 Geneve 23

Switzerland

Education

- PhD, Physics, Brown University, Providence, RI 02912 (Expected 2012)
- MA, Physics, Boston University, Boston, MA 02215 (2007)
- BA, Physics, Harvard University, Cambridge, MA 02138 (2005)

Employment

- 2007-Present

Research Assistant

Brown University

Department of Physics

Providence, RI 02912

- 2006-2007

Research Assistant

Boston University

Department of Physics

Boston, MA 02215

- 2005-2006

Teaching Assistant

Boston University

Department of Physics

Boston, MA 02215

Experience

Research

2007-Present: Work on the CMS experiment.

Analysis

- First Measurement of the Top Quark Mass at the LHC: I worked on measuring the top mass in the dilepton channel with the Analytical Matrix Weighting Technique (AMWT). I adapted the AMWT code for use with the CMS software framework and developed several improvements such as giving priority to b-tagged jets when calculating the mass. I also generated simulation samples over a wide range of top masses using MadGraph, prepared them for official production and ran both data and simulation samples on the grid. Furthermore, I implemented the event selection, evaluated the systematics and performed many cross-checks.
- Search for a Heavy Top Partner at the LHC: this was a study in simulation of measuring exotic particles with fractional charge of $5/3$ in the early operation of the LHC. I generated the signal and irreducible backgrounds, processed them through simulation, implemented several means of estimating the background contribution and separating the signal from the background and finally evaluated the integrated luminosity necessary to either discover or set a limit on the existence of these particles.

Detector Work

- The CMS Hadron Calorimeter (HCAL) is a device used to study the properties of jets originating from hadrons and contributes to the measurement of missing transverse energy from particles such as neutrinos. In 2007-2008, I worked on

the logical map for cables connecting the HCAL electronics. I merged several separate maps into a single one, helped design the layout for several components of the outer calorimeter and adjusted the code to conform with the hardware as cabling took place. From 2008 to 2010, I worked on the validation of HCAL software. In addition to running it for every new release of the CMS software framework, I also automated the process, reduced its memory consumption and implemented tools to validate new features of HCAL software as they arose. In 2010, I also worked on the web-based monitoring of HCAL.

- The CMS High Level Trigger (HLT) performs the final selection of LHC events that will be written to storage for physics analysis. I worked on the soft muon triggers used for b-tagging in 2007 and evaluation of the rate for the entire trigger menu in 2008. From 2010 to 2011, I studied the effects of pile-up on rates and timing and also developed a tool for adapting histograms that rely on multiple trigger paths in situations where the HLT prescales change.
- b-tagging: In 2010-2011, I worked on validation of software algorithms that identify jets from bottom quarks. I ran the validation suite for every release and also made some adjustments to automate it.

Teaching

- 2005-2006: I was a teaching assistant at Boston University and taught discussion sections in an introductory physics course for pre-medical students and biology majors.

Skills

- Physics: analysis of complex final states with many types of detector objects
- Programming: C++, ROOT, Python, Java, UNIX shell, SQL

- System administration (Scientific Linux)
- Languages: English, Russian (native), basic Spanish, some French

Contributions to Conferences

- "Measurement of the top mass in pp collisions at 7 TeV" at the LHCC students' poster session, March 2011, Geneva, Switzerland
- "Search for a Heavy Top Partner at the LHC" at DPF, July 2009, Detroit, MI
- "The CMS High-Level Trigger and Trigger Menus" at the APS April Meeting, April 2008, Saint Louis, MO

Selected Publications

- CMS Collaboration, "First measurement of the top quark mass in pp collisions at $\sqrt{s} = 7$ TeV", CMS Physics Analysis Summary CMS-PAS-TOP-10-006 (2011)
- CMS Collaboration, "First measurement of the cross section for top-quark pair production in proton-proton collisions at $\sqrt{s} = 7$ TeV", Phys. Lett. B695 (2011) 424443, arXiv:1010.5994. doi:10.1016/j.physletb.2010.11.058
- CMS Collaboration, "Search for Exotic Top Partners with the CMS Experiment", CMS Physics Analysis Summary CMS-PAS-EXO-08-008 (2009)

Preface and Acknowledgments

I would like to thank my advisor, Meenakshi Narain, for guiding me through the process of becoming a physicist, for a great deal of useful advice and for her kindness and generosity. I would also like to thank Jeremy Andrea, Ulrich Heintz and Thomas Speer for their contributions to the AMWT analysis and for teaching me the requisite experimental techniques. I'd like to thank Thomas in particular for helping me with the writing of the dissertation and for answering my many, many questions. Last, but certainly not least, I would like to thank my parents and my sister for their love and support. This work would not have been possible without them.

Contents

Vita	iv
Preface and Acknowledgments	viii
Contents	ix
List of Tables	xiii
List of Figures	xv
1 The Top Quark	1
1.1 The Standard Model	1
1.1.1 Fermions	2
1.1.2 Interactions and Gauge Bosons	4
1.2 Top Quark Production	6
1.2.1 Single Top	6
1.3 Top Quark Decay	7
1.3.1 Kinematics of Dilepton $T\bar{T}$ Decay Products	8
1.4 Top-Antitop Properties	13
1.4.1 Charge Asymmetry	13
1.4.2 Spin Correlation	15
1.4.3 Helicity of W Bosons	16

1.4.4	Flavor Changing Neutral Currents	17
1.5	Top Quark Mass	18
1.5.1	Indirect Measurements of the Top Quark Mass	18
1.5.2	Degrees of Freedom in $T\bar{T}$ Decays	21
1.5.3	Semi-leptonic Channel	22
1.5.4	Hadronic Channel	23
1.5.5	Dilepton Channel	24
1.5.6	Summary	25
2	The Large Hadron Collider and the Compact Muon Solenoid Experiment	26
2.1	The Large Hadron Collider	26
2.2	Compact Muon Solenoid	29
2.2.1	CMS Coordinate System	29
2.2.2	Magnet	30
2.2.3	Inner Tracking System	30
2.2.4	Electromagnetic Calorimeter	35
2.2.5	Hadron Calorimeter	38
2.2.6	Muon System	41
2.2.7	Trigger	44
3	Data and Simulation Samples	48
3.1	Data	48
3.2	Simulation	49
4	Event Selection and Object Reconstuction	52
4.1	Event Cleaning	52
4.2	Trigger	53
4.3	Muons	55

4.4	Electrons	60
4.5	Dilepton Selection	65
4.6	Jets	67
4.7	Missing Transverse Energy	70
4.8	Event Selection Summary	74
5	Jet Selection	75
5.1	Initial and Final State Radiation	75
5.2	b-tagging	76
6	Event Reconstruction	82
6.1	Event Kinematics	82
6.2	Solution Weighting	83
6.3	Smearing of Jets and Missing ET	85
6.4	Weight Cut	88
6.5	Final Peak Mass Distributions	90
7	Template Fit	92
7.1	Background Estimate	93
7.1.1	The R-in/out Method for the Drell-Yan Background	94
7.1.2	Peak Mass Template for the Drell-Yan Background	96
7.1.3	b-tagging Classification for Drell-Yan	97
7.2	Likelihood	97
7.3	Study of the Method in Simulation	98
7.4	Result with Data	101
8	Systematic Uncertainties	104
8.1	Jet Energy Scale	104
8.1.1	Jet Energy Scale Cross-Check	105

8.2	Other Detector Objects	108
8.2.1	Jet Energy Resolution	108
8.2.2	Lepton Energy Scale	108
8.2.3	Missing Transverse Energy	108
8.2.4	b-tagging	108
8.3	Pile-up	109
8.4	Background	109
8.5	Simulation	110
8.6	Template Fit	111
8.7	Summary	111
9	b-jet Energy Calibration	113
10	Conclusion	115
10.1	Combination	115
10.2	Prospects for the Top Quark Mass at CMS	117
10.3	b-jet Energy Calibration	118
A	Data Events Used to Measure the Mass of the Top Quark	120
	Bibliography	148

List of Tables

1.1	Branching fractions of $t\bar{t}$ decays.	8
2.1	LHC beam parameters.	28
3.1	All data samples used in the analysis.	49
3.2	List of simulated samples used in the analysis.	51
4.1	Complete list of triggers used for the analysis.	54
4.2	Criteria used for electron identification.	62
4.3	Criteria used for jet identification.	69
4.4	Total number of dilepton events after each selection cut.	74
5.1	Fraction of simulated $t\bar{t}$ dilepton events with 0, 1 or 2 matched b -jets according to the choice of jets.	78
5.2	Events after the final selection split by b -tagged multiplicity.	78
7.1	Estimated Drell-Yan background contamination.	95
7.2	Fractions of simulated Drell-Yan events that satisfy the minimum peak weight requirement.	96
7.3	Expected number of events in each sample according to the number of b -tagged jets used.	97
7.4	Expected mean uncertainty from ensemble tests with different methods of event classification.	101

8.1	List of systematic uncertainties with their contribution to the total uncertainty.	112
10.1	Summary of measured top quark masses for the KINb and AMWT methods	117

List of Figures

1.1	The particles of the Standard Model.	2
1.2	Tree-level Feynman diagrams of $t\bar{t}$ production.	6
1.3	Tree-level Feynman diagrams of single top production.	7
1.4	Dilepton decay of a $t\bar{t}$ pair.	9
1.5	Transverse momenta of generator-level leptons.	9
1.6	η of generator-level leptons.	11
1.7	Transverse momenta of generator-level b -jets.	12
1.8	η of generator-level b -jets.	12
1.9	Transverse momenta of radiated jets.	13
1.10	\cancel{E}_T distribution due to generator-level neutrinos	14
1.11	Electroweak fit for the mass of the Higgs boson except for m_t	19
1.12	Dominant Feynman diagrams of B_0 - B_0 bar mixing.	19
1.13	Feynman diagrams of the top quark and electroweak bosons	21
2.1	The CERN Accelerator Complex.	27
2.2	The CMS Detector.	29
2.3	Schematic cross section of the CMS tracker.	31
2.4	Global track reconstruction efficiency for muons and pions.	32
2.5	A sketch of one tracker endcap.	34
2.6	A crystal from the ECAL endcap and its vacuum phototriode.	35

2.7	Layout of the CMS electromagnetic calorimeter.	36
2.8	A quarter view of the four HCAL subdetectors.	38
2.9	A schematic of the HB wedges.	40
2.10	A transverse view of the DT layout.	42
2.11	A CSC chamber.	43
2.12	A longitudinal view of the CSC layout.	44
2.13	A transverse view of the barrel RPCs.	45
4.1	The trajectory of a charged particle in a magnetic field.	56
4.2	Muon p_T distributions.	58
4.3	Muon η distributions.	59
4.4	Muon p_T distributions after the full selection.	59
4.5	Muon η distributions after the full selection.	60
4.6	Electron p_T distributions.	63
4.7	Electron η distributions.	63
4.8	Electron p_T distributions after the full selection.	64
4.9	Electron η distributions after the full selection.	65
4.10	Dilepton invariant mass distributions.	66
4.11	Dilepton invariant mass distributions after the full selection.	66
4.12	Distributions of the numbers of jets.	70
4.13	Jet p_T distributions.	71
4.14	Jet η distributions.	71
4.15	Jet p_T distributions after the full selection.	72
4.16	Jet η distributions after the full selection.	72
4.17	\cancel{E}_T distributions.	73
4.18	\cancel{E}_T distributions after the full selection.	73
5.1	Initial and final state radiation in $t\bar{t}$ events.	75

5.2	Properties of radiated jets.	76
5.3	The decay of a b-hadron at a secondary vertex and the impact parameter of one of the resulting tracks.	77
5.4	Distributions of the numbers of b -tagged jets.	79
5.5	b -tagged jet p_T distributions.	79
5.6	b -tagged jet η distributions.	80
5.7	b -tagged jet p_T distributions after the full selection.	80
5.8	b -tagged jet η distributions after the full selection.	81
6.1	p_T of the neutrino in dilepton $t\bar{t}$ decays.	84
6.2	Distributions of the total weight in top quark candidate events in data.	85
6.3	Peak mass distributions for an input top quark mass of $172 \text{ GeV}/c^2$	86
6.4	The effect of the jet and \vec{E}_T smearing on neutrino momenta.	86
6.5	Distributions of the total weight in $t\bar{t}$ candidate events in data before and after jet and \vec{E}_T smearing.	88
6.6	Distributions of the total weight in data events rejected by the minimum weight requirement.	89
6.7	Distributions of the peak weight versus the peak mass.	89
6.8	Peak mass distributions split by lepton channel.	90
6.9	Peak mass distributions split by b -tagging multiplicity.	90
6.10	The peak mass distribution of all selected events in data and simulation.	91
7.1	Templates for $t\bar{t}$ events generated at different top quark mass values.	93
7.2	Drell-Yan peak mass distribution from data.	96
7.3	Pull distributions for the $172 \text{ GeV}/c^2$ mass point.	99
7.4	Properties of the fit with samples split by lepton channel.	100
7.5	Properties of the fit with samples split by b -tag multiplicity.	100
7.6	Properties of the fit with 100 pb^{-1} and the background left floating.	102

7.7	Properties of the fit with 35 pb^{-1} and the background left floating. . .	102
7.8	Properties of the fit with 100 pb^{-1} and a fixed background.	102
7.9	Properties of the fit with 35 pb^{-1} and a fixed background.	102
7.10	Properties of the fit with 100 pb^{-1} and no background.	102
7.11	Properties of the fit with 35 pb^{-1} and no background.	102
7.12	Distribution of the $-\log(\text{likelihood})$ points for data.	103
7.13	Fit of the data to the templates obtained in the simulation.	103
8.1	Dilepton mass spectrum from events with e^+e^- or $\mu^+\mu^-$	105
8.2	Jet multiplicity (left) and dilepton p_T spectra (right).	106
8.3	Distribution of $\cos(\Delta\phi)$ for events with exactly one jet.	106
8.4	Distributions of $\Delta\phi$ (left) and mean $\Delta\phi$ in bins of dilepton p_T (right).	107
8.5	Values of χ^2 versus jet energy scale factor f_{jes}	107
8.6	The number of vertices in events after the full selection.	110
9.1	Negative logarithm of the likelihood from the fit of templates for $m_t =$ $173.3 \text{ GeV}/c^2$ to data versus jet energy scale α	114

Chapter 1

The Top Quark

1.1 The Standard Model

The Standard Model¹ (SM) of particle physics is a theory that describes all observed elementary particles and three of the four forces through which they interact. These particles can be divided into bosons which have spin 1 and fermions which have spin $\frac{1}{2}$. The bosons mediate the three forces which are comprised of the electromagnetic, strong and weak interactions. The electromagnetic interaction acts through the photon, the strong interaction works via gluons and the weak interaction is mediated by the W^\pm and Z^0 bosons. The strongly interacting fermions are called quarks and the ones which cannot interact strongly are called leptons. All of the SM particles are shown in Figure 1.1.

The Standard Model is not the complete theory of elementary particles and their interactions: it does not include gravity and does not extend to arbitrarily high energy scales. However, it has proven to be remarkably accurate at all energy regimes currently accessible with particle accelerators. The SM correctly predicts properties of elementary particles such as their lifetime and allows us to estimate the cross sections

¹Numerous texts describing the Standard Model have been published and it is common knowledge within the field of particle physics. Therefore, there will be no citations for the basic aspects of the SM in this section. References [1], [2] and [3] can be consulted for details.

Three Generations of Fermions						
	I	II	III			
Mass →	2.5 MeV/c ²	1.29 GeV/c ²	173.3 GeV/c ²	0		
Charge →	$\frac{2}{3}$	$\frac{2}{3}$	$\frac{2}{3}$	0		
Spin →	$\frac{1}{2}$	$\frac{1}{2}$	$\frac{1}{2}$	1		
Name →	u up	c charm	t top	γ photon		
Quarks	5.0 MeV/c ² $-\frac{1}{3}$ d down	100 MeV/c ² $-\frac{1}{3}$ s strange	4.2 GeV/c ² $-\frac{1}{3}$ b bottom	0 0 1 g gluon	Gauge Bosons	
Leptons	0.511 MeV/c ² -1 $\frac{1}{2}$ e electron	105.7 MeV/c ² -1 $\frac{1}{2}$ μ muon	1.777 GeV/c ² -1 $\frac{1}{2}$ τ tau	80.4 GeV/c ² ±1 1 W[±] weak force		
	< 2 eV/c ² 0 $\frac{1}{2}$ ν_e electron neutrino	< 0.19 MeV/c ² 0 $\frac{1}{2}$ ν_μ muon neutrino	< 18.2 MeV/c ² 0 $\frac{1}{2}$ ν_τ tau neutrino	91.2 GeV/c ² 0 1 Z⁰ weak force		

Figure 1.1: The particles of the Standard Model. All fermions also have an anti-particle with opposite charge. Masses are taken from [1] except for the top quark mass which is from [4].

of processes that produce various particles.

1.1.1 Fermions

Leptons

There are three generations of charged leptons: electrons, muons and taus. Each of these includes a negatively charged particle or a positively charged anti-particle for a total of six charged leptons. Furthermore, each of the six has an associated neutrino or anti-neutrino. The latter are electrically neutral and are assumed to be massless in the Standard Model. The observed oscillation of neutrinos between the lepton generations implies that neutrinos have non-zero masses, but since these masses are far smaller than the scale of the energies for this analysis, we use the Standard Model assumption.

The three generations differ only in mass and “lepton number”. The latter is used to describe the conservation of the number of leptons from each generation. Electrons and the associated neutrinos have an electron lepton number of 1 while positrons and the associated anti-neutrinos have an electron lepton number of -1. The same convention holds for the other generations of leptons. Under the assumption of massless neutrinos, the conservation of the three lepton numbers is absolute. Therefore, muons and taus must always emit an associated neutrino when they decay and they can only do so through the weak interaction.

The lifetime of weakly decaying fermions is approximately proportional to m_W^4/m_f^5 where m_W is the mass of the W boson and m_f is the mass of the fermion [3]. The muon has the lowest mass of all unstable SM particles and as a result of this, its mean lifetime is relatively long: $\tau_\mu = 2.2 \times 10^{-6}$ s. This allows relativistic muons to travel through particle detectors without decaying. The neutrinos and the electron are the lightest particles in the Standard Model and are thus stable due to conservation of energy and charge.

Quarks

Quarks are massive fermions with charges that are either $\pm\frac{1}{3}$ or $\pm\frac{2}{3}$ times the charge of the electron. In addition to the electric charge, they also carry one of three “color” charges which allows them to participate in strong interactions. Due to the nature of the strong interaction, free quarks are never observed. Except for the top quark which is discussed in greater detail below, separated quarks form additional quark-antiquark pairs until all of the quarks are bound in color-neutral hadrons. This phenomenon is referred to as “hadronization”.

As with leptons, there are three generations of quarks with two quarks and two antiquarks each. Thus, there is a total of six quark flavors: up, down, strange, charm, bottom and top. Quark flavor is conserved under electromagnetic and strong

interactions, but not under the weak interaction. Unlike leptons, heavier quarks can decay into lighter quarks from other generations via the weak interaction.

1.1.2 Interactions and Gauge Bosons

Electroweak Interactions

One of the main insights of the Standard Model is that the electromagnetic and weak interactions can be combined into a single “electroweak” interaction. This has the symmetry $SU(2) \times U(1)$ and is generated by a triplet of vector fields (referred to as W_μ^1 , W_μ^2 and W_μ^3) and a single vector field (called B_μ). The W_μ^i fields couple to electroweak chiral doublets which consist of the Dirac spinors of fermions or anti-fermions from the same generation. The fields only couple to left-handed fermions or right-handed anti-fermions and the current associated to this coupling is called the weak isospin current. The B_μ field couples to the hypercharge current which is a combination of the W_μ^3 component of the weak isospin and the electric charge.

The electroweak symmetry is spontaneously broken using the Higgs mechanism which results in one massless and three massive gauge bosons:

$$A_\mu = B_\mu \cos \theta_W + W_\mu^3 \sin \theta_W , \quad (1.1a)$$

$$Z_\mu = -B_\mu \sin \theta_W + W_\mu^3 \cos \theta_W , \quad (1.1b)$$

$$W_\mu^\pm = \frac{1}{\sqrt{2}} (W_\mu^1 \mp W_\mu^2) . \quad (1.1c)$$

Here, the massless A_μ corresponds to the photon, Z_μ to the Z^0 boson and W_μ^\pm to the W^\pm bosons. θ_W is the weak mixing angle and is given by $\cos \theta_W = M_W/M_Z$.

In the Standard Model, spontaneous symmetry breaking is accomplished by introducing a Higgs field which has a degenerate ground state. The choice of a particular minimum value around which to do a perturbative expansion breaks the symmetry.

The Higgs field results in a massive Higgs boson (H) with spin 0 and also gives masses to the fermions. However, the Higgs boson has not currently not been observed and there exist extensions of the SM that break the symmetry by other means.

Strong Interactions

As mentioned above, the strong interaction is mediated by gluons and takes place between particles that have color charge. There are three different colors: “red”, “green” and “blue”. Every quark carries a single color or anticolor and every gluon carries one color and one anticolor. Since the gluons themselves have color, a gluon can interact with other gluons as well as with quarks. The symmetry of the strong interaction is SU(3).

Unlike all other interactions, the coupling of the strong interaction is relatively weak at short distances and increases as the interacting particles are separated. The “running coupling constant” of the strong interaction can be written as

$$\alpha_s(q^2) = \frac{12\pi}{(11n - 2n_f) \log(q^2/\Lambda^2)}, \quad (1.2)$$

where q is the momentum of the virtual gluon mediating the interaction, n is the number of quark generations, n_f is the number of quark flavors and Λ is the momentum scale at which this approximation breaks down and the coupling constant becomes large [2]. Λ has been measured to be between 100 and 500 MeV/ c .

The relationship between the distance and momentum scales of the interaction is determined by the uncertainty principle: $d = c\Delta t \gtrsim \hbar/q$. Thus, at distances on the order of the size of the proton, quarks behave as nearly free particles. This phenomenon is known as “asymptotic freedom”. However, the color is confined within hadrons: the separation of colored particles leads to hadronization. The time scale of hadronization is inversely proportional to Λ and is between 10^{-23} and 10^{-24} s.

1.2 Top Quark Production

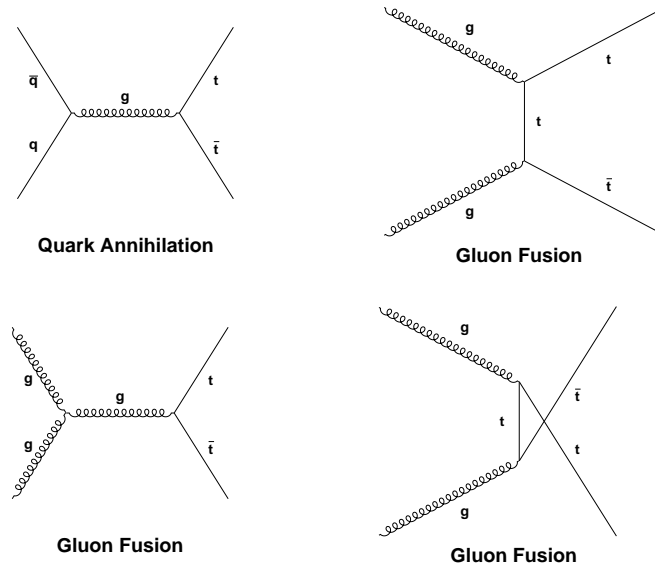


Figure 1.2: Tree-level Feynman diagrams of $t\bar{t}$ production.

The top quark is the most massive Standard Model particle with a mass of approximately $173.3 \text{ GeV}/c^2$ [4]. At hadron colliders, it is predominantly produced in top-antitop quark pairs ($t\bar{t}$) through either gluon fusion or quark annihilation as shown in Figure 1.2. At the Large Hadron Collider (LHC), the dominant mode of $t\bar{t}$ production is gluon fusion: it produces 70% of $t\bar{t}$ pairs at $\sqrt{s} = 7 \text{ TeV}$ [5]. The cross section of $t\bar{t}$ production at $\sqrt{s} = 7 \text{ TeV}$ is $158_{-24}^{+23} \text{ pb}$ when calculated at next-to-leading order [6]. This is consistent with next-to-next-to-leading order calculations [7] and with experimental results [8].

1.2.1 Single Top

Single top quarks produced via the electroweak interaction have also been observed, but this production mode is much more rare. At the Large Hadron Collider, there are three modes of single top production: t-channel, s-channel and tW-channel. The three modes are shown in Figure 1.3. The cross sections of the different modes at

$\sqrt{s} = 7$ TeV are 64.6 pb for the t-channel, 4.21 pb for the s-channel and 10.6 pb for the tW-channel [9].

Single top production in the tW-channel results in two W bosons and a b-quark. It is similar to $t\bar{t}$ except for the latter having an additional b-quark. Since b-quarks are only observed in detectors as jets of particles (see Section 4.6), the extra b-quark can be mimicked by radiated jets and single top in the tW-channel is a background in analyses that study $t\bar{t}$.

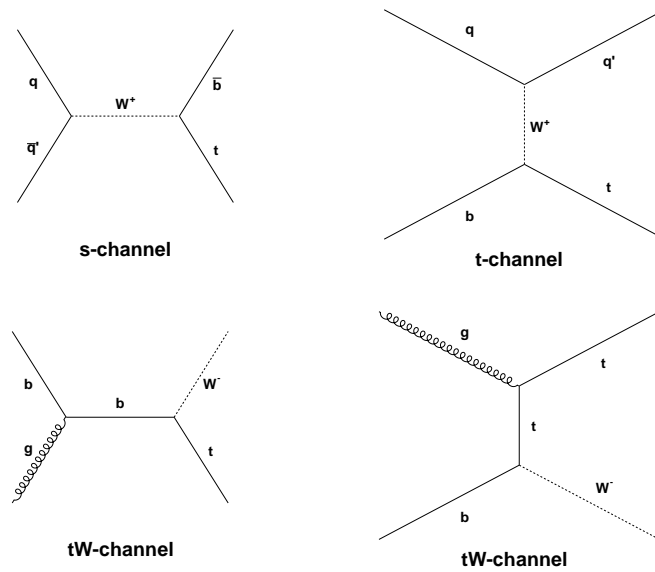


Figure 1.3: Tree-level Feynman diagrams of single top production.

1.3 Top Quark Decay

As noted in Section 1.1.1, the lifetimes of fermions are inversely proportional to the fifth power of their masses. Due to the very large mass of the top quark, it has a decay width $\Gamma_t = 1.99^{+0.69}_{-0.55}$ GeV and thus a lifetime of $(3.3^{+1.3}_{-0.9}) \times 10^{-25}$ s [10]. This is significantly less than the time scale of hadronization (10^{-23} - 10^{-24} s) so top quarks decay before they can hadronize.

The top quark decays almost exclusively to a W boson and a bottom quark and

the $t\bar{t}$ pair decays into $W^+bW^-\bar{b}$. Each W boson can then decay into a muon, electron or tau and an associated neutrino or it can decay into a pair of quarks. We consider a W boson decay leptonic if it results in a muon or an electron. Since tau leptons are about 17 times more massive than muons, they decay within the innermost section of particle detectors. If a tau decays into hadrons, it is difficult to distinguish from other hadronic activity. Therefore, top quark decays into taus are considered leptonic only if the tau decays into a muon or an electron. The probability for a tau to decay leptonically is 0.352 [1].

The $t\bar{t}$ decay channel is determined by the two W bosons: it is hadronic if both decay into quarks, semi-leptonic if exactly one decays leptonically and dilepton if both do so. The decay channels are shown in Table 1.1. In this analysis, we report on the measurement of the mass of the top quark in the dilepton channel. Figure 1.4 shows the decay of a $t\bar{t}$ pair into dileptons. The total branching fraction of this channel is approximately 0.065.

$t\bar{t} \rightarrow W^+bW^-\bar{b}$	$W^- \rightarrow e^- \text{ or } \mu^-$	$W^- \rightarrow \tau^-$	$W^- \rightarrow \textit{hadrons}$
$W^+ \rightarrow e^+ \text{ or } \mu^+$	0.0467	0.0233	0.146
$W^+ \rightarrow \tau^+$	0.0233	0.0117	0.073
$W^+ \rightarrow \textit{hadrons}$	0.146	0.073	0.457

Table 1.1: Branching fractions of $t\bar{t}$ decays. The three lepton flavors are assumed to have the same branching fractions.

1.3.1 Kinematics of Dilepton $t\bar{t}$ Decay Products

Hadron Collider Conventions

At hadron colliders, the momentum of the colliding protons and their constituent partons is almost entirely in the directions of the beams. By convention, the direction of one of the beams is taken to be the z -axis. Because the energy of the colliding hadrons is not equally distributed among their constituent partons, any interaction

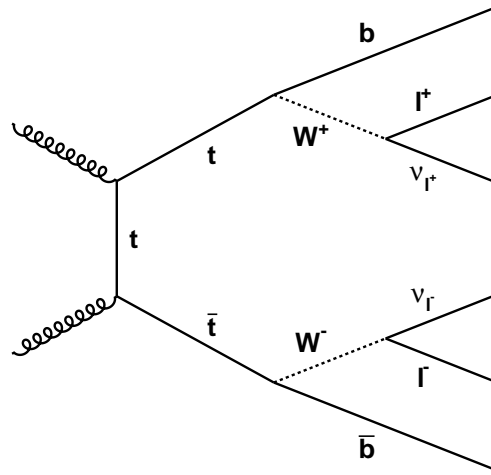


Figure 1.4: Dilepton decay of a $t\bar{t}$ pair.

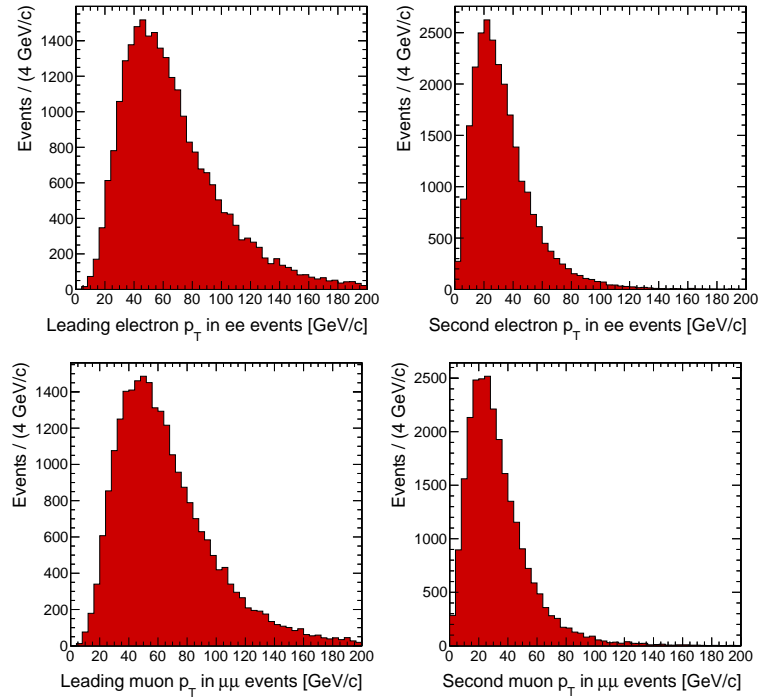


Figure 1.5: Transverse momentum distributions of leptons from $t\bar{t}$ decays. The distributions for the electron leading in p_T (top left), the electron with the lower p_T (top right), the muon leading in p_T (bottom left) and the muon with the lower p_T (bottom right) are shown.

can result in particles with significant momentum along the z -axis. Therefore, only high momenta in the plane transverse to the beam are good indicators of interactions with a large center-of-mass energy. To describe these momenta, we introduce the variables p_T for the transverse momentum and E_T for the transverse energy. We also define the missing transverse energy vector, \vec{E}_T , as the negative of the vector sum of all transverse momenta. The missing transverse energy, \cancel{E}_T , is defined to be the magnitude of \vec{E}_T . Finally, the total transverse energy, H_T , is the scalar sum of all transverse momenta.

The total z -momentum of the colliding partons is not zero, and thus the distribution of minimally biased particles from LHC collisions is not uniform in θ . This property can be recovered by using the rapidity,

$$y = \frac{1}{2} \ln \frac{E + p_z c}{E - p_z c}. \quad (1.3)$$

However, y has the drawback of depending on the mass of the object it describes. To convert it to a polar coordinate, we assume that the mass is negligible compared to the momentum and define the pseudorapidity:

$$\eta = -\ln \left[\tan \left(\frac{\theta}{2} \right) \right]. \quad (1.4)$$

Kinematic Distributions

Dilepton $t\bar{t}$ decays result in two charged leptons, two neutrinos and a $b\bar{b}$ quark pair. To study the properties of these, we use simulated $t\bar{t}$ events with an input top quark mass of $172 \text{ GeV}/c^2$. The events were generated using the MADGRAPH event generator [11] and hadronized using the PYTHIA Monte-Carlo generator [12]. The initial state particles in these events were simulated to be from proton-proton collisions at $\sqrt{s} = 7 \text{ TeV}$ center-of-mass energy.

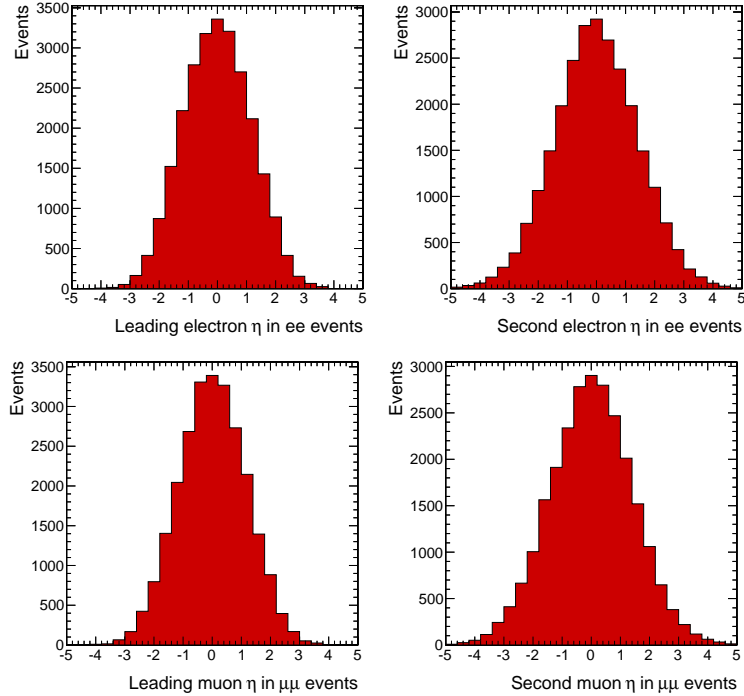


Figure 1.6: η distributions of leptons from $t\bar{t}$ decays. The distributions for the electron leading in p_T (top left), the electron with the lower p_T (top right), the muon leading in p_T (bottom left) and the muon with the lower p_T (bottom right) are shown.

The masses of the quarks and leptons originating from $t\bar{t}$ decays are much smaller than the mass of the top quark. As a result of this, the physics objects from $t\bar{t}$ decays usually have a high p_T and a low $|\eta|$. These properties can be used to distinguish $t\bar{t}$ from other processes that arise from hadron collisions.

The transverse momentum distributions of electrons and muons from $t\bar{t}$ decays are shown in Figure 1.5 and their η distributions are shown in Figure 1.6. These distributions include leptons from $W \rightarrow \tau \rightarrow \ell$ decays. The distributions for electrons and muons are identical except for statistical fluctuations. Since the transverse momentum of the leptons is high, we can use it to distinguish $t\bar{t}$ events from other events in proton collisions. We impose a $p_T > 20$ GeV/ c requirement for all leptons. This eliminates about 29% of dilepton $t\bar{t}$ events, but it reduces the dominant multijet background to negligible levels.

As described in Section 4.6, the quarks hadronize and are only observed in our

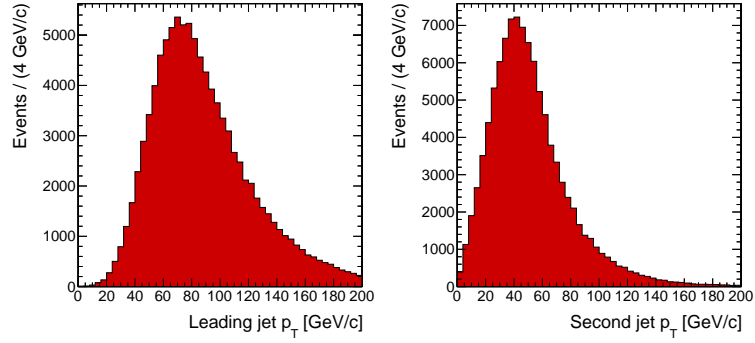


Figure 1.7: Transverse momentum distributions of jets from $t\bar{t}$ decays. The distribution for the jet leading in p_T is shown left and the jet with the lower p_T is on the right.

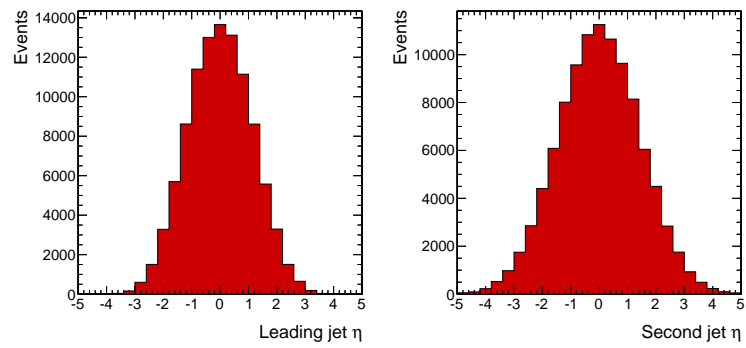


Figure 1.8: η distributions of jets from $t\bar{t}$ decays. The distribution for the jet leading in p_T is shown left and the jet with the lower p_T is on the right.

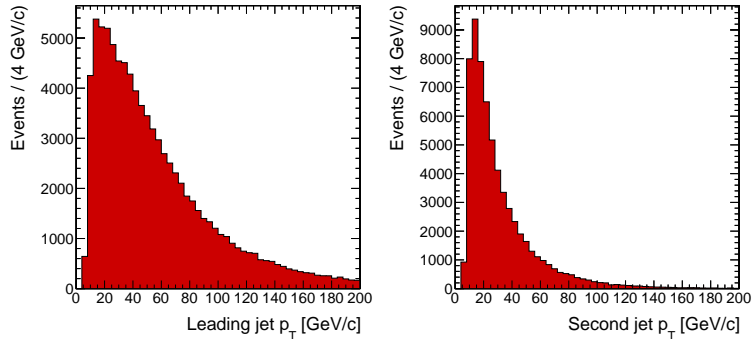


Figure 1.9: Transverse momentum distributions of jets in $t\bar{t}$ events that are due to radiation and do not originate from $t\bar{t}$ decays.

detector as jets of particles. The p_T and η of the two jets from the $b\bar{b}$ pair are shown in Figures 1.7 and 1.8. The b -jets in $t\bar{t}$ decays originate directly from the top or antitop quarks rather than from W bosons so they are more energetic than the leptons. To reduce backgrounds with two leptons such as Drell-Yan production, we impose a $p_T > 30 \text{ GeV}/c$ on all jets.

In addition to the b -jets, $t\bar{t}$ events often have gluon jets that arise from initial or final state radiation. The p_T spectra of these jets are shown in Figure 1.9. The method from distinguishing the b -jets from the radiated jets is described in Chapter 5.

The neutrinos from the $t\bar{t}$ decay escape the detector unobserved and can only be perceived as an imbalance in the transverse energy. This missing transverse energy can be used to distinguish $t\bar{t}$ events from Drell-Yan production. \cancel{E}_T distributions in $t\bar{t}$ events for the three different lepton decay channels are shown in Figure 1.10.

1.4 $t\bar{t}$ Properties

1.4.1 Charge Asymmetry

Due to the contribution of next-to-leading-order Feynman diagrams, $t\bar{t}$ production via quark annihilation is not symmetric in charge. At the Tevatron, this charge asymmetry manifests as a forward-backward asymmetry. This means that the top

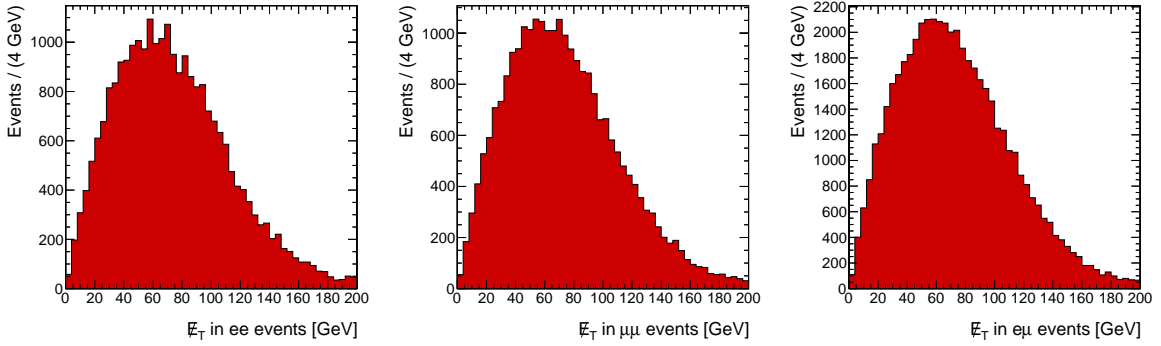


Figure 1.10: The \cancel{E}_T distributions of e^+e^- , $\mu^+\mu^-$ and $e^\pm\mu^\mp$ events in a $t\bar{t}$ sample. Here, the \cancel{E}_T is calculated using generator-level neutrinos.

quark is more likely to fly in the direction of the incoming proton while the antitop tends to go in the direction of the antiproton. DØ [13] and CDF [14] have measured the forward-backward asymmetry by using $\Delta y = y_t - y_{\bar{t}}$ where y is the rapidity. The forward backward asymmetry is defined as

$$A_{fb} = \frac{N^{\Delta y > 0} - N^{\Delta y < 0}}{N^{\Delta y > 0} + N^{\Delta y < 0}}. \quad (1.5)$$

where N is the number of events with the specified property of y .

DØ and CDF make different assumptions when measuring A_{fb} so their results are not directly comparable, but both observe an asymmetry that is larger than the prediction of the Standard Model. This could be an indication of new physics such as a new mediating particle or a particle that decays into the top quark. The latest result from DØ is $A_{fb} = (8 \pm 4(stat) \pm 1(syst))\%$ and it can be compared to DØ's Standard Model expectation of $A_{fb}^{SM} = (1_{-2}^{+1}(syst))\%$ [15]. The current CDF result is $A_{fb} = (15.0 \pm 5.0(stat) \pm 2.4(syst))\%$ whereas CDF's SM prediction is $A_{fb}^{SM} = (3.8 \pm 0.6(syst))\%$ [16].

The LHC is a proton-proton collider so the initial state is symmetric along the direction of the beam and there is no forward-backward asymmetry. However, since the quarks in the collision are usually valence quarks whereas the antiquarks are sea

antiquarks, these two types of partons have different average momenta. This results in a broader rapidity distribution for top quarks relative to that of antitop quarks. The difference can be observed by considering the distribution of $\Delta(y^2) = y_t^2 - y_{\bar{t}}^2$ or by using the variation in the magnitude of the pseudorapidity: $\Delta|\eta| = |\eta_t| - |\eta_{\bar{t}}|$. The charge asymmetry is then

$$A_C = \frac{N^+ - N^-}{N^+ + N^-}. \quad (1.6)$$

where N^+ corresponds to the number of events for which the relevant parameter is positive and N^- is the number of events for which it is negative. The dominant mechanism of $t\bar{t}$ production at the LHC is gluon fusion so the charge asymmetry is expected to be much smaller than at the Tevatron. Current LHC measurements are consistent with Standard Model, but since the effect is so small, it will take significantly more integrated luminosity to confirm or refute the Tevatron results [17].

1.4.2 Spin Correlation

The spins of the top and antitop quarks are expected to be correlated and this correlation should propagate through the weak interaction to their decay products. The absence of such a correlation could be an indication of physics beyond the Standard Model. Currently, the most accurate measurement of spin correlation observes a correlation strength of 0.57 ± 0.31 and excludes the hypothesis that the spins are uncorrelated at the 97.7% confidence level [18].

This measurement was performed using the “matrix element method” which determines the probability of the spins being correlated by integrating over the phase space of the initial and final states. This probability can be approximated as

$$P_{t\bar{t}} = \frac{1}{\sigma_{t\bar{t}}A} \int |\mathcal{M}_{t\bar{t}}|^2 d\Phi_6 \frac{f(q_1)f(q_2)}{q_1q_2} dq_1 dq_2 W_D, \quad (1.7)$$

where $\sigma_{t\bar{t}}$ is the cross section of the $t\bar{t}$ process, A is the acceptance of the detector,

$\mathcal{M}_{t\bar{t}}$ is the matrix element, Φ_6 is the phase space of the final six-particle state, q_i are the momenta of the initial state partons, $f(q_i)$ are the parton distributions functions and W_D is the detector transfer function which relates the parton-level final state to the leptons, jets and \vec{E}_T observed in the detector.

The probability is evaluated with the hypothesis of the spins being correlated and again with them being uncorrelated. A discriminant is then defined based on the two probabilities and the correlation strength is extracted using a likelihood fit to distributions of simulated data. These distributions are produced using a Monte-Carlo generator and differ only in the spin correlation of the $t\bar{t}$ quarks. This type of fit is called a “template fit” and it can be used with other top quark properties.

1.4.3 Helicity of W Bosons

As described in Section 1.3, the top quark almost always decays into a W boson and a bottom quark. The W boson from the decay can be in one of three possible helicity states: left-handed, right-handed or longitudinal. In the Standard Model, top quark decays into right-handed W bosons are strongly suppressed and an observation of a larger fraction of these than expected would be evidence of new physics.

The fractions of the three helicity states are labeled f_- (for left-handed), f_+ (right-handed) and f_0 (longitudinal). These fractions have been measured by the CDF [19] and DØ [20] experiments in the dilepton and semi-leptonic $t\bar{t}$ decay channels. Several measurements were performed with a variety of techniques including the matrix element method and template fits which use the helicity angle θ^* . The latter is defined to be the angle between the direction of the top quark and the down type fermion (charged lepton, down quark or strange quark). When the measurements from CDF and DØ are combined, the fractions are determined to be $f_0 = 0.732 \pm 0.081$ and $f_+ = -0.039 \pm 0.045$. These values are consistent with the Standard Model.

1.4.4 Flavor Changing Neutral Currents

Flavor changing neutral currents are interactions which allow a quark to transition to another quark with a different flavor, but the same electric charge. In the Standard Model, decays of the top quark into an up or charm quark and a gluon, photon or Z boson have branching fractions of order 5×10^{-11} , 5×10^{-13} and 10^{-13} respectively [21]. Thus, any observation of such decays would be an indication of physics beyond the Standard Model. No top quark decays via flavor changing neutral currents have been observed, but several experiments have set limits on the various decay modes.

The branching fraction $B(t \rightarrow Zq)$ has been determined to be less than 3.7% by CDF [22] and less than 3.2% by DØ [23]. CDF estimates this fraction by fully reconstructing events that are assumed to have a leptonically decaying Z and a hadronically decaying W (i.e. $t\bar{t} \rightarrow WbZq \rightarrow q\bar{q}'b\ell^+\ell^-q''$) and performing a template fit using the result of a kinematic fit based on the masses of the top quark and the W boson. DØ measures the same parameter by looking at the number of trilepton events in which the W and Z bosons decay leptonically. Experiments at the LHC will eventually be able to make significant improvements to this limit. With 10 fb^{-1} of integrated luminosity at a center-of-mass energy of 14 TeV, it will be possible to constrain $B(t \rightarrow Zq)$ to approximately 10^{-3} [21].

Due to the much larger backgrounds of their final states, the $t \rightarrow \gamma q$ and $t \rightarrow gq$ decay modes are more difficult to observe directly than $t \rightarrow Zq$. However, it is possible to estimate their branching fractions by assuming that the couplings associated with the decays are the same as those associated with top quark production. The Zeus and H1 experiments at the HERA collider used limits on the single top quark production cross section in electron-proton collisions to set a limit of 5.9×10^{-3} on $B(t \rightarrow \gamma q)$ [21]. Similarly, the Tevatron experiments used single top quark production to find limits on $B(t \rightarrow gq)$. CDF measures $B(t \rightarrow ug)$ to be less than 3.9×10^{-4} and $B(t \rightarrow cg)$ to be less than 5.7×10^{-3} [24] while DØ measures $B(t \rightarrow ug)$ and $B(t \rightarrow cg)$ to be

less than 2.0×10^{-4} and 3.9×10^{-3} , respectively.

1.5 Top Quark Mass

The mass of the top quark is a fundamental parameter of the Standard Model: it cannot be derived from other parameters and must be determined experimentally. Because the top quark mass is so much larger than that of any other SM particle, it affects the predictions of SM observables and serves as one of the most important inputs to global electroweak fits. As illustrated in Figure 1.11, these fits can use the mass of the top quark to provide constraints on the properties of the Higgs boson. The top quark mass can also be used to constrain hypotheses of physics beyond the Standard Model.

Thus, precise measurement of the top quark mass is important for understanding new physics. Prior to the development of accelerators energetic enough to produce the top quark, limits on its mass could be calculated based on Standard Model observables that depend on the top quark mass. These include the mixing of the $B^0 - \bar{B}^0$ mesons and the properties of the W and Z bosons. The mass of the top quark was first measured simultaneously with the observation of the top quark at CDF [25] and DØ [26] in 1995. Since then, it has been measured with a variety of methods in all $t\bar{t}$ decay channels.

1.5.1 Indirect Measurements of the Top Quark Mass

$B_d^0 - \bar{B}_d^0$ Mixing

Due to the weak interaction, neutral mesons undergo particle-antiparticle mixing [1] as shown in Figure 1.12. In the case of the $B^0 - \bar{B}^0$ mesons, the virtual quarks in the middle of the “box” diagrams of Figure 1.12 can be up quarks, charm quarks or top quarks. However, since the amplitude of the mixing depends on the mass of the

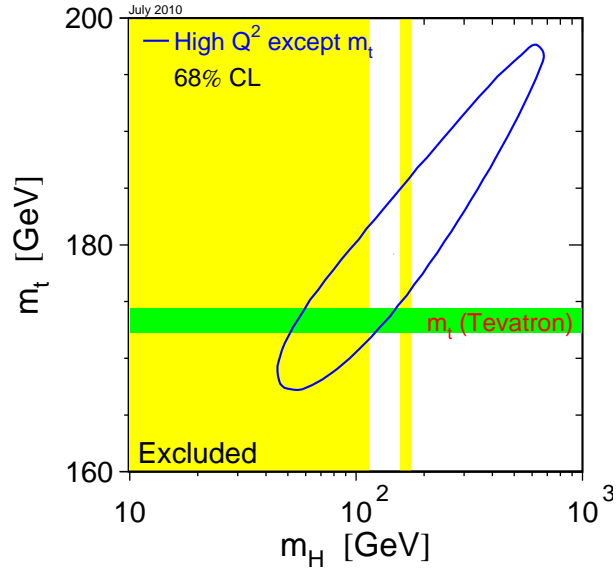


Figure 1.11: The 68% confidence level contour in m_t and the mass of the Higgs boson (m_H) for the fit to all SM data except the direct measurement of m_t . [27]

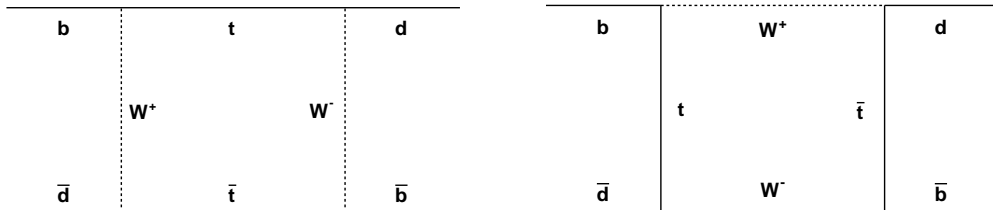


Figure 1.12: Dominant Feynman diagrams of $B_d^0 - \bar{B}_d^0$ mixing.

virtual quarks, the dominant contribution is from the top quark and the rate of the mixing depends on the top quark mass.

$B^0 - \bar{B}^0$ mixing can be observed using events in which the decay products of both mesons include electrons or muons. In the absence of mixing, the two leptons resulting from this process will have opposite signs, but if one of the mesons has oscillated into its anti-particle, the leptons will have the same sign. The ratio of the number of events with a pair of same sign leptons to the number of events with opposite sign leptons can then be used to determine the rate of mixing. This measurement was first performed by the UA1 experiment [28] which did not distinguish between $B_d^0 - \bar{B}_d^0$ and $B_s^0 - \bar{B}_s^0$ mixing. In 1987, the ARGUS experiment used the $\Upsilon(4S)$ resonance to provide unambiguous evidence for $B_d^0 - \bar{B}_d^0$ mixing [29]. The rate of this mixing was larger than expected and this led to a $50 \text{ GeV}/c^2$ lower bound on the top quark mass [30].

Electroweak Fits

The top quark affects the predictions of Standard Model observables via radiative corrections. For example, it contributes to the mass of the W boson via the left diagram of Figure 1.13. The center and right diagrams of Figure 1.13 show its contributions to the $Z \rightarrow b\bar{b}$ decay channel. Thus, the mass of the top quark can be estimated by using the masses and widths of the W and Z bosons, the branching fractions of Z decays into leptons, all quarks and bottom quarks, the weak coupling, and various other parameters of the Standard Model.

The precision of such an estimate is limited because any fit of the electroweak parameters also depends on the mass of the Higgs boson which has yet to be observed. However, the leading dependence of electroweak fits on the mass of the Higgs boson is logarithmic while their leading dependence on the mass of the top quark is quadratic [31]. This allows for a relatively precise determination of the top quark

mass.

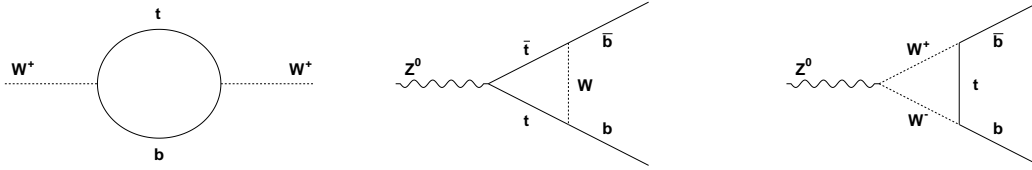


Figure 1.13: Feynman diagrams in which the top quark contributes to the properties of the W (left) and Z (center and right) bosons.

Electroweak fits are usually performed using information from several experiments. In 1994, the combination of electroweak measurements from the LEP, Tevatron and SLC experiments resulted in a top quark mass of $177 \pm 11_{-19}^{+18}$ GeV/ c^2 [32]. The second uncertainty is due to the unknown mass of the Higgs boson.

1.5.2 Degrees of Freedom in $t\bar{t}$ Decays

The methods of measuring the top quark mass in each $t\bar{t}$ decay channel are driven in part by the number of degrees of freedom in the final topology of the decay. It is assumed that the four-momenta of charged leptons and hadrons from the decay are reasonably well measured and that the masses of the final state particles are negligibly small. The neutrinos from leptonic decays escape the detector unobserved so there are three unknown parameters per neutrino. The $t\bar{t} \rightarrow W^+bW^- \bar{b}$ topology yields three constraints: two from the decay products of the two W bosons having the invariant mass M_W and one from the top and antitop quarks having the same mass. Top quarks are currently produced only at hadron colliders so only the momenta of the initial state particles in the plane transverse to the beam are assumed to be zero. The momentum parallel to the beam depends on the distribution of quarks and gluons within the colliding hadrons. It is not known for any given collision because some of the partons comprising the protons continue traveling down the beam pipe. They are not observed by any detector and carry away significant amounts of longitudinal

momentum. Thus, conservation of momentum leads to only two more constraints and the total number of degrees of freedom for any $t\bar{t}$ decay topology is $3n_\nu - 5$ where n_ν is the number of neutrinos.

1.5.3 Semi-leptonic Channel

The most precise measurements of the top quark mass have been made in the semi-leptonic channel. The branching fraction of this channel is approximately 0.35. This is smaller than that of the hadronic decay mode, but the charged lepton reduces both the background and the number of possible jet permutations that can be used when reconstructing the event. There is only one neutrino so the system is over-constrained with -2 degrees of freedom. The $t\bar{t}$ system can be reconstructed, but there are ambiguities which preclude the simple determination of the top quark mass.

As described in Section 4.6, the quarks from the decay are observed in particle detectors as jets. A jet cannot be used to determine the charge of the original quark and ascertaining the quark's flavor based on the jet is difficult (see Section 5.2). As a result of this, the jets observed in the detector cannot be accurately assigned to the final state quarks which causes an ambiguity due to the various permutations. In addition to this, solving for the momentum of the neutrino involves a quadratic equation and thus an ambiguity due to the two solutions.

Multiple methods have been used to determine the top quark mass in the semi-leptonic channel. The first mass measurements solved the $t\bar{t}$ system and used the two extra constraints to perform a kinematic fit for each solution. The top quark mass estimator for each event was taken to be the mass from either the solution with the lowest χ^2 [25] or a weighted mean of several solutions [26]. The top quark mass was extracted using a template fit to distributions of simulated data with different top quark masses.

The largest systematic uncertainty in deriving the top quark mass is due to the

energy scale of jets observed in the detector. In the semi-leptonic channel, this scale can be measured simultaneously with the top quark mass by comparing the invariant mass of the two jets from the hadronically decaying W boson to M_W . This technique was used together with the template method in [33].

The Ideogram method [34] is an extension of this idea. It combines the simultaneous measurement of the jet energy scale with a kinematic fit and a probability function that takes into account the resolution of the top quark mass estimator for each solution. This is accomplished by convoluting a Gaussian function that includes this resolution with a relativistic Breit-Wigner function that represents the average invariant $t\bar{t}$ mass with a given top quark mass.

The top quark mass can also be determined by using the “matrix element method” described in Section 1.4 to evaluate the probability of each $t\bar{t}$ event as a function of the top quark mass. This method was first used in [35] and makes use of all known properties of top quark production and decay. It is more precise than methods which do not include some properties of the phase space, but the evaluation of the integral over many degrees of freedom requires considerable computing resources. To mitigate this requirement, some approximations have to be made to reduce the number of integration variables. For example, the transverse momenta of the incoming partons are assumed to be negligible and the charged lepton momenta are usually assumed to be perfectly measured. The integration can also be evaluated using phase space sampling with the so-called “Dynamic Likelihood Method” [36]. The approximations reduce the amount of computing resources necessary to perform the measurement, but they also reduce the precision of the result.

1.5.4 Hadronic Channel

The hadronic channel has a branching ratio of approximately 0.46 and its final state consists of six jets. Since this final state does not contain neutrinos, there are five

more constraints than there are degrees of freedom. Therefore, the combination of a kinematic fit and the template method described above for the semi-leptonic channel can also be applied to hadronic decays [37, 38]. The Ideogram method has likewise been used [39] and so has a variation of the matrix element method [40].

The hadronic channel does not have any leptons to distinguish it from the multi-jet background that is dominant at hadron colliders. It is the only one of the three $t\bar{t}$ decay modes for which the background is typically larger than the signal. To distinguish the signal from this background, several measurements used neural networks [41, 42]. The hadronic channel also has more possible jet permutations than the other decay channels. To reduce the ambiguity due to these, the above measurements also attempted to distinguish jets originating from b -quarks from other jets (see Section 5.2).

1.5.5 Dilepton Channel

Unlike the over-constrained semi-leptonic and hadronic $t\bar{t}$ decay modes, the dilepton channel is under-constrained. There are two neutrinos and thus one degree of freedom. It is still possible to use the matrix element method in the dilepton channel as in [43] and [44], but the $t\bar{t}$ system cannot be solved without supplying an extra constraint and kinematic fits cannot be performed.

Several variables have been used to perform template fits in order to determine the top quark mass in the dilepton channel. The simplest of these rely on kinematic properties of the final state such as the energy of the b -jets or the invariant mass of lepton-jet pairs [45]. However, the precision of these simple variables is limited. It is possible to get significantly better precision by fully reconstructing each event.

The dilepton $t\bar{t}$ system can be reconstructed by assuming one or more additional constraints. The mass of the top quark can then be estimated by solving the system for a range of the assumed constraints and giving the resulting solutions a weight based

on how likely they are. Multiple algorithms with different constraints have been used to determine the top quark mass this way. The “neutrino weighting algorithm” [46, 47] assumes the pseudorapidities of the neutrino and anti-neutrino and assigns a weight based on how well these agree with the $\vec{\cancel{E}}_T$. A variation of this called the “neutrino ϕ weighting algorithm” [48] uses the azimuthal angle in the plane transverse to the beam rather than the pseudorapidity. The “full kinematic analysis” (KIN) method [48] takes as input the longitudinal momentum of the $t\bar{t}$ system and uses the number of solutions for which the top and antitop masses agree as the weight. The MWT method [46] uses the mass of the top quark itself as the additional constraint and assigns a weight based on the properties of top quark production and decay. A variation of MWT is used in this thesis and it is described in detail in Chapter 6.

1.5.6 Summary

The mass of the top quark has been measured with several different methods. The most precise measured value of the top quark mass is currently $173.3 \text{ GeV}/c^2$ [4] and the most precise published results in the dilepton channel are $m_t = 171.2 \pm 2.7 \text{ (stat)} \pm 2.9 \text{ (syst)} \text{ GeV}/c^2$ for CDF [43] and $m_t = 174.7 \pm 4.4 \text{ (stat)} \pm 2.0 \text{ (syst)} \text{ GeV}/c^2$ for DØ [49]. Up until recently, the mass of the top quark has only been measured at the Tevatron. This thesis describes the first measurement of the top quark mass at the Large Hadron Collider.

Chapter 2

The Large Hadron Collider and the Compact Muon Solenoid Experiment

2.1 The Large Hadron Collider

The Large Hadron Collider is currently the most powerful particle accelerator in the world. It is located at CERN and spans the border between Switzerland and France in the Geneva region. The LHC is designed to collide protons at a center-of-mass energy of 14 TeV, although in its initial stage of operation, the center-of-mass energy is only 7 TeV. This is 3.5 times greater than the energy of Fermilab's Tevatron.

The LHC is situated in a circular tunnel that is 26.7 km in circumference and at a depth of 45 to 170 meters underground. It takes two beams of protons circulating in opposite directions from a chain of smaller accelerators, increases the energy of the protons in each beam up to 3.5 TeV and then collides them at four different locations. There is a dedicated experiment at each of the locations. Two of the experiments, CMS and ATLAS, are general purpose while the other two, ALICE and LHCb, are

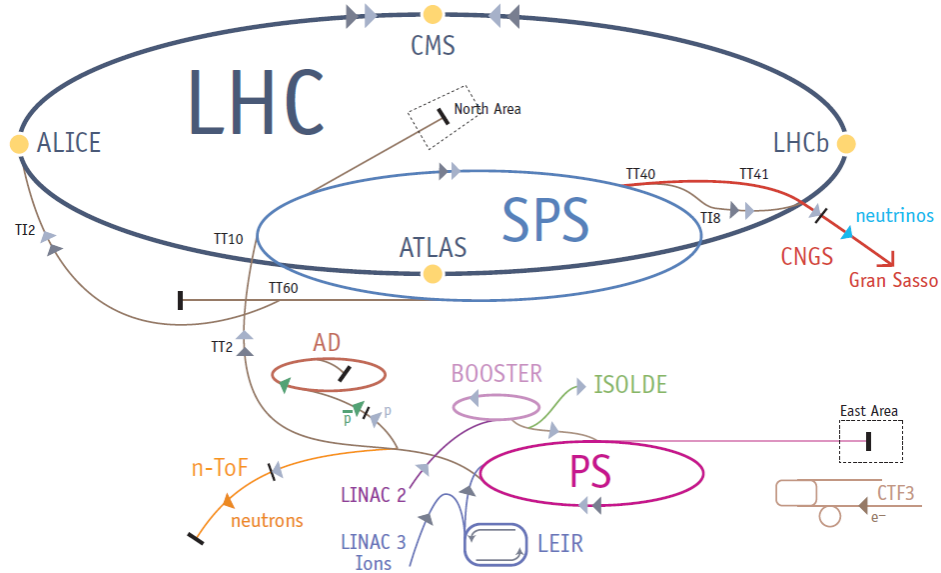


Figure 2.1: The CERN Accelerator Complex. [50]

used to study heavy ion collisions and B-physics respectively.

The LHC accelerator chain and locations of the four experiments are shown in Figure 2.1. The protons used in the LHC are first accelerated to 50 MeV using a linear accelerator (the Linac2). They are then injected into the Proton Synchrotron Booster which accelerates them to 1.4 GeV and sends them to the Proton Synchrotron (PS). The latter accelerates the beams to 25 GeV and feeds them to the Super Proton Synchrotron (SPS) which increases the energy to 450 GeV and passes them to the LHC via the TT12 and TT18 transfer lines as shown in Figure 2.1. The LHC currently accelerates the protons to 3.5 TeV and will eventually take them to 7 TeV.

The rate of events for any process at the LHC is given by:

$$N = \sigma \mathcal{L}, \quad (2.1)$$

where σ is the cross section of the process and \mathcal{L} is the instantaneous luminosity. The

latter depends only on the beam parameters and can be written as:

$$\mathcal{L} = \frac{N_b^2 n_b f_{rev} \gamma_r}{4\pi \epsilon_n \beta^* \sqrt{1 + \frac{\theta_c \sigma_z}{2\sigma^*}}} \quad (2.2)$$

The definitions of the beam parameters and their design values for collisions at the highest luminosity are shown in Table 2.1. At 14 TeV center-of-mass energy, the design luminosity is $10^{34} \text{ cm}^{-2}\text{s}^{-1}$.

Parameter	Meaning	Value
n_b	Number of proton bunches per beam	2808
N_b	Number of protons per bunch	1.15×10^{11}
f_{rev}	Frequency of revolution	11.245 kHz
γ_r	Relativistic gamma of the protons	7461
ϵ_n	Normalized transverse beam emittance	$3.75 \mu\text{m rad}$
β^*	Beta function at the interaction point	55 cm
θ_c	Beam crossing angle	$285 \mu\text{ rad}$
σ_z	RMS longitudinal bunch length	7.55 cm
σ^*	RMS transverse beam size	$16.7 \mu\text{m}$

Table 2.1: LHC beam parameters and their design values for the two general purpose detectors. [51]

The first collisions at the injection energy occurred in November 2009 and the first collisions at 7 TeV took place in March 2010. The data used in this analysis was collected from LHC proton-proton collisions at 7 TeV during all of 2010. As the LHC was being commissioned at this time, the instantaneous luminosity varied widely, reaching a maximum of approximately $2 \times 10^{32} \text{ cm}^{-2}\text{s}^{-1}$ near the end of 2010 operation. The total integrated luminosity delivered by the LHC in 2010 is 46 pb^{-1} and the amount recorded by the CMS experiment and suitable for analysis with the entire detector is 36 pb^{-1} .

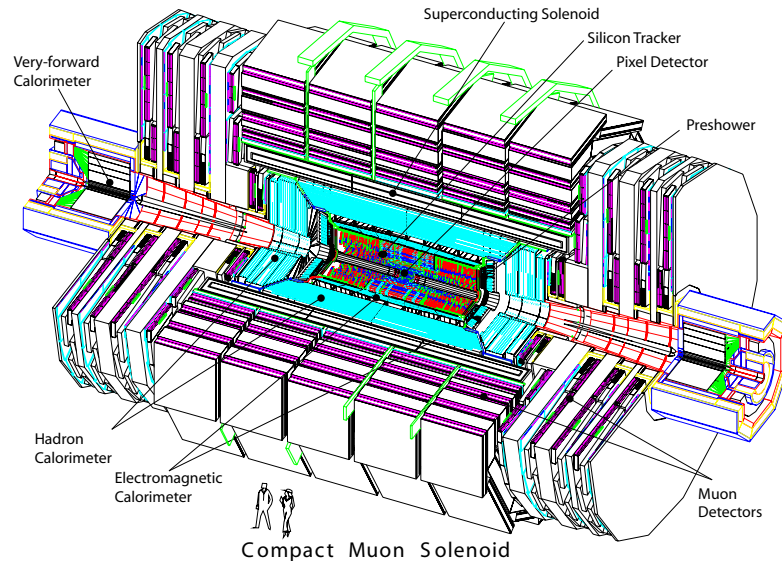


Figure 2.2: The CMS Detector. [52]

2.2 Compact Muon Solenoid

The Compact Muon Solenoid (CMS) experiment is one of the two general purpose detectors at the LHC and consists of several distinct subdetectors used for observing different phenomena. At the center of CMS, the inner tracking system (often referred to as “the tracker”) is used to measure the trajectory of all charged particles. It is surrounded by the electromagnetic calorimeter (ECAL) and the hadronic calorimeter (HCAL) which absorb and measure the energy of jets from electrons, photons and hadrons. All of these systems are inside a superconducting solenoid which generates a 3.8 T magnetic field used to curve the paths of charged particles and allow their momenta to be measured. Muon systems necessary for precise measurement of high energy muons are located in the return yoke of the magnet.

2.2.1 CMS Coordinate System

CMS uses a right-handed coordinate system which has the origin at the nominal collision point in the center of the experiment, the x -axis pointing inward towards

the center of the LHC ring, the y -axis pointing up and the z -axis parallel to the beam pipe. In spherical coordinates, the polar angle θ is measured from the z -axis whereas the azimuthal angle ϕ is measured from the x -axis in the plane transverse to the beam.

2.2.2 Magnet

In order for the tracker to be able to measure the momenta of energetic charged particles, it has to be located in a strong magnetic field. This is accomplished using a superconducting solenoid that was designed to provide a 4 T magnetic field. It currently operates at 3.8 T. The solenoid is 12.5 m long and 6 m in diameter. Its coil is made of NbTi and winds around the cylinder in four layers.

The magnetic flux is returned through a 10000 ton iron yoke made up of five wheels and two endcaps. The iron yoke surrounds the solenoid. The five wheels comprise a barrel which is 13 m long and has an outer radius of 7 m. The endcaps have the same radius as the barrel and each of them is 4 m thick. The iron in the yoke is interspersed with the gas chambers of the muon system.

2.2.3 Inner Tracking System

The inner tracking system of CMS is capable of precisely measuring the trajectories of charged particles and reconstructing the decay positions of particles with long lifetimes such as bottom quarks and taus. At the design luminosity of $10^{34} \text{ cm}^{-2}\text{s}^{-1}$, LHC collisions will result in an average of around 1000 reconstructible charged particles every 25 ns. Hence, the tracking system needs to be able to quickly distinguish multiple particles and also to withstand the radiation from this flux of particles for prolonged periods of time. To accomplish this, the inner tracking system of CMS is comprised entirely of silicon detectors.

Silicon sensors consist of a doped semiconductor in an electric field. As charged

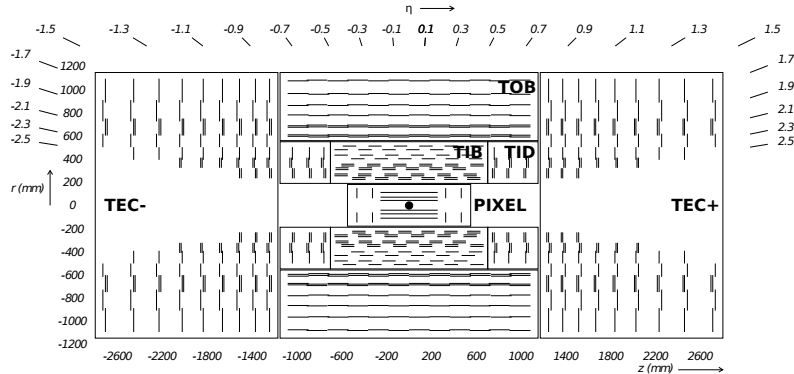


Figure 2.3: Schematic cross section of the CMS tracker. The pixel detector is outlined by the innermost rectangle and the strip tracker is everything outside of that. Each line represents a detector module. Double lines indicate back-to-back modules which deliver stereo hits. [52]

particles pass through the semiconductor, they create electron-hole pairs. The electric field drives these further apart thus inducing a current which is sent to the readout system. The trajectories of charged particles can be measured by using large numbers of such sensors.

CMS has two kinds of silicon detectors: a pixel detector and a strip tracker. As the measurements close to the interaction point are less affected by multiple scattering, they carry more weight in the reconstruction algorithms. Thus, the pixel detector, which has finer granularity, is located close to the beam pipe where the need for resolution is greatest and the occupancy is highest. The strip tracker is further away, where the particle flux is lower. The schematic cross section of the two inner tracking detectors is shown in Figure 2.3.

The pixel detector and strip tracker provide coverage up to $|\eta| = 2.5$ with up to 14 measurement points per track. Within most of this η range, they are capable of reconstructing charged particles with over 90% efficiency and measuring the transverse momentum of particles with $p_T < 100 \text{ GeV}/c^2$ to about 1% resolution. The efficiencies for muons and pions over two orders of magnitude in p_T are shown in Figure 2.4.

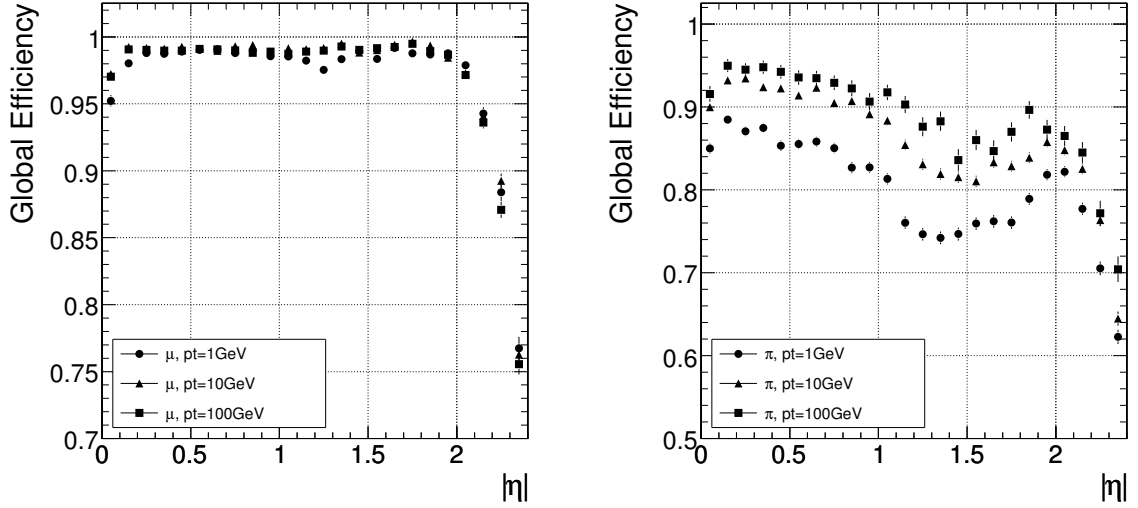


Figure 2.4: Global track reconstruction efficiency for muons (left panel) and pions (right panel) of transverse momenta of 1, 10 and 100 GeV. [52]

Pixel Detector

The pixel detector is situated closest to the interaction point. It is the most important detector for determining the impact parameter used for secondary vertex reconstruction. It consists of three barrel layers and four endcap disks. The barrel layers are 53 cm long cylinders parallel to the beam axis and centered on the interaction point. They have radii of 4.4, 7.3 and 10.2 cm and contain 48 million pixels with an active area of 0.78 m². The endcap disks extend radially from about 6 cm to 15 cm. They are on both sides of the barrel at $|z| = 34.5$ cm and $|z| = 46.5$ cm and cover 0.28 m² with 18 million pixels. The pixel detector covers the pseudorapidity range $|\eta| < 2.5$.

The pixel cells consist of high dose n-implants on a high resistance n-substrate. In order to provide similar resolution in transverse and longitudinal directions, each pixel cell is $100 \times 150 \mu\text{m}^2$ in size. The small size of the cells enables the pixel detector to have low occupancy even in events with high track density. This is particularly important for the identification of jets from tau leptons and bottom quarks. Due to the large number of pixels, the amount of information from every event is more than what can be recorded so the signals they send to the readout are usually zero-

suppressed. This means that only signals above a certain threshold will be read out and these thresholds can be adjusted individually for each pixel.

Strip Tracker

The strip tracker surrounds the pixel detector. It is composed of 15148 detector modules each of which carries either one thin ($320\ \mu\text{m}$) or two thick ($500\ \mu\text{m}$) single sided p-on-n type silicon micro-strip sensors. The thin sensors are used closest to the beam pipe to minimize the amount of material there. The tracker has four subsystems: the Tracker Inner Barrel (TIB), Inner Disks (TID), Outer Barrel (TOB) and End Caps (TEC).

The TIB consists of four cylindrical layers at radii of 0.255, 0.339, 0.419 and 0.498 m from the beam axis. They are centered on the interaction point and each is 1.4 m in length. The two inner layers support double sided modules with a strip pitch of $80\ \mu\text{m}$ whereas the outer two host single sided modules with a strip pitch of $120\ \mu\text{m}$. The double sided modules have silicon sensors mounted back-to-back with a stereo angle of 100 mrad in order to provide measurements of two coordinates simultaneously.

The TID are identical disks enclosing the TIB and spanning a radius from about 0.2 m to 0.5 m centered on the z -axis. Three of them are located on each side of the TIB between 0.8 m and 0.9 m from the interaction point along the z -axis. Each disk is made of three rings of modules. The two inner rings use double-sided modules while outer ring hosts single-sided ones. The TIB and the TID use only $320\ \mu\text{m}$ sensors and provide coverage up to $|\eta| = 2.5$.

The TOB surrounds the TIB and the TID. It consists of six cylindrical layers that are centered on the z -axis and extend 1.18 m from the interaction point in both directions along the z -axis. The layers are located at radii of 60.8, 69.2, 78.0, 86.8, 96.5 and 108.0 cm. The TOB uses $500\ \mu\text{m}$ sensors with double-sided modules in the

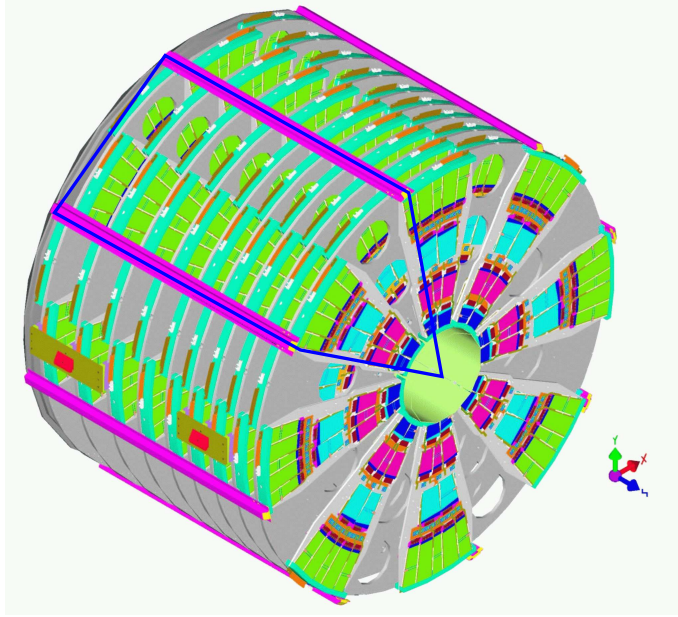


Figure 2.5: A sketch of one tracker endcap with a highlighted sector of petals. Each sector contains nine front petals facing the interaction point and nine back petals mounted on the opposite side of the disk. [52]

two inner layers and single-sided modules in the outer ones.

The TEC encloses the rest of the tracker. It consists of nine disks on each side of the TOB. They extend radially from 0.22 m to 1.14 m and from ± 1.24 m to ± 2.80 m along the beam axis. The modules on the TEC are mounted on sub-structures called petals each of which carries up to seven rings of modules. A drawing of one endcap is shown in Figure 2.5. The inner two rings and the fifth ring from the center use double-sided modules while the rest of the TEC uses single-sided ones. The sensors in the four inner rings are of the thinner, $320 \mu\text{m}$ variety while the ones in the three outer rings are $500 \mu\text{m}$ thick. The TOB and the TEC cover the pseudorapidity range $|\eta| < 2.5$.

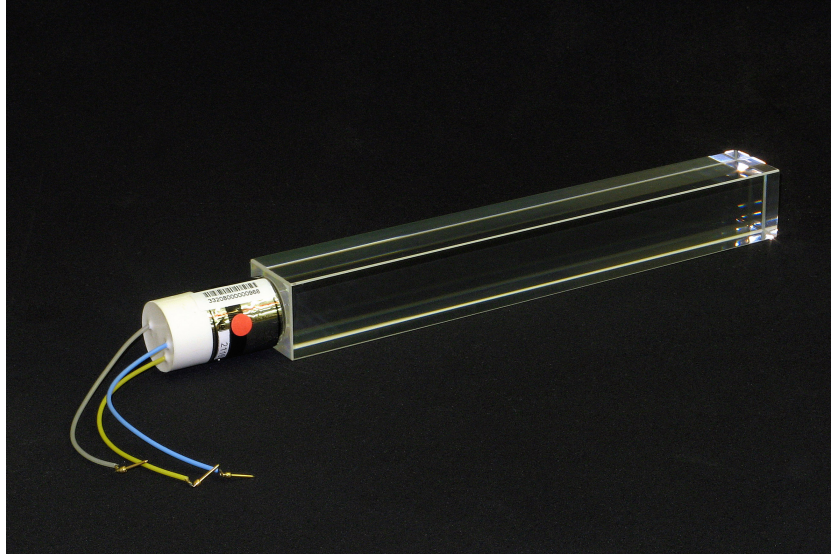


Figure 2.6: A crystal from the ECAL endcap and its vacuum phototriode. [52]

2.2.4 Electromagnetic Calorimeter

The electromagnetic calorimeter of CMS (ECAL) is designed to measure the energy of photons and electrons. It is a hermetic, homogeneous calorimeter made of lead tungstate (PbWO_4) scintillator crystals. These crystals were used because they are radiation resistant, have fine granularity and are fast enough to react to the 25ns bunch crossings of the LHC. They also have a small Moliere radius of 2.2 cm which allows ECAL to be compact and thus fit inside the magnet together with the hadronic calorimeter and the tracker. Furthermore, the radiation length of PbWO_4 , X_0 , is only 0.89 cm so the ECAL thickness is larger than $25 X_0$ at any point. An ECAL crystal is shown in Figure 2.6.

The layout of ECAL is shown in Figure 2.7. ECAL consists of the ECAL Barrel (EB) and the ECAL Endcaps (EE) with a preshower detector positioned in front of the endcaps. It covers the pseudorapidity range $|\eta| < 3.0$. ECAL's energy resolution

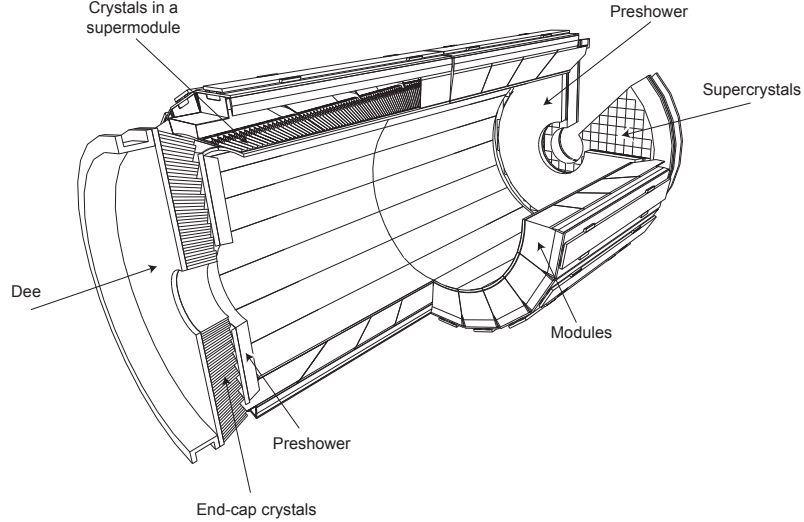


Figure 2.7: Layout of the CMS electromagnetic calorimeter showing the arrangement of crystal modules, supermodules and endcaps, with the preshower in front. [52]

can be parametrized as:

$$\left(\frac{\sigma}{E}\right)^2 = \left(\frac{S}{\sqrt{E}}\right)^2 + \left(\frac{N}{E}\right)^2 + C^2, \quad (2.3)$$

where S is the stochastic term, N the noise term, and C the constant term. In ECAL, the stochastic term originates mainly from fluctuations in the lateral shower containment, from photostatistics and from fluctuations in the energy measured in the preshower detector relative to what is observed. The noise term arises from noise in the electronics and the digitization with a small contribution from pileup at higher luminosities. The constant term is driven by the non-uniformity of the longitudinal light collection, calibration errors and leakage of energy from the back of the crystals. The energy resolution was studied using test beams and was found to be

$$\left(\frac{\sigma}{E}\right)^2 = \left(\frac{2.8\%}{\sqrt{E}}\right)^2 + \left(\frac{0.12}{E}\right)^2 + (0.30\%)^2, \quad (2.4)$$

where E is the energy of the electron or photon in GeV [52].

ECAL Barrel

The ECAL Barrel is composed of 61200 lead tungstate crystals and covers the pseudorapidity range $|\eta| < 1.479$. There are 360 crystals along any circle in ϕ and 170 crystals along any length in the z direction. The cross section of each crystal is approximately 0.0174×0.0174 in $\eta - \phi$.

The crystals are housed in alveolar structures called submodules. The submodule walls are 0.1 mm thick and are made of an aluminium layer facing the crystal and two layers of glass fibre-epoxy resin. Submodules are joined into modules each of which contains 400 or 500 crystals, depending on its position in η . The modules are then assembled into supermodules each of which contains 1700 crystals and is attached to the barrel of the hadronic calorimeter.

In the barrel, the light from the crystals is collected and amplified by avalanche photodiodes (APDs). There are two APDs on the back of each crystal. They read out in parallel and each pair has a mean gain of 50.

ECAL Endcaps

The ECAL endcaps are located on either side of the barrel. Each endcap is 3.15 m away from the interaction point and together they cover the pseudorapidity range $1.479 < |\eta| < 3.0$. The endcap crystals are slightly larger than their barrel counterparts (28.62×28.62 mm² at the front face rather than 22×22 mm²). The 7324 crystals in each endcap are grouped into units of 5x5 crystals called superclusters. Each endcap is made up of 276 standard superclusters and 36 partial superclusters.

The endcaps absorb more radiation than the barrel and APDs are not sufficiently radiation hard for them so vacuum phototriodes (VPTs) are used instead. There is one VPT attached to the back of each crystal. They have a mean gain of 10.2 at zero magnetic field, but this decreases by about a factor of 2 when the CMS magnet is operational.

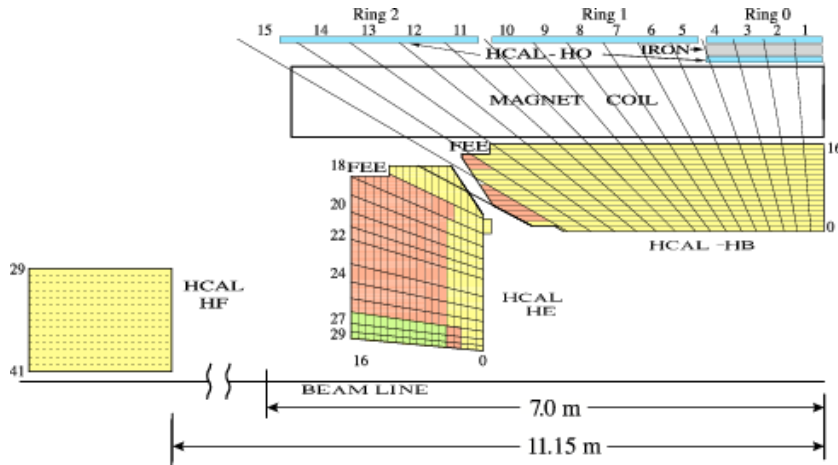


Figure 2.8: A quarter view of the four HCAL subdetectors. [53]

ECAL Preshower

The preshower detector (ES) is a sampling calorimeter which uses layers of lead to initiate the electromagnetic showers and silicon strip sensors to measure the showers' profiles and energies. The preshower is positioned in front of the endcaps. It is used to identify neutral pions within $1.653 < |\eta| < 2.6$ and help identify electrons against minimum ionizing particles.

2.2.5 Hadron Calorimeter

The CMS hadron calorimeter (HCAL) is used to study the kinematic properties of jets from hadrons. A layout of the HCAL subdetectors is shown in Figure 2.8. HCAL consists of four different subdetectors covering the pseudorapidity range $|\eta| < 5$: the barrel (HB), the endcaps (HE), the forward calorimeter (HF) and the outer calorimeter (HO). HB and HE surround ECAL and are located inside the magnet whereas HF and HO are outside of it.

The hadronic energy resolution of HB and the ECAL barrel in front of it can be parametrized as $\sigma/E = S/\sqrt{E} \oplus C$, where S is the stochastic term and C is the constant term. The stochastic and constant terms were measured by using beams of

electrons, muons, pions and protons. In HB, they were found to be $S = 0.847 \pm 0.016 \text{ GeV}^{\frac{1}{2}}$ and $C = 0.074 \pm 0.008$. The resolution is similar in the endcaps and slightly worse in the forward region: the parameters for HF are $S = 1.98 \text{ GeV}^{\frac{1}{2}}$ and $C = 0.09$ [53].

HCAL Barrel

The HCAL Barrel (HB) is a sampling calorimeter composed of brass absorber plates interleaved with plastic scintillator. It extends from an inner radius of 1.8 m to an outer radius of 2.9 m and covers the pseudorapidity range $|\eta| < 1.3$. The absorber consists of 14 brass plates with stainless steel plates on the inside (4 cm thick) and outside (7.5 cm thick) to provide structural support. The 8 brass plates closest to the interaction point are 5.05 cm thick while the other 6 plates are 5.65 cm thick. The total absorber thickness at $|\eta| = 0$ is 5.82 interaction lengths (λ_I) and this increases with polar angle as $1/\sin(\theta)$ up to a maximum of 10.6 λ_I at $|\eta| = 1.3$. In addition, ECAL provides approximately 1.1 λ_I at all η .

The plastic scintillator is divided into 16 η sectors and 18 ϕ wedges which are shown in Figure 2.9. Each wedge is subdivided into 4 azimuthal sectors resulting in an $\eta-\phi$ granularity of 0.087×0.087 . The two layers outside the steel plates are 9 mm thick whereas all the other layers are 3.7 cm thick. The light from the scintillators is sent to a hybrid photodiode (HPD). Each HPD consists of a photocathode held at a high voltage of about 8 kV and a pixelated silicon photodiode. The gain of each HPD is approximately 2000.

HCAL Endcaps

The HCAL Endcaps (HE) cover the pseudorapidity range $1.3 < |\eta| < 3$. Like HB, they are made out of brass absorber plates surrounded by plastic scintillator that sends light to HPDs. All of the brass plates for HE are 7.9 cm thick and, together with

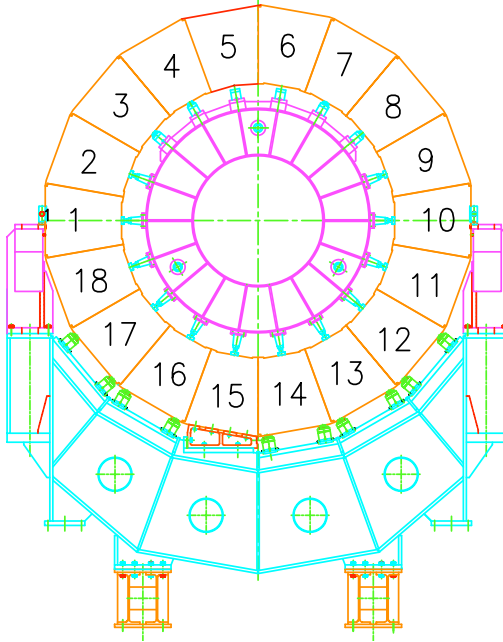


Figure 2.9: A schematic of the HB wedges. Wedge 1 is on the inside of the LHC ring. [52]

ECAL, have a length of about $10 \lambda_I$. The $\eta - \phi$ granularity is 0.087×0.087 for $|\eta| < 1.6$ and 0.17×0.17 for $|\eta| \geq 1.6$.

Outer Calorimeter

The size of the barrel electromagnetic and hadron calorimeters is limited by the radius of the solenoid. As a result of this, their thickness near $|\eta| = 0$ is not sufficient to contain the most energetic jets. The outer calorimeter (HO) uses the return yoke of the magnet and the 19.5 cm thick “tail catcher” iron (labeled “IRON” in Figure 2.8) to provide the extra interaction lengths needed to measure these jets. In the central 2.536 m region of the detector (called Ring 0), HO has two pieces of scintillator on either side of the tail catcher at radial distances of 3.82 m and 4.07 m. In the rest of the $|\eta| < 1.26$ region, there is only one scintillator at 4.07 m. HO has an $\eta - \phi$ granularity of approximately 0.087×0.087 and extends the total length of the calorimeters to a minimum of $10 \lambda_I$.

Forward Calorimeter

The forward calorimeter (HF) is located 11.2 meters from the interaction point and covers the pseudorapidity range $2.9 < |\eta| < 5.2$. It consists of a steel structure made of 5 mm thick grooved plates. Quartz fibers are inserted into the grooves and generate a signal when struck by Cherenkov light produced by charged shower particles. There are two kinds of fibers: long fibers which run the entire 1.65 m length of HF and short fibers which are only 22 cm. The long and short fibres are read out separately which makes it possible to distinguish electromagnetic jets from hadronic ones because only the former deposit a large fraction of their energy in the first 22 cm.

2.2.6 Muon System

As implied by the experiment's middle name, muons are an important tool for the study of interesting processes at the LHC. Samples with isolated muons of high p_T are almost uncontaminated by the dominant multijet background. Furthermore, muons can be measured more precisely than electrons because muons are less affected by radiative losses in the material of the detector. In addition to the tracker, CMS uses three types of gaseous detectors to analyze muons: drift tubes, cathode strip chambers and resistive plate chambers.

The three muon systems cover the pseudorapidity range $|\eta| < 2.4$. For muons with p_T up to about 100 GeV/ c , the p_T resolution is dominated by the tracker. However the muon systems are useful in keeping the resolution of muons with p_T up to 1 TeV/ c at approximately 5%. They are also the only way CMS can trigger on muons because the reconstruction of tracking information is not fast enough to be used at the Level 1 Trigger.

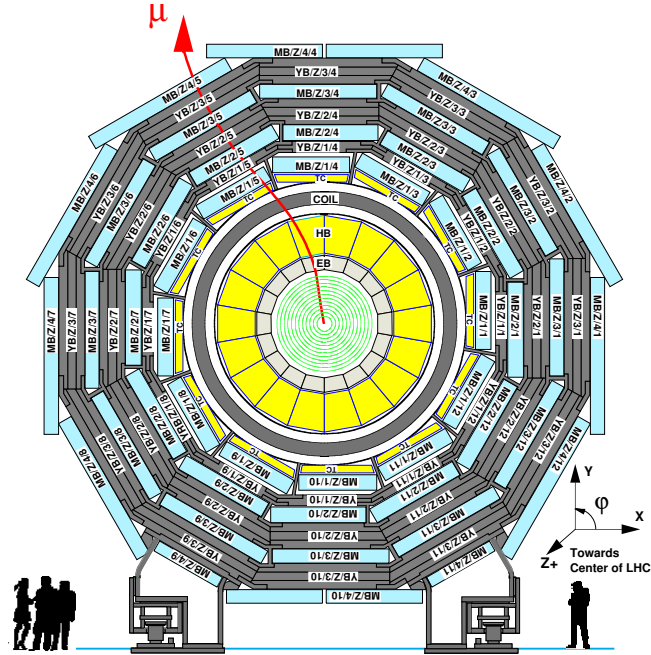


Figure 2.10: A transverse view of the DT layout. DT chambers are shaded in aqua. [52]

Drift Tubes

The Drift Tube system (DT) is made up of tubes filled with a mixture of 85% Ar + 15% CO₂ and a wire held under high voltage. As muons pass through the gas, it becomes ionized. The ions “drift” to the central wire and give rise to an electronic pulse thus allowing the reconstruction of the muon’s path. The length of the wire is 2.4 m and the transverse dimension of the tube is 21 mm.

The DT system is shown in Figure 2.10. It consists of 4 concentric cylindrical layers around the beam axis of which two are embedded in the yoke of the magnet and the other two are on the sides of the yoke. The outer cylinder has 70 drift chambers while the 3 inner ones each have 60. Every DT chamber is comprised of 2 or 3 superlayers each composed of 4 layers of drift tubes. DT uses a total of about 172000 wires and provides coverage up to $|\eta| = 1.2$.

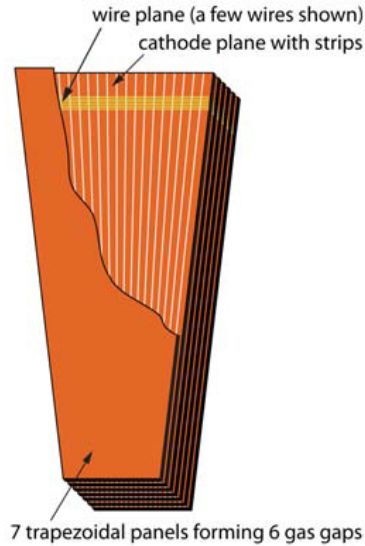


Figure 2.11: A CSC chamber. [52]

Cathode Strip Chambers

The Cathode Strip Chambers (CSC) are multiwire chambers composed of 6 anode wire planes interspersed with 7 cathode panels (see Figure 2.11). The wire planes run azimuthally whereas the cathode panels have strips that run radially. The azimuthal coordinate of muons is found by interpolating the charges induced on the strips by the avalanche of positive ions near a wire.

A longitudinal view of the CSC layout is shown in Figure 2.12. There are 468 CSCs located on the two endcaps. They are trapezoidal and cover either 10° or 20° intervals in ϕ . To provide, contiguous coverage, all chambers overlap either with other CSCs or with DT chambers in the barrel. The CSCs cover the pseudorapidity range $0.9 < |\eta| < 2.4$.

Resistive Plate Chambers

The Resistive Plate Chambers (RPCs) consist of double-gap modules in which the two gaps are filled with gas and have a single read-out strip in between them. The

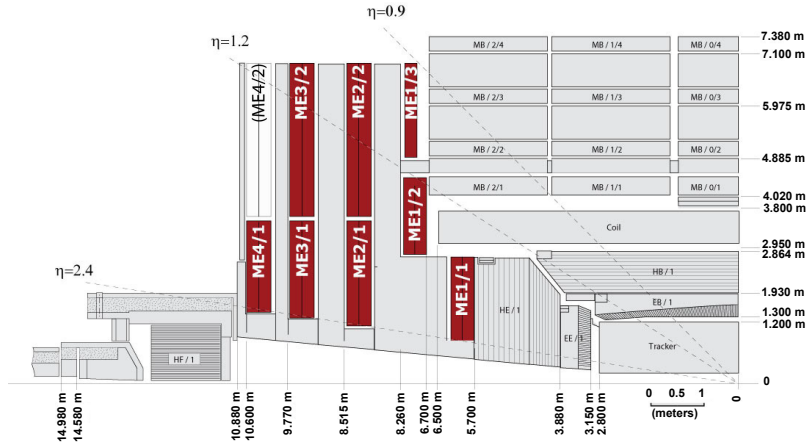


Figure 2.12: A longitudinal view of the CSC layout. CSC chambers are shaded in red. [52]

signal from the two gaps is summed. The gaps are operated in avalanche mode: the electric field across the gaps is reduced to keep the gas amplification low. This creates a need for further amplification at the front-end, but it also improves the speed by more than an order of magnitude. The timing resolution of the RPCs is about 1 ns which makes it ideal for distinguishing bunch crossings when triggering on muons.

The RPCs are located both in the barrel and on the endcaps and cover the pseudorapidity range $|\eta| < 1.6$. The 480 rectangular RPCs in the barrel form 6 cylinders centered on the beam axis. A transverse view of the barrel RPCs is shown in Figure 2.13. The RPCs on the endcaps are trapezoidal and are arranged in 3 rings.

2.2.7 Trigger

At design luminosity, the LHC will collide proton bunches every 25 ns with each collision resulting in an average of 20 proton-proton interactions. The total amount of data from all of these is several orders of magnitude larger than what can be stored for later offline analysis and thus the interesting interactions must be selected online. At CMS this is done in two steps: the Level 1 trigger (L1) which is built of custom

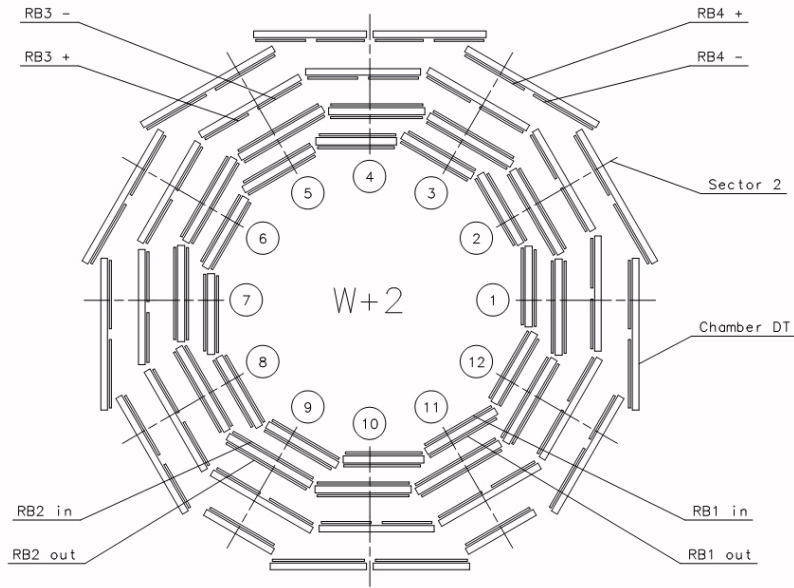


Figure 2.13: A transverse view of the barrel RPCs. [52]

hardware and the High Level Trigger (HLT) which runs on a farm of commercial processors. The L1 trigger performs a fast, coarse-grained analysis of the detector information and reduces the 40 MHz bunch crossing rate to around 30 kHz. The HLT then performs a slower, but more precise analysis and further reduces the rate to about 300 Hz.

Level 1 Trigger

The L1 trigger hardware is located partly on the detector and partly in the underground control room 90 m away. It stores the data from multiple bunch crossings in pipelines and takes at most $3.2 \mu\text{s}$ to decide whether the data from a particular bunch crossing should be sent to the HLT. Because of this need for low latency, only information from the muon systems and calorimeters is used. The hardware consists of field-programmable gate arrays (FPGAs) and application-specific integrated circuits (ASICs) with programmable look up tables. To maximize flexibility, FPGAs are used wherever they can satisfy the requirements for speed and radiation resistance. ASICs

are used in places FPGAs are not suited for.

The calorimeter trigger is based on trigger towers each of which takes input from a grid of 5×5 ECAL crystals and 1 HCAL channel. The transverse energy from these towers is summed, associated with a bunch crossing and passed to the Regional Calorimeter Trigger (RCT). The RCT analyzes regions of 4×4 towers except in HF where each tower is a separate region. It calculates the hadronic and electromagnetic E_T for each region and uses the geometry of the energy distribution in the towers to find electron, photon and tau candidates and compute their isolation. The data from the RCT is passed to the Global Calorimeter Trigger (GCT) which reconstructs jets, calculates the \cancel{E}_T and H_T and then sends them to the Global Trigger (GT).

The DT, CSC and RPC are all part of the muon trigger. The DT creates track segments in the ϕ coordinate and hit patterns in the η coordinate while the CSC makes 3-dimensional track segments. These tracks and hit patterns are used to reconstruct the transverse momentum, location and quality of muon candidates and up to 4 muons from each subsystem are sent to the Global Muon Trigger (GMT). The RPC is treated separately because it has a timing resolution of about 1 ns which allows it to clearly distinguish between bunch crossings. All three muon detectors identify the bunch crossing, but the RPC is best at it. It computes the p_T of muon candidates by measuring the azimuthal coordinate of the track at several points and sends up to 4 muons from the barrel region and up to 4 more from the muon region to the GMT. The GMT combines the information from all three muon systems, eliminates duplicates and passes all information from the muon triggers to the GT.

The Global Trigger makes the final decision on whether to accept or reject the event at L1. It makes use of all objects from the GCT and GMT: electrons, muons, taus, photons, jets, H_T and \cancel{E}_T . In addition, it uses signals sent directly from various subdetectors to accept technical triggers used for calibration.

High Level Trigger

Unlike the L1 trigger, the HLT is implemented entirely in software running on commercial CPUs. In the 2010 data taking period, the HLT farm consisted of 720 machines each using a pair of quad-core processors. The HLT takes information from the L1 trigger and performs a faster and less precise version of offline reconstruction. Because the HLT has significantly more time than the L1 trigger to make a decision, it uses information from the entire detector, including the inner tracking system. However, it only analyzes regions of the detector that have interesting particles for a given bunch crossing. On average, the HLT takes about 40 ms to decide whether to accept a particular bunch crossing, but it can sometimes take significantly longer. Bunch crossings that consume more than a preset amount of time are automatically accepted.

The HLT decision is based on many independent algorithms called paths. Each trigger path is a sequence of software modules which do reconstruction or filtering. If any of the filters fails for a given bunch crossing, the rest of the sequence is ignored. There are currently on the order of 100 different paths with different thresholds for various physics objects. These paths evolve with luminosity delivered by the LHC.

Chapter 3

Data and Simulation Samples

3.1 Data

Each event in CMS data is placed into at least one primary dataset based on the trigger path(s) that accepted it. The primary datasets are then processed further to create secondary datasets (also called “skims”). Because the most prominent signature of dilepton $t\bar{t}$ events is the pair of high p_T leptons, the secondary datasets used in this analysis are dilepton skims of the electron and muon primary datasets. The only requirement for these skims is a pair of leptons with $p_T > 10$ GeV/ c for each of them. The data samples used in this analysis are listed in Table 3.1. They were recorded during 2010 and correspond to a total integrated luminosity of 36 pb^{-1} . One of the muon skims was missing approximately 2 pb^{-1} of integrated luminosity so the primary muon dataset was used to recover the lost luminosity.

In order to locate all $t\bar{t}$ events, we process both muon and electron datasets. To avoid overlap in the $e^\pm\mu^\mp$ channel, we take events from the muon dataset only if they fire a muon trigger and events from the electron dataset only if they fire an electron trigger and do not fire any muon triggers. This algorithm ensures that there is no double-counting and does not miss the rare $e^\pm\mu^\mp$ events which do not fire a muon trigger.

Dataset	Luminosity (pb ⁻¹)
/EG/Run2010A-DiLeptonEle-Nov4Skim_v1/RECO	3
/Mu/Run2010A-DiLeptonMu-Nov4Skim_v1/RECO	3
/Electron/Run2010B-DiLeptonEle-Nov4Skim_v1/RECO	33
/Mu/Run2010B-DiLeptonMu-Nov4Skim_v1/RECO	31
/Mu/Run2010B-Nov4ReReco_v1/RECO	2

Table 3.1: All data samples used in the analysis. The difference between Run2010A and Run2010B is in the primary datasets: the electron-photon (EG) dataset from Run2010A was split into separate Electron and Photon datasets in Run2010B.

CMS data is divided into “runs” which are further subdivided into luminosity sections. A run is simply a continuous period of data-taking. A luminosity section is a fixed time interval of approximately 23 s and corresponds to the smallest time period for which the status of the detector is recorded. Not all data is suitable for analysis because it may have been taken with parts of the detector off or not working properly. Thus, all of the recorded datasets are filtered by removing bad runs and luminosity sections to select only good quality data.

3.2 Simulation

Simulation samples are used to verify that we understand the data and to measure the top quark mass by comparing data to simulated templates corresponding to different top quark masses. The samples used in the analysis are $t\bar{t}$ and its most significant backgrounds: Drell-Yan and single top produced in the tW channel. Most of the samples used were generated with the MADGRAPH event generator [11]. MADGRAPH draws all Feynman diagrams for a given hard process, computes the matrix element of the process and uses this information to produce parton-level events. To generate Drell-Yan events with higher jet multiplicities, we used the ALPGEN event generator which calculates the matrix element numerically (without making explicit use of Feynman diagrams) and can handle a large number of partons in the final state [54]. A third generator, POWHEG, was used to assess differences in event generation and

calculate the systematic uncertainties [55].

The parton-level events are processed through the PYTHIA Monte-Carlo generator which performs the hadronization and showering of final state partons [12]. Because PYTHIA's showering algorithm works in the limit of soft, collinear partons whereas the event generators are only reliable far from the soft and collinear limits, the showering sometimes results in extra jets. To avoid these, we use the MLM parton-jet matching algorithm which rejects events with showers that do not match partons from the matrix element calculation [56]. Tau particles decaying to hadrons result in jets that differ from other hadronic jets so hadronically decaying taus are handled separately by TAUOLA [57]. The HERWIG Monte-Carlo is used to compute the systematic uncertainty due to hadronization and showering [58].

The final step of producing the signal and background samples is to simulate the CMS detector. This is accomplished using GEANT4 which simulates the passage of particles through matter [59]. After this point, the events from simulation and from data are treated in the same way: they are reconstructed with the CMS Software Framework and the Physics Analysis Toolkit [60]. The signal and background samples are shown in Table 3.2.

Sample	σ (pb)	\mathcal{L} (pb ⁻¹)
Main Analysis Samples		
$t\bar{t}$ +Jets, ^a MADGRAPH, PYTHIA TuneZ2 ^b	157.5	7395
$t\bar{t}$ +Jets, MADGRAPH, PYTHIA TuneD6T	157.5	8293
$t\bar{t}$ +Jets, MADGRAPH, PYTHIA TuneZ2, massM ^c	10.2	9200
Single top tW channel, MADGRAPH, PYTHIA TuneZ2	10.6	46694
Drell-Yan, MADGRAPH, PYTHIA TuneZ2 ^d	3048	852
Samples for Data-Driven Background Estimate		
Z+1Jet $p_T Z$ 0-100 GeV/ c , ALPGEN, PYTHIA TuneZ2	381	834
Z+1Jet $p_T Z$ 100-300 GeV/ c , ALPGEN, PYTHIA TuneZ2	8.7	30430
Z+2Jets $p_T Z$ 0-100 GeV/ c , ALPGEN, PYTHIA TuneZ2	104	1144
Z+2Jets $p_T Z$ 100-300 GeV/ c , ALPGEN, PYTHIA TuneZ2	8.5	15425
Z+3Jets $p_T Z$ 0-100 GeV/ c , ALPGEN, PYTHIA TuneZ2	22.9	2404
Z+3Jets $p_T Z$ 100-300 GeV/ c , ALPGEN, PYTHIA TuneZ2	4.0	14357
Z+4Jets $p_T Z$ 0-100 GeV/ c , ALPGEN, PYTHIA TuneZ2	4.6	9619
Z+4Jets $p_T Z$ 100-300 GeV/ c , ALPGEN, PYTHIA TuneZ2	1.3	34093
Z+5Jets $p_T Z$ 0-100 GeV/ c , ALPGEN, PYTHIA TuneZ2	1.1	9633
Z+5Jets $p_T Z$ 100-300 GeV/ c , ALPGEN, PYTHIA TuneZ2	0.5	21914
Samples for Systematic Uncertainty Evaluation ^e		
$t\bar{t}$ +Jets, MADGRAPH, PYTHIA TuneD6T, more ISR/FSR/	157.5	8851
$t\bar{t}$ +Jets, MADGRAPH, PYTHIA TuneD6T, less ISR/FSR	157.5	7757
$t\bar{t}$ +Jets, MADGRAPH, PYTHIA TuneD6T, scale down	157.5	6978
$t\bar{t}$ +Jets, MADGRAPH, PYTHIA TuneD6T, scale up	157.5	7322
$t\bar{t}$ +Jets, MADGRAPH, PYTHIA TuneD6T, matching down	157.5	5956
$t\bar{t}$ +Jets, MADGRAPH, PYTHIA TuneD6T, matching up	157.5	6581
$t\bar{t}$ +Jets, MADGRAPH, PYTHIA TuneD6T, extra pile-up	157.5	8135
Dilepton $t\bar{t}$ +Jets, POWHEG, HERWIG	16.5	60395
Dilepton $t\bar{t}$ +Jets, POWHEG, PYTHIA TuneZ2	16.5	60477

^a $t\bar{t}$ +Jets means $t\bar{t}$ with up to 3 jets not originating from the $t\bar{t}$ decay.

^bPYTHIA tunes Z2 and D6T are described in [61].

^cThis is a set of 17 dilepton $t\bar{t}$ samples differing only in the mass of the top (M) which ranges from 151 GeV/ c^2 to 199 GeV/ c^2 in intervals of 3. The values of the cross section and equivalent luminosity are averages over the 17 samples.

^dThe Drell-Yan has a generator-level cut on the invariant mass of the lepton pair at 50 GeV/ c^2 .

^eFor an explanation of the systematic uncertainties, see Section 8.5.

Table 3.2: List of simulated samples used in the analysis with the cross section and equivalent luminosity for each sample.

Chapter 4

Event Selection and Object Reconstruction

Dilepton $t\bar{t}$ events result in four types of objects that can be observed by our detector: electrons, muons, jets and \cancel{E}_T . To select and reconstruct such events, we require two leptons, two jets and a significant amount of \cancel{E}_T . The leptons and jets must be central and energetic and the lepton invariant mass must be inconsistent with that of the Z boson. Selected events must also pass requirements independent of these objects to verify that they come from clean collisions rather than noise or beam effects.

4.1 Event Cleaning

Prior to any requirements specific to $t\bar{t}$ events, we apply selections intended to eliminate events that result from the beam scraping against the beam pipe. Such events produce many tracks originating far from the nominal collision point. Therefore, we require at least 25% of all tracks in events with 10 or more tracks to be “high purity” tracks. “High purity” tracks are selected based on the χ^2 of the track, the track’s impact parameters and the number of tracker layers with hits. The exact selection criteria are described in [62]. This requirement ensures the presence of high qual-

ity tracks near the interaction point. We also require all valid primary vertices of the event to be less than 24 cm away from the nominal interaction point longitudinally and less than 2 cm away radially. Furthermore, each valid primary vertex must be associated with at least 4 tracks and the z position of the vertex used for the reconstruction of the $t\bar{t}$ system must be within 1 cm of any lepton used in the analysis.

Events are also rejected if they are found to have anomalous HCAL noise coming from HPDs or read-out boxes (RBXs) each of which contains four HPDs. The noise in the HPDs can originate from either the thermal emission of electrons which ionize a molecule in the HPD causing a small cascade or from an HPD discharge due to misalignment with the magnetic field. RBX noise is characterized by a high multiplicity of hits in all four HPDs.

The best means of rejecting the noise using only HCAL is the pulse shape variable. HCAL reads out ten 25 ns time slices for each event. The pulse shape variable is the ratio of the energy in the two peak time slices to the energy in all ten. To reject the noise, we use a combination of the pulse shape variable, timing with respect to the rest of the event, the hit multiplicity and lack of coincidence with ECAL. The details of this combination are described in [63].

4.2 Trigger

The distinguishing characteristic of dilepton $t\bar{t}$ events is the presence of two electrons, two muons or an electron and a muon. Thus, we can achieve a high trigger efficiency by using a combination of muon and electron triggers. To maintain a constant rate of events written to storage media, the triggers had to evolve as the instantaneous luminosity delivered by the LHC increased. The list of triggers used for specific ranges of runs is shown in Table 4.1. The combined efficiency of these triggers for events that pass other analysis selections is more than 99%.

Trigger	Run Range	\mathcal{L} (pb ⁻¹)
Muon Triggers		
Mu9 ^a	Run \leq 145000	3.2
Mu11	145000 < Run \leq 147120	5.0
Mu15	147120 < Run	27.8
Electron Triggers		
Ele10_LW ^b	Run \leq 138000	0.01
Ele15_LW	138000 < Run \leq 141900	0.3
Ele15_SW ^c	141900 < Run \leq 144000	2.2
Ele15_SW_CaloEleId ^d <i>or</i> Ele20_SW <i>or</i> DoubleEle10_SW ^e	144400 < Run \leq 144114	0.7
Ele17_SW_CaloEleId <i>or</i> DoubleEle10_SW	146000 < Run \leq 147120	5.0
Ele17_SW_TightCaloEleId_SC8HE ^f <i>or</i> Ele17_TightEleId_SW ^g <i>or</i> DoubleEle15_SW	147120 < Run \leq 148100	9.4
DoubleEle17_SW <i>or</i> Ele17_SW_TightCaloEleId_Ele8HE ^h <i>or</i> Ele22_SW_TighterEleId <i>or</i> Ele17_SW_TighterEleIdIsol ⁱ <i>or</i>	148100 < Run	18.4

^aThe number following the name of the particle (“Mu” or “Ele”) is p_T threshold of the trigger in GeV/ c . “Mu” stands for a muon and “Ele” means an electron.

^bLW means a large pixel matching window.

^cSW is a smaller pixel matching window.

^dCaloEleId uses the cluster shape in ECAL to identify the electron.

^eDoubleEle means that there must be two electrons with the given p_T .

^fSC8HE refers to the supercluster energy and the ratio of the electron’s energy in HCAL to that in ECAL.

^gEleId means that the electron must be identified in both ECAL and the tracker.

^hThis trigger requires one electron with $p_T > 17$ GeV/ c and another one with $p_T > 8$ GeV/ c .

ⁱIsol refers to an isolation cut applied around the electron.

Table 4.1: Complete list of triggers used for the analysis.

CMS has a dedicated muon trigger subsystem which is located outside of the calorimeters and is rarely affected by particles other than muons. This makes muons

easy to identify so the only changes needed to keep the muon trigger rate from growing were small increases in the p_T threshold. The highest single muon trigger p_T cut was at 15 GeV/ c which is well below the 20 GeV/ c cut used in our analysis and thus has no noticeable impact on our efficiency.

Electrons are much more difficult to distinguish from the multijet background and controlling the rate by merely increasing the p_T threshold would have caused the loss of signal events. To avoid this, several electron quality criteria (described in section 4.4) were introduced starting at the HLT. These include decreasing the size of the “pixel matching” window in which pixel tracks and ECAL superclusters are considered matched, requiring an ECAL supercluster with a minimum E_T , requiring a maximum value of the ratio of the energy in HCAL to that in ECAL and imposing an isolation requirement. To maximize signal acceptance, various combinations of these quality cuts and different p_T thresholds were used as described in Table 4.1. Furthermore, double electron triggers were used to improve coverage of the e^+e^- channel.

4.3 Muons

Muons are reconstructed in CMS using a combination of the inner tracking system and the dedicated muon systems (DT, CSC and RPC). The muons interact with the detector at several points along their trajectory. These points are called “hits” and can be reconstructed into tracks. The tracks in the muon systems and the tracker are reconstructed using similar algorithms. The trajectory of the muons is curved as they travel through the region of the magnetic field, which allows their p_T to be measured. An idealized version of a charged particle in the magnetic field of a solenoid is shown in Figure 4.1. The CMS detector differs from this ideal version in two ways: the magnetic field is not homogeneous and there is material in the detector which

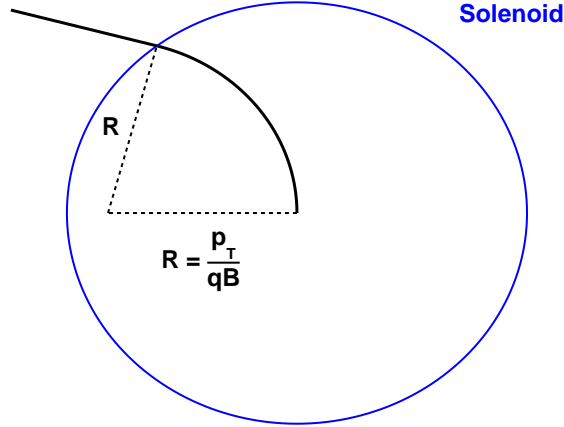


Figure 4.1: The trajectory of a particle with charge q and transverse momentum p_T inside an ideal solenoid with a magnetic field B .

interacts with the muon. The inhomogeneity of the magnetic field is dealt with by incorporating the changes of the \vec{B} field into the parameterization of the trajectory and solving for the latter using the recursive method of Runge-Kutta. Details of this algorithm can be found in [64].

Material affects the trajectory of the muons in two ways. First, the average energy of the muon decreases according to the Bethe-Bloch formula [1]:

$$-\left\langle \frac{dE}{dx} \right\rangle = K z^2 \frac{Z}{A} \frac{1}{\beta^2} \left[\frac{1}{2} \ln \left(\frac{2m_e c^2 \beta^2 \gamma^2 T_{max}}{I^2} \right) - \beta^2 - \frac{\delta(\beta)}{2} \right], \quad (4.1)$$

where E is the energy of the particle, x is the distance traveled through the material, K is a constant independent of the material and particle, z is the charge of the particle, Z is the atomic number of the absorber, A is the atomic mass of the absorber, m_e is the mass of the electron, T_{max} is the maximum kinetic energy which can be imparted to a free electron in a single collision, I is the mean excitation energy and $\delta(\beta)$ is the density effect correction to the ionization energy. This loss of energy is well understood and the tracking algorithm includes a correction for it. The second effect

of the material is due to multiple scattering which deflects the trajectory of the muon in a stochastic manner. This increases the uncertainty in the trajectory and is one of the reasons to have the high resolution pixel closest to the interaction point.

In both the muon systems and the tracker, trajectories are reconstructed in four steps. First, the hits in the detector are used to construct seeds which consist of two or three hits compatible with the nominal interaction point. Second, a combinatorial Kalman filter [65] is used to build the trajectory by employing the full knowledge of all analyzed detector layers to find compatible hits in each next detector layer. The Kalman filter accounts for the energy loss of the muons by using the Bethe-Bloch formula and giving the loss a Gaussian spread. Third, the ambiguities arising from hits shared by multiple track candidates are resolved by discarding candidates with the fewest hits or the highest χ^2 if the numbers of hits are equal. Finally, the trajectory is smoothed by running another Kalman filter from the outermost hit towards the interaction point. This applies the full knowledge of the detector to the innermost parts of the trajectory. A more detailed description of track reconstruction can be found in [66].

Once the tracks in the tracker and muon systems have been reconstructed, two different approaches are used to combine them into muons: Global Muon reconstruction and Tracker Muon reconstruction. Global Muon reconstruction starts with a track reconstructed in the muon systems (called a “standalone” muon), matches it to a track in the tracker and performs a fit combining the two sets of hits. The matching is done by considering tracks from the tracker in a rectangular $\eta - \phi$ region around the standalone muon and selecting the track most compatible with the standalone muon in position and momentum at a boundary surface. The final fit of the Global Muon is again based on the Kalman filter technique. Details of the matching and fit can be found in [64].

Tracker Muon reconstruction starts with a track in the tracker and extrapolates

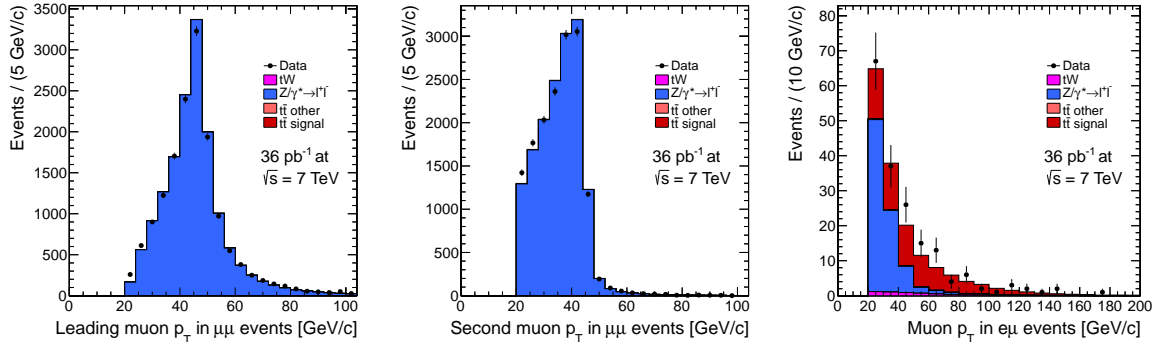


Figure 4.2: The p_T distributions of leading muons in $\mu^+\mu^-$ events (left), muons with the lower p_T in $\mu^+\mu^-$ events (center) and muons in $e^\pm\mu^\mp$ events (right).

it to the muon systems. The propagation of the track is done using the same method of Runge-Kutta as for standalone muons. Tracker Muons are derived entirely from the track in the tracker, but they must be matched to at least a short segment of hits in the muon chambers. Thus, they require fewer hits in the muon systems than are necessary for a Global Muon and do not make use of a final fit between the subdetectors [67].

Muons used in determining the mass of the top quark are required to be reconstructed using both the Tracker Muon and Global Muon algorithms, although only Global Muons are used in the analysis. Muons from cosmic rays and hadrons are avoided by requiring the minimum transverse distance between the muon and the nominal interaction point to be less than 0.2 mm. We want only muons clearly visible in both subdetectors, so we use only those that have more than 10 tracker hits and at least 1 muon chamber hit in the final fit. Furthermore, the χ^2 of the final Global Muon fit divided by the number of degrees of freedom must be less than 10. The fit always includes the interaction point and constrains the result to select mostly muons from prompt decays from W and Z bosons.

The particles coming from top quark decays are expected to be central and energetic. We require the muons to have $p_T > 20$ GeV/ c and $|\eta| < 2.4$. To preclude muons

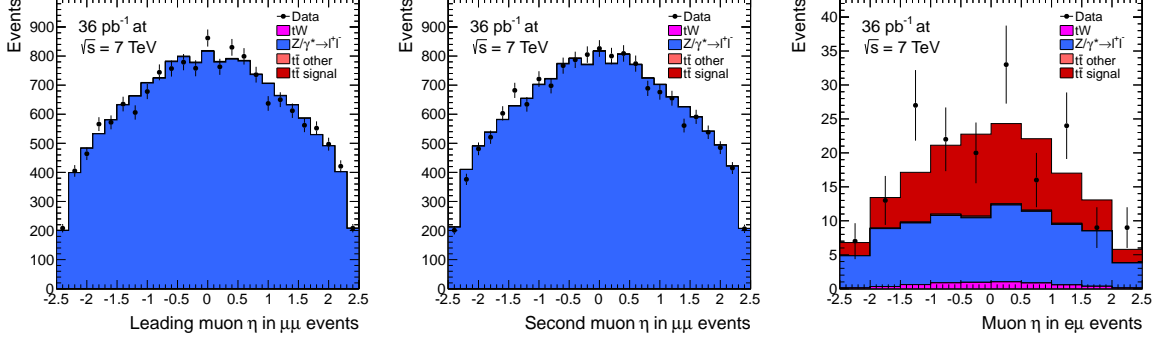


Figure 4.3: The η distributions of leading muons in $\mu^+\mu^-$ events (left), muons with the lower p_T in $\mu^+\mu^-$ events (center) and muons in $e^\pm\mu^\mp$ events (right).

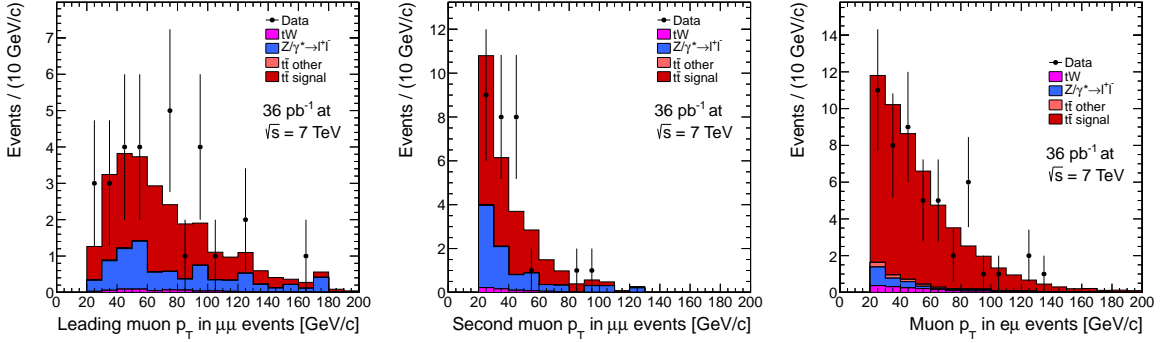


Figure 4.4: The p_T distributions of leading muons in $\mu^+\mu^-$ events (left), muons with the lower p_T in $\mu^+\mu^-$ events (center) and muons in $e^\pm\mu^\mp$ events (right) after the full selection.

from heavy flavor hadron decays and hadrons that punch through the calorimeters, we impose isolation criteria based on the energy of particles around the muon. The region of interest for the isolation is defined to be a cone of $\Delta R < 0.3$ around the muon where $\Delta R = \sqrt{(\Delta\eta)^2 + (\Delta\phi)^2}$. We exclude the muon itself from this cone and then require the sum of the E_T in the cone from all particles in the tracker, ECAL and HCAL divided by the E_T of the muon to be less than 0.15.

The p_T and η distributions of muons in events with at least two selected leptons are shown in Figures 4.2 and 4.3. For muons, the agreement between data and simulation is nearly perfect. The slight excess of data in low p_T bins is due to the simulated Drell-Yan sample having a cut on the invariant mass of the muon pair at $50 \text{ GeV}/c^2$.

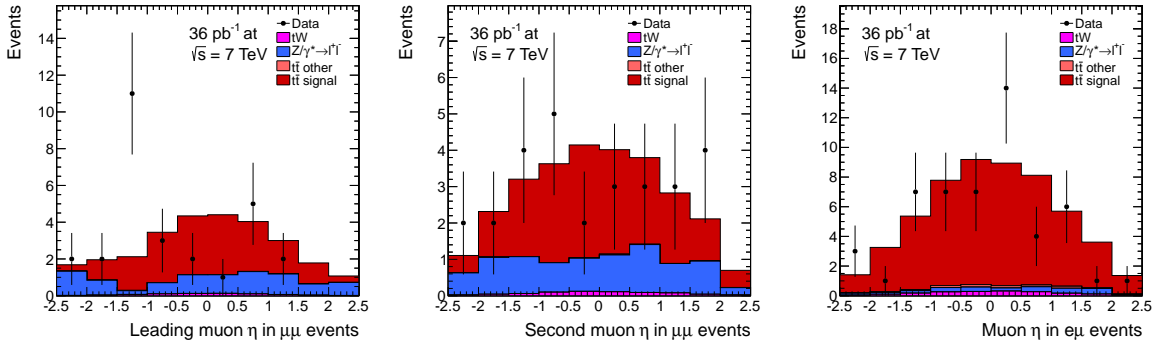


Figure 4.5: The η distributions of leading muons in $\mu^+\mu^-$ events (left), muons with the lower p_T in $\mu^+\mu^-$ events (center) and muons in $e^\pm\mu^\mp$ events (right) after the full selection.

The same kinematic properties of muons after the full selection (including cuts on leptons, jets, \cancel{E}_T and the Z -veto) are shown in Figures 4.4 and 4.5. There are far fewer events in these distributions, but the data and simulation remain consistent within the statistical uncertainties.

4.4 Electrons

Electron reconstruction in CMS is performed using the tracker and the electromagnetic calorimeter. There are two different algorithms used to reconstruct electrons: the tracker-driven algorithm and the ECAL-driven algorithm. Both contribute to finding the seeds for electron tracks, but electrons used to determine the mass of the top quark are required to be identifiable with the ECAL-driven algorithm.

A description of the tracker-driven algorithm can be found in [68]. The ECAL-driven algorithm starts by finding “superclusters” with energy deposited by the electrons. In the case of electrons that reach ECAL without having lost a significant fraction of their energy, this is simple: about 97% of the incident energy of electrons with $p_T = 120$ GeV/ c is deposited within a 5×5 crystal window [69]. However, the electrons from the interaction point need to pass through about 2 radiation

lengths of material in the tracker before they reach ECAL and they lose energy to bremsstrahlung. Due to the magnetic field, the path of the electrons is curved and hence they radiate photons along the way. The photons reach ECAL spread out in ϕ , but not in η . Therefore, to recover the electron and the bremsstrahlung photons, superclusters are constructed by summing energy depositions that are separated only in ϕ .

After the supercluster has been reconstructed, it is used to construct the seed for determining the track associated with the electron. The position of the supercluster is propagated backwards through the magnetic field towards the pixel detector (this is done for both possible charges to account for electrons and positrons). The inner layers of the pixel detector are closest to the beam pipe so the electrons are unlikely to have interacted with material before reaching them. Therefore, the seeds are taken to be hits in the two inner layers of the pixel detector within a loose $\Delta\eta - \Delta\phi$ window of the supercluster.

Due to the bremsstrahlung, the Bethe-Bloch formula cannot be used to accurately predict the energy loss of electrons in matter and the Bethe-Heitler model is used instead. In this model, the probability density function of the energy loss of an electron is given by:

$$f(z) = \frac{[-\ln z]^{c-1}}{\Gamma(c)}, \quad (4.2)$$

where $c \cdot \ln(2)$ is the thickness of the material the electron has traveled through in radiation lengths and z is the fraction of energy remaining after traversing this thickness. The Bethe-Heitler distribution cannot be accurately described by a single Gaussian so the Kalman filter is not an optimal way to reconstruct the track of the electron. To solve this problem, we use the Gaussian-sum filter which is a generalization of the Kalman filter. It accounts for the energy loss of the electrons by using a weighted sum of Gaussians rather than a single Gaussian [70].

The electrons are reconstructed as a track and a shower of particles in the calorime-

ters. We apply several selections to distinguish them from hadronic activity. As described above, the width of the supercluster in η (called $\sigma_{i\eta i\eta}$) should be small and the supercluster and track should be close to each other in both η and ϕ . Furthermore, the electron should leave a substantial amount of energy in the supercluster so we require supercluster $E_T > 15$ GeV. In addition, the energy deposited by the electron in HCAL (called H) should be much less than energy in ECAL (called E). We impose this condition by requiring the ratio of the two (referred to as H/E) to be small. Finally, an electron can be mimicked by a combination of a muon (which provides the track) and hadrons in ECAL. To avoid these, we require $\Delta R > 0.1$ between the electron and any muon.

The ECAL barrel and endcaps have different geometries and have slightly different selection criteria imposed on them. The criteria are shown in Table 4.2. A more detailed description and the derivation of the values of parameters used for electron identification can be found in [71].

Variable	Barrel Cut	Endcap Cut
$\Delta\eta$	0.007	0.009
$\Delta\phi$	0.8	0.7
$\sigma_{i\eta i\eta}$	0.001	0.03
H/E	0.12	0.05

Table 4.2: Criteria used for electron identification.

In $t\bar{t}$ samples, we are only interested in electrons from W bosons and impose several additional constraints to select them. To avoid electrons from hadrons, we require the minimum transverse distance between the electron and the nominal interaction point to be less than 0.4 mm. Photon conversion into e^+e^- pairs is another undesired source of electrons. We eliminate it by rejecting electrons that do not have a hit in more than 1 layer of the tracker and have an oppositely charged partner.

The kinematic properties of electrons and muons from top quark decays are not expected to differ. We impose almost the same selection for muons as for electrons:

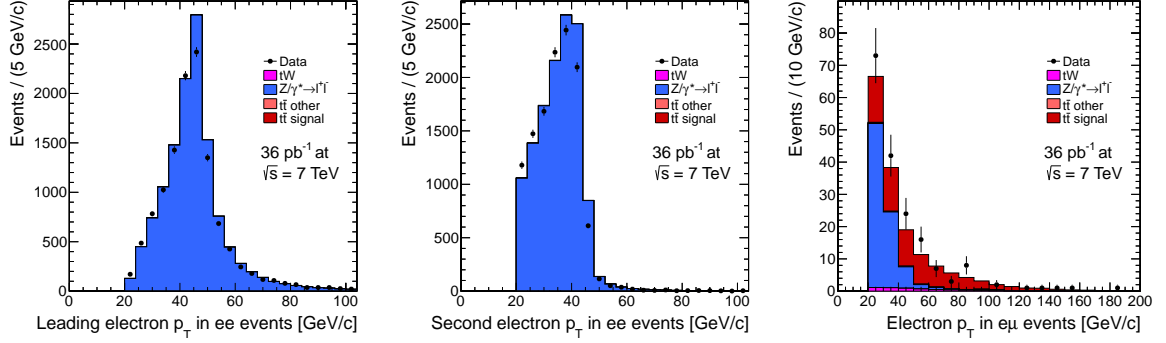


Figure 4.6: The p_T distributions of leading electrons in e^+e^- events (left), electrons with the lower p_T in e^+e^- events (center) and electrons in $e^\pm\mu^\mp$ events (right).

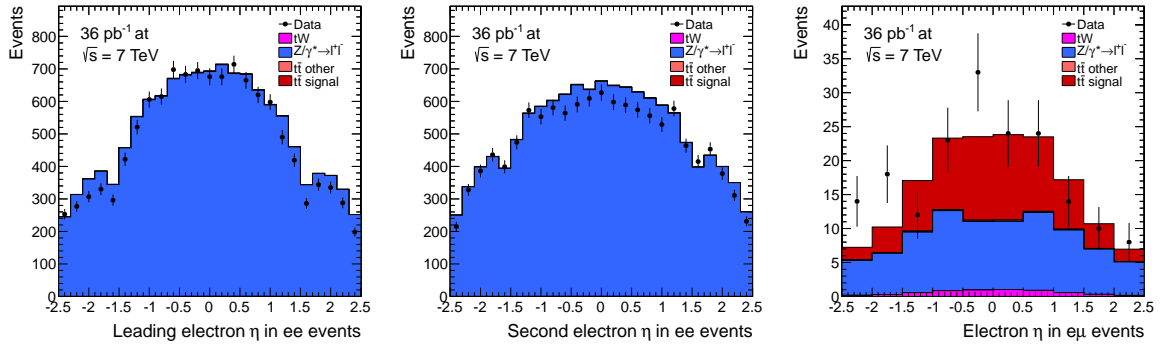


Figure 4.7: The η distributions of leading electrons in e^+e^- events (left), electrons with the lower p_T in e^+e^- events (center) and electrons in $e^\pm\mu^\mp$ events (right).

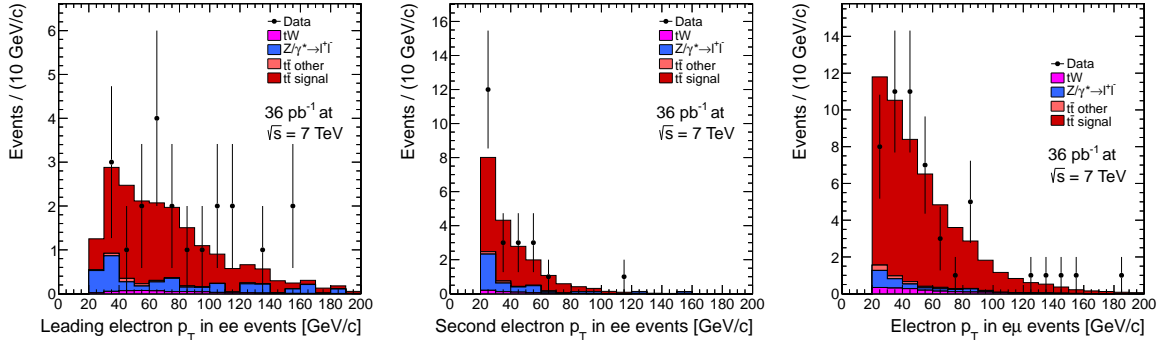


Figure 4.8: The p_T distributions of leading electrons in e^+e^- events (left), electrons with the lower p_T in e^+e^- events (center) and electrons in $e^\pm\mu^\mp$ events (right) after the full selection.

$p_T > 20 \text{ GeV}/c$ and $|\eta| < 2.5$. The slight difference in the $|\eta|$ cut is due to the greater acceptance of ECAL relative to the muon system. Similarly, electrons are required to be isolated in the same way as muons. For each electron, we compute the sum of the E_T from all particles within $\Delta R < 0.3$ of the electron (excluding the electron itself). This sum divided by the electron's E_T must be less than 0.15.

The kinematic properties of selected electrons in dilepton events are shown in Figures 4.6 and 4.7. Due to a small miscalibration of the ECAL endcaps, the agreement of p_T distributions in data and simulation is not as good as it is for muons. This effect is taken into account when computing the systematic uncertainty for the top quark mass measurement. Just as with muons, the excess of data in the low p_T bins is due to the $50 \text{ GeV}/c^2$ cut on the dielectron invariant mass in the Drell-Yan sample. The inefficiency near $|\eta| = 1.5$ is due to the gap between the ECAL barrel and endcaps. The η and p_T distributions of electrons after the full selection are shown in Figures 4.8 and 4.9. The consistency of data and simulation is within the statistical uncertainty.

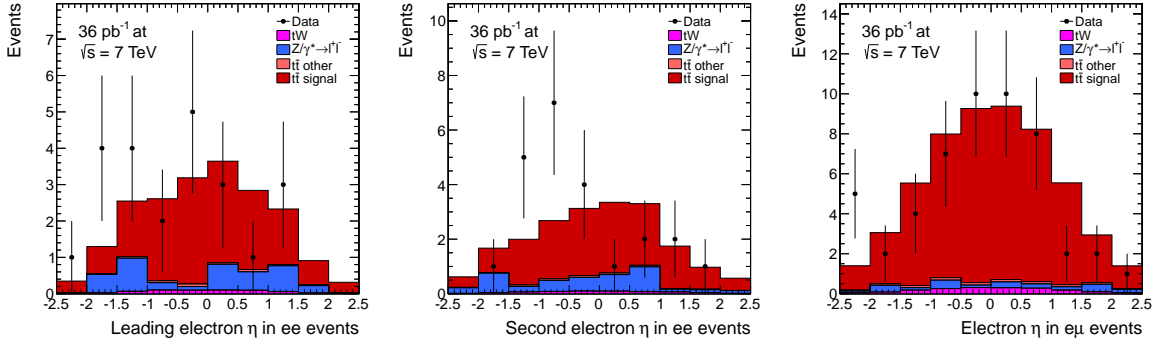


Figure 4.9: The η distributions of leading electrons in e^+e^- events (left), electrons with the lower p_T in e^+e^- events (center) and electrons in $e^\pm\mu^\mp$ events (right) after the full selection.

4.5 Dilepton Selection

To reconstruct the top quark mass, we require two opposite signed leptons: e^+e^- , $\mu^+\mu^-$ or $e^\pm\mu^\mp$. If there are more than two good leptons in the event, we use the pair with the greatest total p_T . To reduce the number of background events, two requirements are imposed on the invariant mass of the dilepton pair ($M_{\ell+\ell^-}$). To reject the Drell-Yan background in the e^+e^- and $\mu^+\mu^-$ channels, $M_{\ell+\ell^-}$ is required to be more than $15 \text{ GeV}/c^2$ away from the mass of the Z boson (that is, $M_{\ell+\ell^-} < 76 \text{ GeV}/c^2$ or $M_{\ell+\ell^-} > 106 \text{ GeV}/c^2$). The width of the Z boson is $2.5 \text{ GeV}/c^2$ [1], but due to the effects of detector resolution, the standard deviation of the invariant mass distribution is approximately $3.5 \text{ GeV}/c^2$. Thus, this requirement eliminates the Drell-Yan background to slightly over 4 standard deviations. The second selection is necessary to eliminate the background due to heavy flavor resonances. A requirement of $M_{\ell+\ell^-} > 12 \text{ GeV}/c^2$ is imposed in all channels.

The dilepton invariant mass distributions in e^+e^- , $\mu^+\mu^-$ and $e^\pm\mu^\mp$ events are shown in Figure 4.10. As with the p_T distribution, the agreement between data and simulation is best in dimuon events. The invariant mass distributions after the full selection are shown in Figure 4.11.

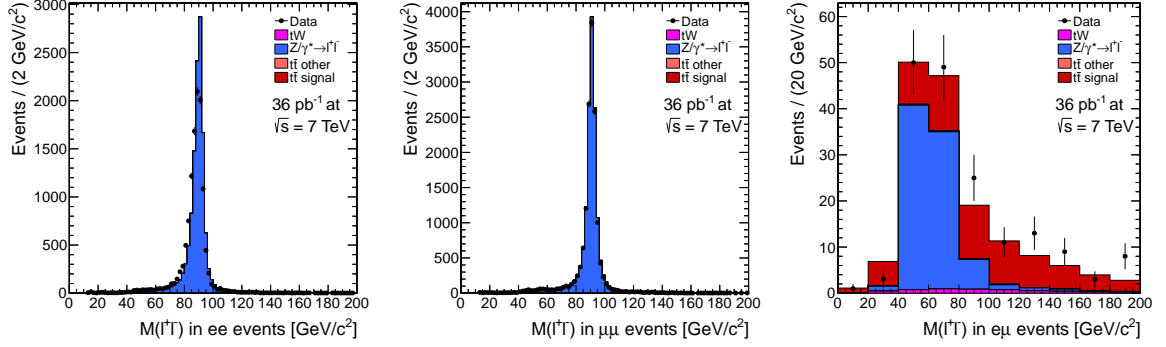


Figure 4.10: The dilepton invariant mass distribution in e^+e^- (left), $\mu^+\mu^-$ (center) and $e^\pm\mu^\mp$ (right) events.

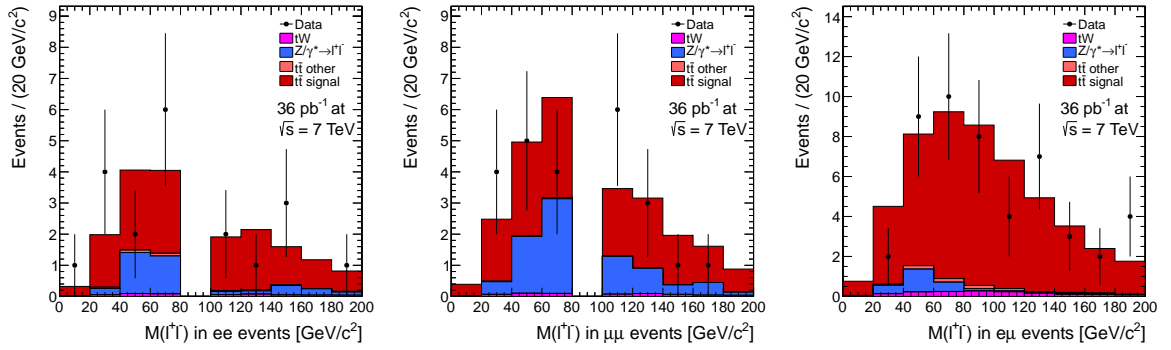


Figure 4.11: The dilepton invariant mass distribution in e^+e^- (left), $\mu^+\mu^-$ (center) and $e^\pm\mu^\mp$ (right) events after the full selection.

4.6 Jets

Unlike muons and electrons, bottom and antibottom ($b\bar{b}$) quarks do not remain free particles long enough to travel through the tracker. As the $b\bar{b}$ quarks fly through the detector, due to color confinement, the separation of the $b\bar{b}$ pair produces other quark-antiquark pairs until all of the quarks have been rearranged into color-neutral hadrons. The hadrons then decay into lighter quarks and possibly leptons, thus forming jets of particles which are observed in the detector.

The goal of jet reconstruction is to determine the momentum of the original quarks. To reconstruct the jets, we first need identify all of their constituents. This is accomplished using the particle flow (PF) algorithm. Once all of the particles are found, we use the anti- k_t algorithm to construct jets out of them. The non-linear calorimeter response necessitates that the measured energy of the jet is corrected based on its kinematic properties to bring it closer to the energy of the original particle.

A detailed description of the PF algorithm can be found in [72]. In brief, the PF algorithm attempts to reconstruct all stable particles in the event by using a combination of all CMS subdetectors. It starts by considering all tracks and finding those that correspond to Global Muons compatible with muons reconstructed within the tracker alone. These “PF muons” are used to estimate the energy deposited by the muon in ECAL and HCAL and then their tracks are removed from the track collection. A similar technique is then applied to electrons: “PF electrons” are reconstructed using the tracker-driven algorithm and their tracks and superclusters are likewise removed from the event.

After the muons and electrons have been removed, the remaining tracks are assumed to be either due to charged hadrons or fake. Both ECAL and HCAL are used to eliminate the fake tracks and assist in measuring the energy of the hadrons. The calorimeters are calibrated using simulated single hadrons and this calibration

is verified in the data using high quality tracks which must have at least 15 hits and $p_T > 1 \text{ GeV}/c$. Tracks that are not compatible with energy deposits in the calorimeters are removed. ECAL and HCAL clusters which are not matched to any track are taken to arise from photons or neutral hadrons.

To reconstruct jets from tracks and calorimetric energy deposits, we use the anti- k_t algorithm [73]. This algorithm has several important attributes. It is “collinear safe” which means splitting a single entity into two collinear ones does not change the results. It is also “infrared safe”: perturbations from entities with very low energy likewise do not change the results. Furthermore, the algorithm results in cone-like jets around entities with the largest transverse momentum without explicitly requiring cones.

The anti- k_t algorithm defines distances between various energetic entities as:

$$d_{ij} = \min\left(\frac{1}{k_{ti}^2}, \frac{1}{k_{tj}^2}\right) \frac{\Delta_{ij}^2}{R^2}, \quad (4.3a)$$

$$d_{iB} = \frac{1}{k_{ti}^2}. \quad (4.3b)$$

Here, d_{ij} is the distance between entity i and entity j , d_{iB} is the distance between entity i and the beam, k_t is the transverse momentum, R is the characteristic radius of the jet and $\Delta_{ij}^2 = (y_i - y_j)^2 + (\phi_i - \phi_j)^2$. For all top quark mass studies at CMS, the radius of the jets (R) is set to 0.5. Using this definition of distance, the algorithm looks for the minimum distance between two entities. If this distance is d_{ij} , then entities i and j are merged into a new entity and the search for the minimum distance starts anew. If the minimum distance is d_{iB} , then i is considered to be a jet and is removed from the list of entities. The process continues until all tracks and calorimetric energy deposits have been incorporated into jets.

The final step of jet reconstruction is to correct the energy scale of the jets to compensate for the calorimeter response. The response is estimated using the mean value

of the p_T^{Gen}/p_T^{Reco} distribution where p_T^{Gen} is the transverse momentum of simulated jets before accounting for the properties of the detector and p_T^{Reco} is the transverse momentum after detector reconstruction. The jets are first corrected so that their response is flat in η . This is accomplished by correcting jets in every η region relative to jets in $|\eta| < 1.3$. The correction is derived from simulation and verified in data using the p_T balance of back-to-back dijet events. The second correction applied to the jets is designed to make the response flat in p_T . This correction is likewise derived from simulation, but the verification in data is done using jet-photon balancing. The third and final jet energy correction is applied to data only and resolves small differences of the response in η . A detailed description of the jet corrections can be found in [74].

For the reconstruction of the top quark mass, we require events with at least two jets that have $p_T > 30$ GeV/ c and $|\eta| < 2.5$. To make sure that the jets do not originate from noise in the calorimeters, each jet is required to have the properties in Table 4.3. Furthermore, as leptons and jets can sometimes overlap, we require $\Delta R > 0.4$ between each jet and each of the two selected leptons.

Variable	Selection
Number of Constituents	> 1
Neutral Hadronic Fraction	< 0.99
Neutral Electromagnetic Fraction	< 0.99
Charged Multiplicity	> 0
Charged Hadronic Fraction	> 0
Charged Electromagnetic Fraction	< 0.99

Table 4.3: Criteria used for jet identification.

The number of selected jets in events with at least two leptons and the number of jets after the full selection are shown in Figure 4.12. There is a slight excess of Drell-Yan events with two or more high p_T jets. For the measurement of the top quark mass, this is accounted for by using a data-driven estimate for the Drell-Yan background. The p_T and η of the two leading jets in events with two jets and two

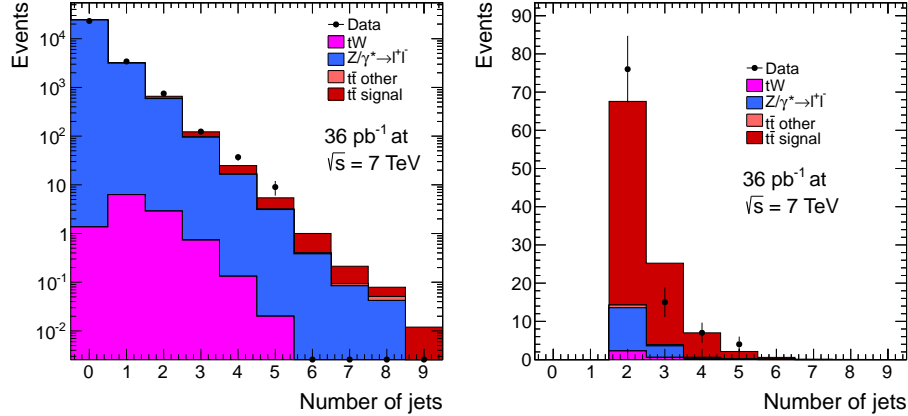


Figure 4.12: The number of jets in events with two leptons (left) and the number of jets after the full selection (right).

leptons are shown in Figures 4.13 and 4.14. The same kinematic distributions after the full selection are in Figures 4.15 and 4.16.

4.7 Missing Transverse Energy

The neutrinos from the W^\pm decays cannot be directly detected by the CMS detector. However, because the sum of p_T of all particles in the event must be zero, the neutrinos are indirectly visible as missing transverse energy. Like the jets, $\vec{\cancel{E}}_T$ is calculated using the particle flow algorithm. Once all of the PF objects have been reconstructed and all relevant corrections have been applied, $\vec{\cancel{E}}_T$ is simply the negative of the vector sum of all transverse momenta.

The missing transverse energy serves two purposes: it is an input to the algorithm reconstructing the $t\bar{t}$ system and it is a means of discriminating against background. In the $e^\pm\mu^\mp$ channel, the background is relatively small so we require only $\cancel{E}_T > 20$ GeV to keep fluctuations in $\vec{\cancel{E}}_T$ from dominating the input to the reconstruction algorithm. The e^+e^- and $\mu^+\mu^-$ channels are affected by the Drell-Yan background so the cut for them is higher: $\cancel{E}_T > 30$ GeV.

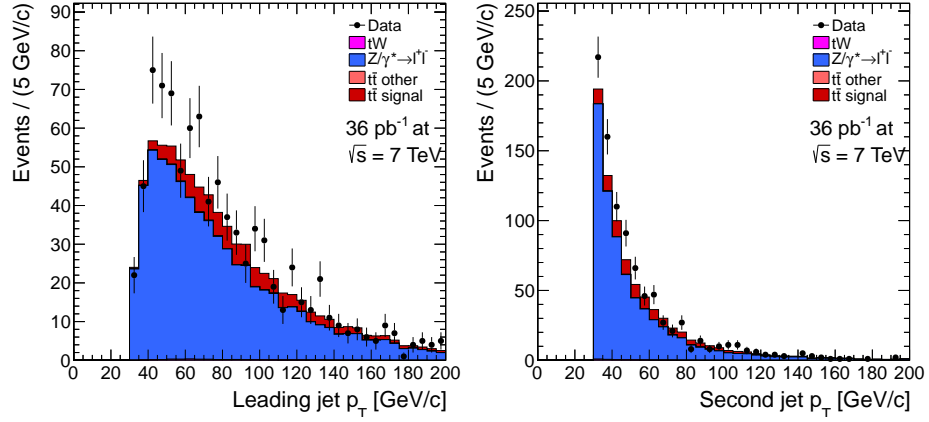


Figure 4.13: The p_T of the leading jet (left) and the jet with the second highest p_T (right) in events with at least two jets and two leptons.

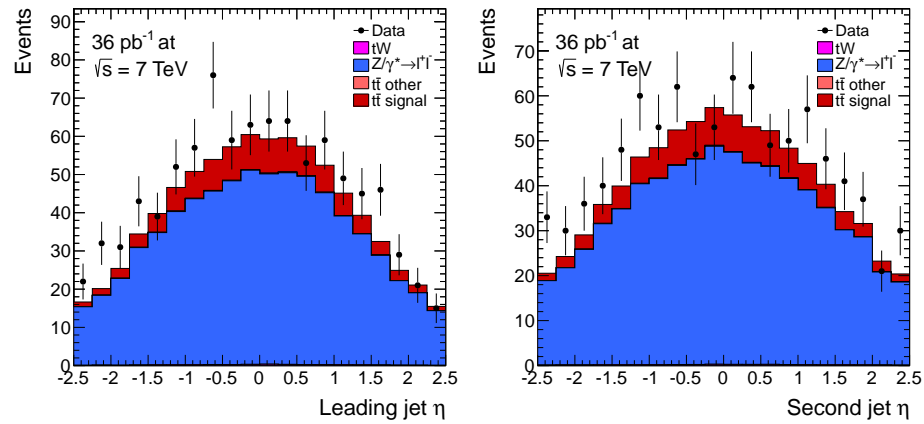


Figure 4.14: The η of the leading jet (left) and the jet with the second highest p_T (right) in events with at least two jets and two leptons.

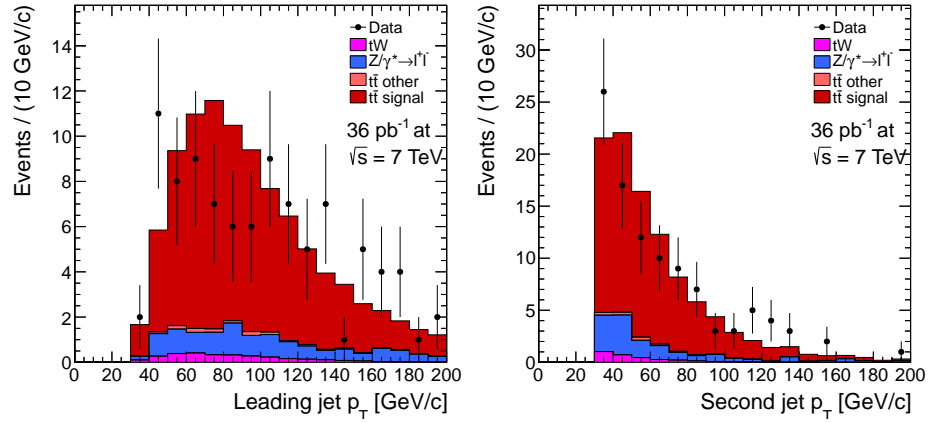


Figure 4.15: The p_T of the leading jet (left) and the jet with the second highest p_T (right) after the full selection.

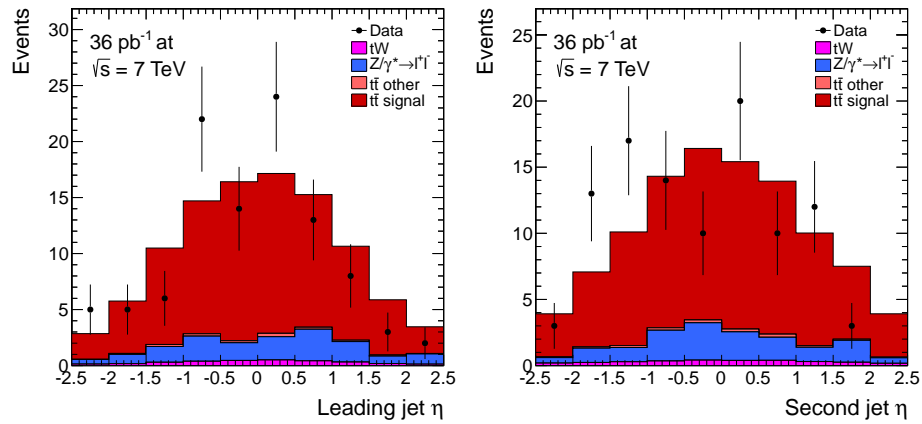


Figure 4.16: The η of the leading jet (left) and the jet with the second highest p_T (right) after the full selection.

Distributions of \cancel{E}_T in events with two leptons and two jets are shown in Figure 4.17. In addition to having more jets, the Drell-Yan events in data also have more \cancel{E}_T which leads to a slightly harder spectrum with this loose selection. The same distributions, but with the full selection can be seen in Figure 4.18.

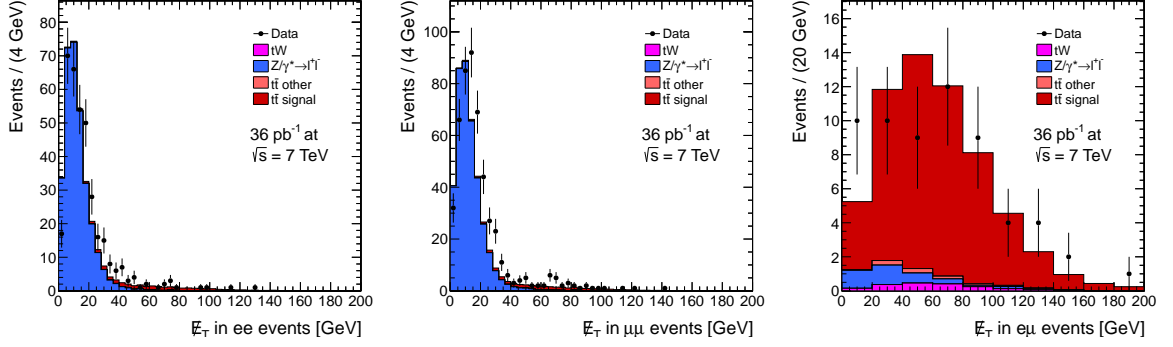


Figure 4.17: The \cancel{E}_T distribution in e^+e^- , $\mu^+\mu^-$ and $e^\pm\mu^\mp$ events.

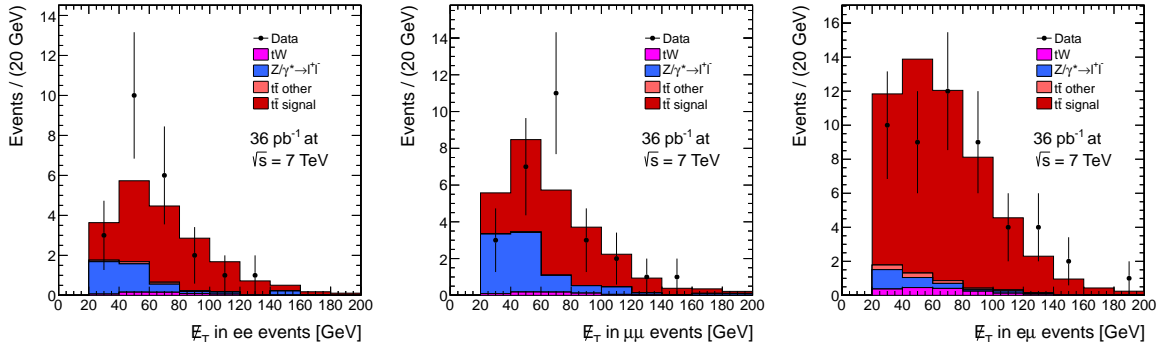


Figure 4.18: The \cancel{E}_T distribution in e^+e^- , $\mu^+\mu^-$ and $e^\pm\mu^\mp$ events after the full selection.

4.8 Event Selection Summary

The number of events remaining after each selection cut is shown in Table 4.8. The event yields in data and simulation are consistent except for the discrepancies described in previous sections. A total of 102 events pass the full selection.

Selection cut	Data	Total expected	$t\bar{t}$ signal	Total background
pre-tagged sample				
≥ 2 id-iso-leptons	27257	28934 ± 49	158.8 ± 0.9	28775 ± 49
Opposite Sign	26779	28545 ± 42	157.3 ± 0.9	28388 ± 42
Z/quarkonia-veto	2878	2873 ± 27	139.3 ± 0.8	2734 ± 27
≥ 2 jets	204	193 ± 2	103.1 ± 0.7	90 ± 2
\cancel{E}_T	102	$108.4 \pm 0.9^{+3}_{-2}$	$92.1 \pm 0.7^{+2}_{-1}$	$16 \pm 1^{+1}_{-1}$

Table 4.4: Total number of dilepton events after each selection cut. The \cancel{E}_T row corresponds to the final selection. The quoted uncertainties are statistical, except for the last row where the systematic uncertainties from jet energy scale variation is also shown. The 4% uncertainty due to the luminosity is not included.

Chapter 5

Jet Selection

5.1 Initial and Final State Radiation

At the LHC, the two b-jets resulting from the decay of the $t\bar{t}$ system may not be the two jets with the highest p_T (called leading jets). This is caused by the presence of initial and final state radiation (ISR and FSR respectively). An illustration of ISR and FSR is shown in Figure 5.1. ISR/FSR jets occur when either the incoming partons or outgoing quarks radiate gluons which are then reconstructed as separate jets. They can be distinguished from the b-jets by using a b -tagging algorithm as described in Section 5.2.

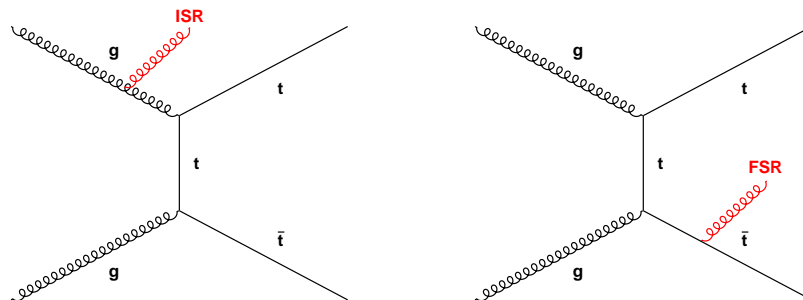


Figure 5.1: Initial state radiation (left) and final state radiation (right) in $t\bar{t}$ events.

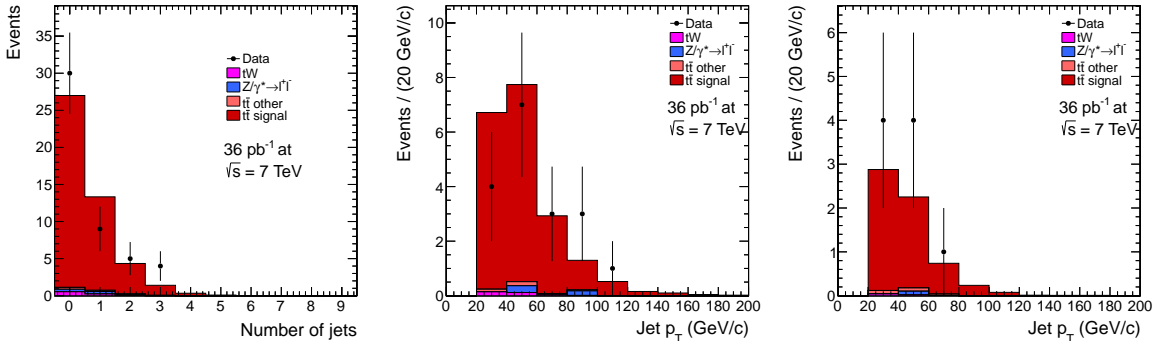


Figure 5.2: The number of jets assumed to be ISR or FSR (left) in events passing the full selection and having two b -tagged jets. The p_T of the leading (center) and second leading (right) ISR/FSR jet.

To study the ISR/FSR, we consider events that pass the full selection and have at least two b -tagged jets. This results in a data sample that is almost entirely dilepton $t\bar{t}$ (in simulation, the purity is 96%) and all jets other than the two b -tagged ones are most likely due to ISR/FSR. Distributions of the number of these jets and p_T of the two leading ones are shown in Figure 5.2. The ISR/FSR jets in data and simulation are consistent within the statistical uncertainty.

5.2 b -tagging

The algorithm we use to tag the b -jets is called track counting. It relies on the displacement of the tracks from the primary vertex to differentiate b -jets from other jets. As mentioned above, the b and \bar{b} quarks undergo hadronization before decaying. In order to decay to lighter hadrons, the B -mesons and b -baryons formed by the b quarks must change flavor. This forces them to decay via the weak interaction and thus they have relatively large lifetimes of approximately 1.6 ps [1]. Combined with relativistic effects, this allows them to travel an average of 0.5 mm from the primary vertex before decaying [75]. The track counting algorithm calculates the distance of closest approach to the primary vertex for each track in a given jet. This distance is

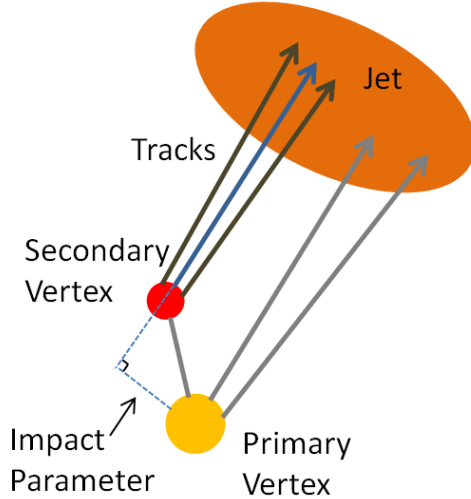


Figure 5.3: The decay of a b -hadron at a secondary vertex and the impact parameter of one of the resulting tracks.

called the impact parameter (IP) and it is shown in Figure 5.3. The uncertainty of the IP (σ_{IP}) depends on the quality of the track and needs to be small compared to the IP itself to ensure that we see a displaced track rather than a statistical fluctuation. Thus, we define the significance of the IP to be IP/σ_{IP} . For the top quark mass analysis, we consider a jet to be b -tagged if $IP/\sigma_{IP} > 1.7$ for the track with the second highest significance [76].

We do not use b -tagging as part of the event selection, but if there are more than two jets in the event, it is used to select the two used in $t\bar{t}$ reconstruction. If there are two or more b -tagged jets, the two b -tagged jets leading in p_T are used. If there are fewer than two b -tagged jets, the other jets (likewise ordered in p_T) are used to supplement the jet selection. This b -tag driven method of selecting the jets is better at correctly identifying the b -jets than simply taking the leading jets. The fractions of jets correctly matched using the two methods on simulated $t\bar{t}$ events are shown in Table 5.1. The improvement in the fraction of events where both b -jets are selected is about 16% and this leads to approximately a 15% improvement in the statistical uncertainty of the mass measurement.

	Leading jets	b -tag driven jets
2 matched jets	0.579	0.672
1 matched jet	0.379	0.307
0 matched jets	0.042	0.021

Table 5.1: Fraction of simulated $t\bar{t}$ dilepton events with 0, 1 or 2 matched b -jets according to the choice of jets.

The numbers of b -tagged jets in events with two jets and two leptons and after the full selection are shown in Figure 5.4. The bins with low b -tagged jet multiplicity are dominated by Drell-Yan and thus have an excess of events in data, but this effect diminishes as the fraction of $t\bar{t}$ events in the sample increases. The p_T and η of b -tagged jets are shown in Figures 5.5 and 5.6 for events with two jets and two leptons and in Figures 5.7 and 5.8 for events passing the full selection. The data is well-described by the simulation.

Selection cut	Data	Total expected	$t\bar{t}$ signal	Total background
= 0 b -tag	19	$15.9 \pm 0.6^{+13}_{-8}$	$6.9 \pm 0.2^{+7}_{-3}$	$9.0 \pm 0.6^{+6}_{-5}$
= 1 b -tag	35	$40.9 \pm 0.5^{+17}_{-14}$	$35.7 \pm 0.4^{+9}_{-8}$	$5.1 \pm 0.4^{+8}_{-6}$
≥ 2 b -tags	48	$51.7 \pm 0.5^{+14}_{-16}$	$49.5 \pm 0.5^{+11}_{-15}$	$2.2 \pm 0.2^{+3}_{-1}$
Total	102	$108.4 \pm 0.9^{+3}_{-2}$	$92.1 \pm 0.7^{+2}_{-1}$	$16 \pm 1^{+1}_{-1}$

Table 5.2: Events after the final selection split by b -tagged multiplicity. Both statistical uncertainties and systematic uncertainties from jet energy scale variation and b /mis-tagging efficiency variation are shown. The 4% uncertainty due to the luminosity is not included.

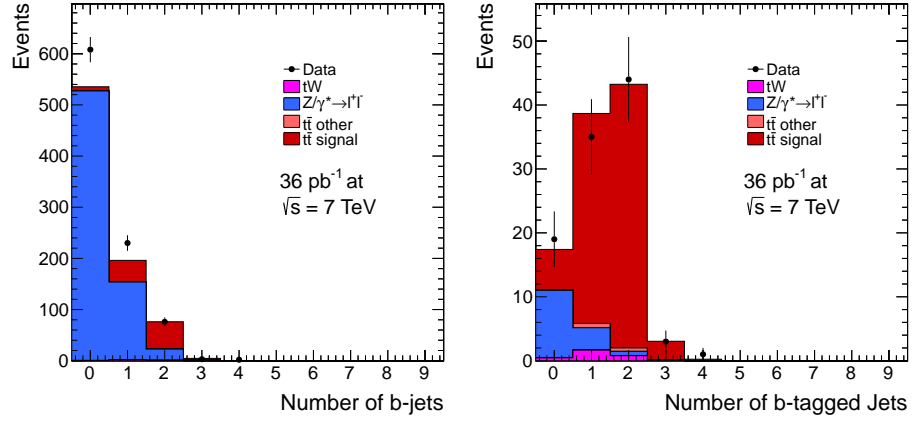


Figure 5.4: The number of b -tagged jets in events with two leptons and two jets (left) and the number of b -tagged jets after the full selection (right).

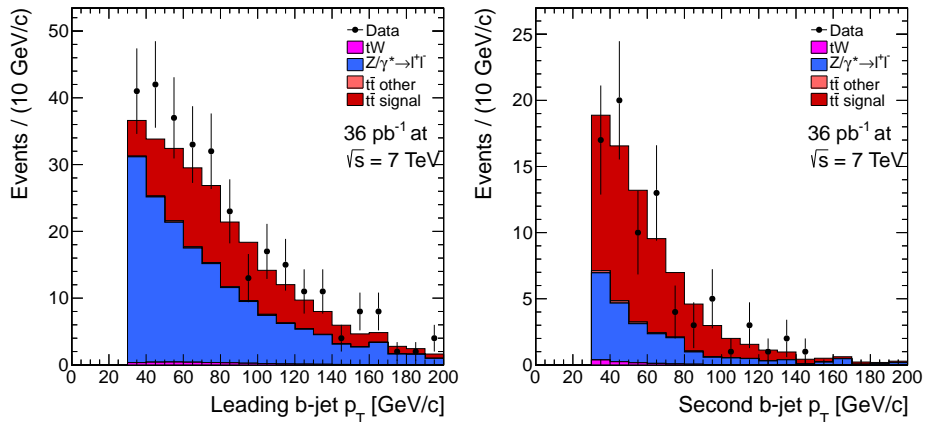


Figure 5.5: The p_T of the leading b -tagged jet (left) and second b -tagged jet (right) in events with at least two jets and two leptons.

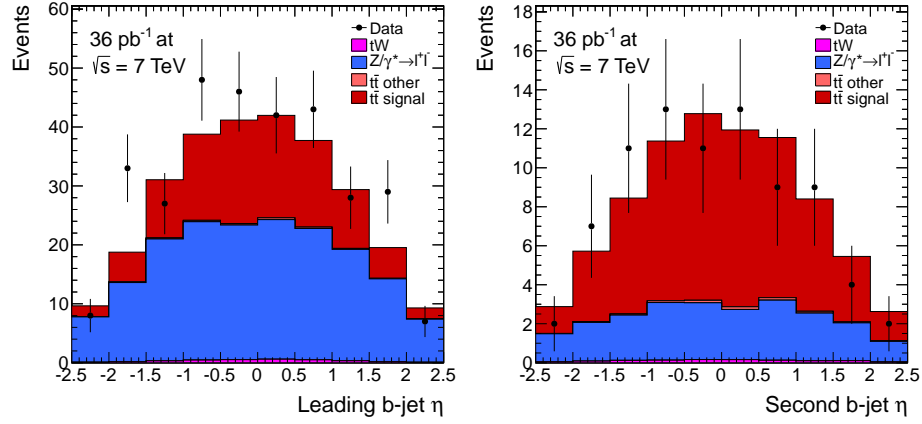


Figure 5.6: The η of the leading b -tagged jet (left) and second b -tagged jet (right) in events with at least two jets and two leptons.

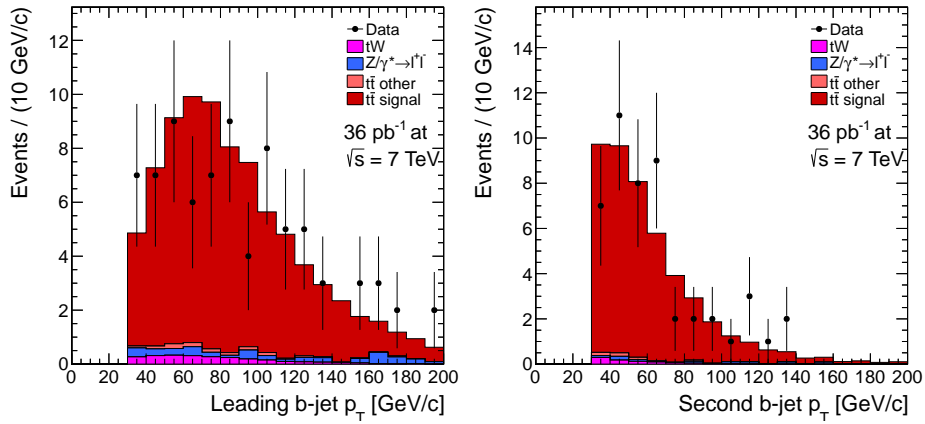


Figure 5.7: The p_T of the leading b -tagged jet (left) and second b -tagged jet (right) after the full selection.

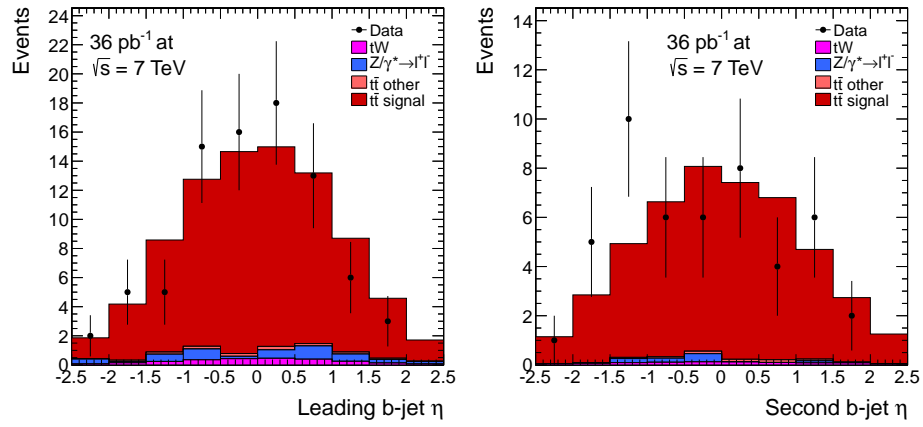


Figure 5.8: The η of the leading b -tagged jet (left) and second b -tagged jet (right) after the full selection.

Chapter 6

Event Reconstruction

6.1 Event Kinematics

A top quark mass estimator for each event is obtained by reconstructing the $t\bar{t}$ system. The reconstruction of the event is performed using the Analytical Matrix Weighting Technique (AMWT) which is based on the Matrix Weighting Technique used at DØ [77]. Dilepton $t\bar{t}$ events have six particles in the final state: two charged leptons, two b-quarks and two neutrinos. The charged leptons are observed and the b-quarks result in jets which are also observed, but the neutrinos are only visible as $\vec{\cancel{E}}_T$.

All final state particle masses are assumed to be small so there are a total of six unknowns. The kinematics of the event give us five constraints: one each from momentum balance in x and y , two from each lepton and neutrino pair having the invariant mass of the W -boson and one from the top and antitop quarks having the same mass. Thus, the system is under-constrained. We deal with this by using the mass of the top quark itself as the missing constraint to analytically solve for the four-momenta of the neutrinos. To measure the top quark mass, we iterate over values of the mass from 0 to 700 GeV/ c^2 in 1 GeV/ c^2 steps and give each of them a weight.

Given a value of the top quark mass, the dilepton $t\bar{t}$ decay can be described by

the following system of equations:

$$\vec{E}_T = \vec{p}_T^\nu + \vec{p}_T^{\bar{\nu}} \quad (6.1a)$$

$$E_\nu = |\vec{p}_\nu| \quad (6.1b)$$

$$E_{\bar{\nu}} = |\vec{p}_{\bar{\nu}}| \quad (6.1c)$$

$$m_{W^+}^2 = (p_\nu + p_{\ell^+})^2 \quad (6.1d)$$

$$m_{W^-}^2 = (p_{\bar{\nu}} + p_{\ell^-})^2 \quad (6.1e)$$

$$m_t^2 = (p_\nu + p_{\ell^+} + p_b)^2 \quad (6.1f)$$

$$m_{\bar{t}}^2 = (p_{\bar{\nu}} + p_{\ell^-} + p_{\bar{b}})^2. \quad (6.1g)$$

We solve these using the analytical method from [78, 79] except for rare events for which this method has an irreducible singularity. In this case we use the numerical method from [80]. According to [78], the transverse momentum of the neutrino can be constrained to a pair of ellipses in the p_x - p_y plane as shown in Figure 6.1. This corresponds to a quartic equation which may have zero, two or four solutions. Because we cannot match the jets to the b and \bar{b} quarks, there are two possible lepton-jet assignments and each event may have up to 8 solutions for any value of the top quark mass.

6.2 Solution Weighting

In order to determine the most likely value of the top quark mass in an event, each solution is given a weight as in [81]:

$$w = \left\{ \sum F(x_1)F(\bar{x}_2) \right\} p(E_{\ell^+}^* | m_t) p(E_{\ell^-}^* | m_t). \quad (6.2)$$

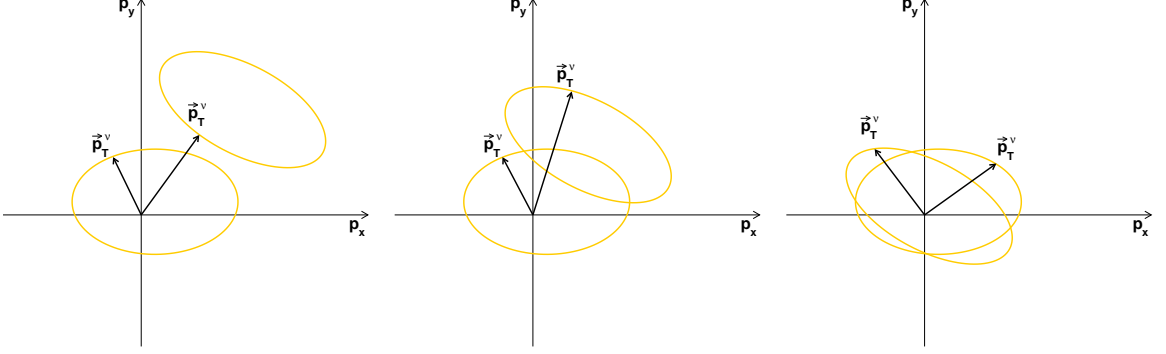


Figure 6.1: p_T of the neutrino in dilepton $t\bar{t}$ decays for events with zero (left), two (center) and four (right) solutions.

Here, x_1 and x_2 are the Björkén x values for the initial state partons, $F(x)$ is the parton distribution function (PDF) for x evaluated at $Q^2 = m_t^2$ and $p(E^*|m_t)$ is the probability of observing a charged lepton of energy E^* in the rest frame of the top quark if the top quark mass has a value m_t .

The PDFs are taken from CTEQ6.1 [82] and accessed using LHAPDF [83]. Each PDF is the probability of finding a parton in the proton that carries the specified momentum fraction. The product of PDFs is summed over all possible leading order initial state partons

The term $p(E^*|m_t)$ is computed in [81]:

$$p(E^*|m_t) = \frac{4m_t E^* (m_t^2 - m_b^2 - 2m_t E^*)}{(m_t^2 - m_b^2)^2 + M_W^2 (m_t^2 - m_b^2) - 2M_W^4}. \quad (6.3)$$

The product of $p(E^*|m_t)$ for the positive and negative leptons is a measure of the $t\bar{t}$ system decaying into the observed in the event. Thus, the weight for any given solution is proportional to the probabilities of both the production and the decay of the $t\bar{t}$ pair. The total weight for each hypothesized value of the top mass is the sum of the weights of all solutions for that mass. The top quark mass estimator for each event is the mass value with the highest total weight. We call this the “peak mass”.

Distributions of the total weight (called “weight curves”) in top quark candidate

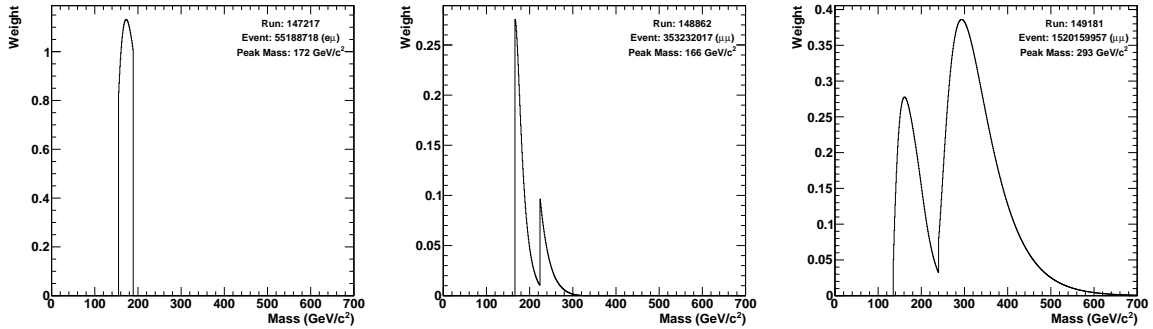


Figure 6.2: Distributions of the total weight in top quark candidate events in data.

events are shown in Figure 6.2. The structure of the weight curves depends on the number of lepton-jet assignments for which there exists a solution. In events for which only one lepton-jet combination gives a solution (Figure 6.2 left), there is typically a single peak whereas the double peaks result from both combinations having solutions. In $t\bar{t}$ simulation, the taller of the two peaks corresponds to the correct jet-lepton assignment 70% of the time.

Peak mass distributions for simulated dilepton $t\bar{t}$ events with the input mass of the top quark equal to $172 \text{ GeV}/c^2$ are shown in Figure 6.3. The peak mass is correlated with the mass of the top quark, but because of the ISR and FSR, detector resolution effects and the bias due to the event selection, it does not give us an unbiased estimate of the top quark mass. The presence of signal in the region beyond $300 \text{ GeV}/c^2$ is due to events in which jets that are not the b-jets were used to reconstruct the $t\bar{t}$ system.

6.3 Smearing of Jets and \vec{E}_T

For approximately 14% of simulated dilepton $t\bar{t}$ decays, there are no solutions for the neutrino momenta at any value of the top quark mass. This is due partly to ISR and FSR and partly to the resolution of the detector which can lead to mismeasurement

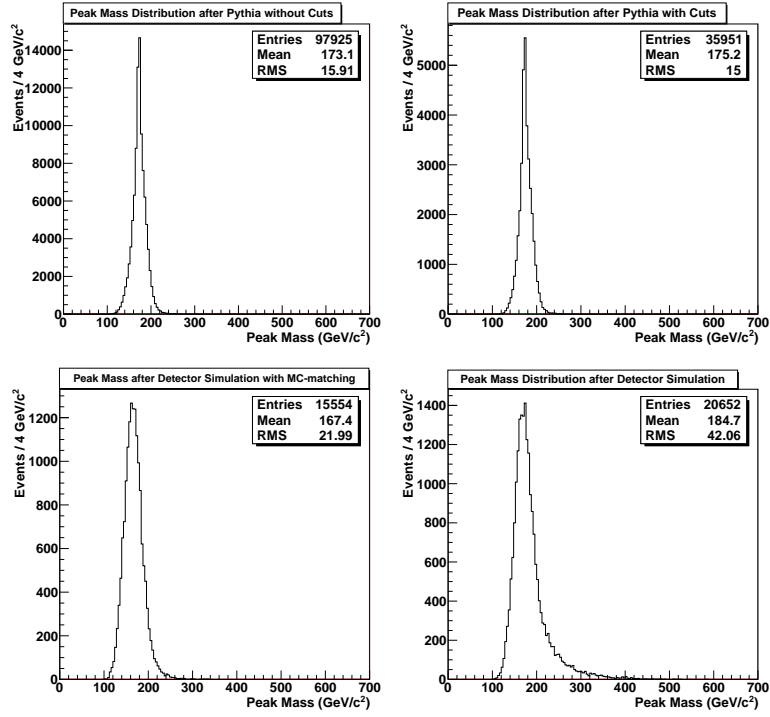


Figure 6.3: Peak mass distributions for an input top quark mass of $172 \text{ GeV}/c^2$. The top row shows distributions after hadronization and before (left) and after (right) the selection cuts. The distributions after simulated detector reconstruction with Monte-Carlo truth matching for b-jets (left) and without any generator level information (right) are in the bottom row.

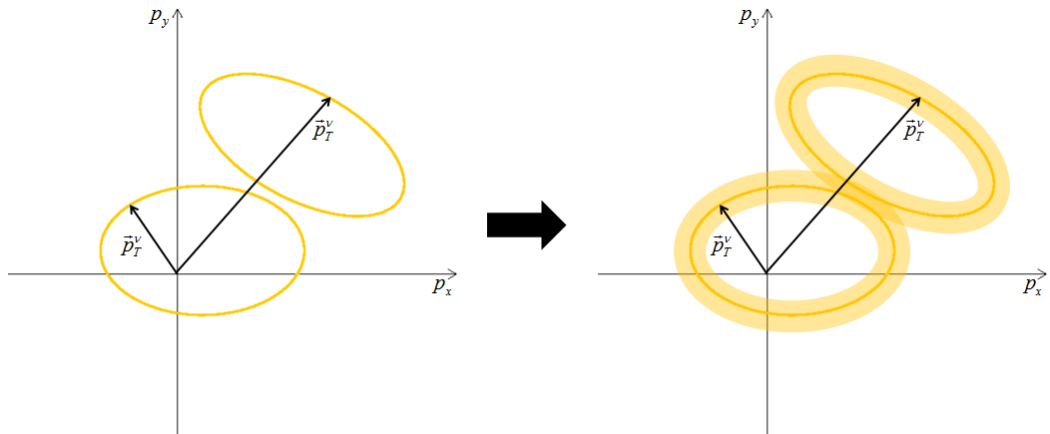


Figure 6.4: The effect of the jet and \vec{E}_T smearing on neutrino momenta. Events with no solutions at ellipse intersections may have solutions in the region of overlap.

of the reconstructed momenta. The objects which are most likely mismeasured are jets so we smear them in accordance with the detector resolution. Each event is reconstructed multiple times and, each time, the jet momenta are multiplied by a random number drawn from a normal distribution with the width computed according to [84].

Since the \vec{E}_T depends on the jets, it is smeared together with them:

$$E_x^{Smeared} = E_x^{Original} + \Sigma p_x^{Original\ Jets} - \Sigma p_x^{Smeared\ Jets} \quad (6.4a)$$

$$E_y^{Smeared} = E_y^{Original} + \Sigma p_y^{Original\ Jets} - \Sigma p_y^{Smeared\ Jets} . \quad (6.4b)$$

In addition, the x and y components of \vec{E}_T not clustered into jets are smeared by 10% using normal distributions with a mean of 0 and a width of 1.

Each event in the CMS data is smeared 1000 times and each event in simulation is smeared 100 times. The difference in the number of smearings is due to the much larger amount of simulated events. There are on the order of a million events in simulation, but only about a hundred events in data. As a result of this, fluctuations in individual simulated events tend to cancel each other out and are not worth the tenfold increase in the time it takes to process the simulated samples.

The total weight for every mass point is the sum of the weights from all smearings. As shown in Figure 6.4, the smearing increases the probability of finding solutions for the neutrino momenta. In simulated $t\bar{t}$ events, this probability changes from 86% to 96%. The data are consistent with simulation: the number of events with solutions increases from 86 to 98 out of the 102 selected events.

A comparison of weight curves before and after smearing is shown in Figure 6.5. Smearing the jets and E_T makes the weight curves smoother and causes small changes in the value of the peak mass. In most events such changes are less than 3 GeV/ c^2 , although in events with sharp peaks, they can be on the order of 10 GeV/ c^2 (as in

the central plot of Figure 6.5). The weight curves of all data events used for the measurement of the top quark mass are shown in Appendix A.

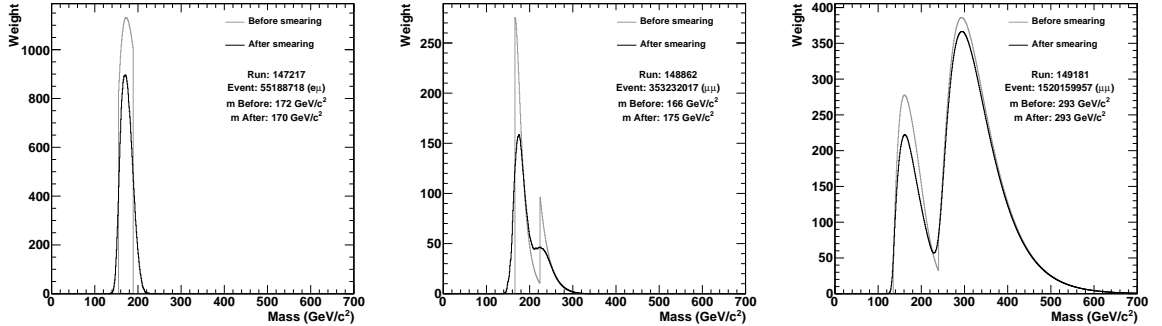


Figure 6.5: Distributions of the total weight in $t\bar{t}$ candidate events in data before and after jet and \cancel{E}_T smearing. The distribution before smearing is scaled by the number of smearings (1000).

6.4 Weight Cut

Background events as well as events with badly reconstructed objects or ISR/FSR jets used for event reconstruction typically yield fewer solutions and these solutions usually have lower weights. As illustrated in Figure 6.6, the peak mass of these events typically depends on either a single anomalous solution or a variation within a jagged peak. Thus, these events are subject to significant fluctuations due to the randomness in the jet smearing and do not yield a reliable estimate of the peak mass. Furthermore, as shown in Figure 6.7, events with low values of the maximum weight (referred to as the “peak weight”) have a much broader peak mass distribution.

To remove the worst of these events, we impose a cut on the peak weight: the average peak weight per smearing must be at least 0.05. In simulation, this requirement removes about 9% of the signal events and about 20% of the Drell-Yan. In data, it removes 7 events in the e^+e^- channel, 2 event in the $e^\pm\mu^\mp$ channel and 4 events in the $\mu^+\mu^-$ channel.

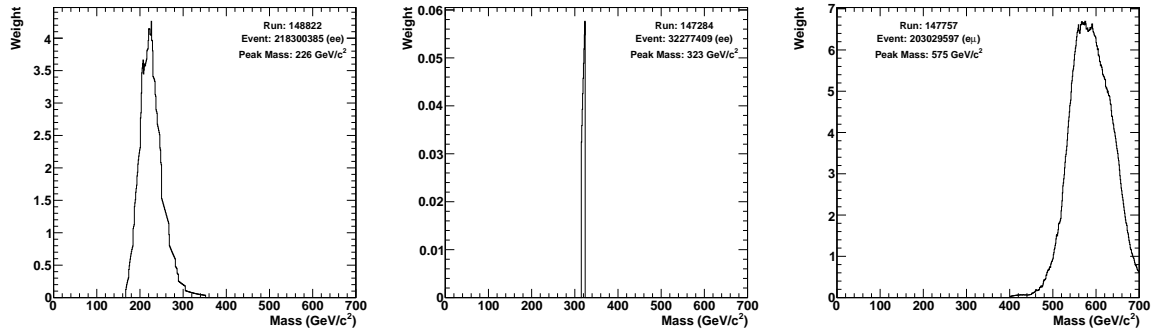


Figure 6.6: Distributions of the total weight in data events rejected by the minimum weight requirement.

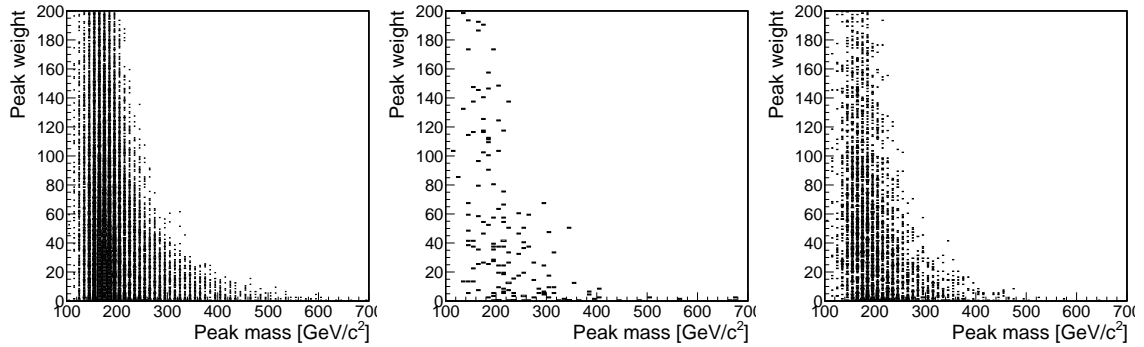


Figure 6.7: Distribution of the peak weight versus the peak mass for simulation of signal events for top quark mass value of $172 \text{ GeV}/c^2$ (left) and the main backgrounds, Drell-Yan (middle) and single top (left).

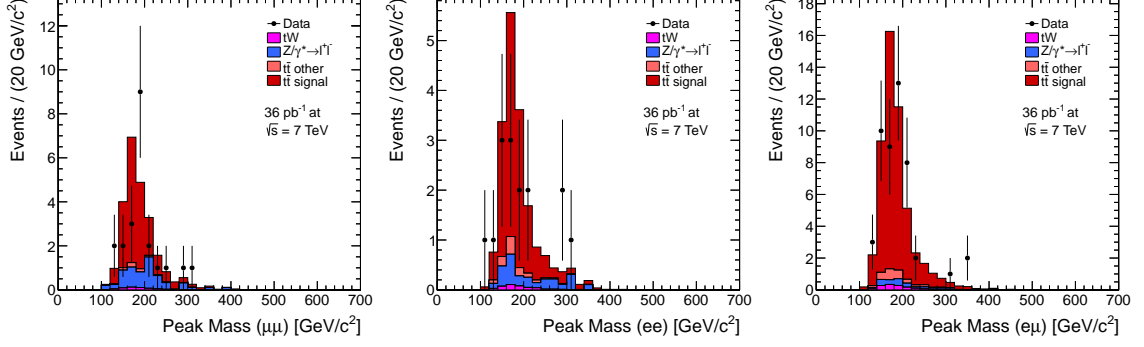


Figure 6.8: The peak mass distributions of data and simulation in the $\mu^+\mu^-$ (left), e^+e^- (center) and $e^\pm\mu^\mp$ (right) channels.

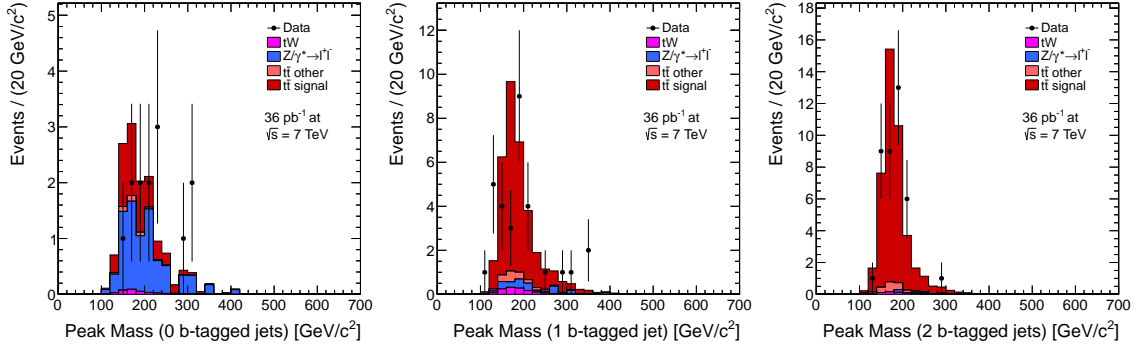


Figure 6.9: The peak mass distributions of data and simulation in events with 0 (left), 1 (center) and 2 (right) b -tagged jets.

6.5 Final Peak Mass Distributions

The distributions of the peak mass split by lepton channel and by the multiplicity of b -tagged jets are shown in Figures 6.8 and Figures 6.9 respectively. Figure 6.10 shows the combined peak mass distribution. There is reasonable agreement between data and simulation with fluctuations in some bins due to the low statistics.

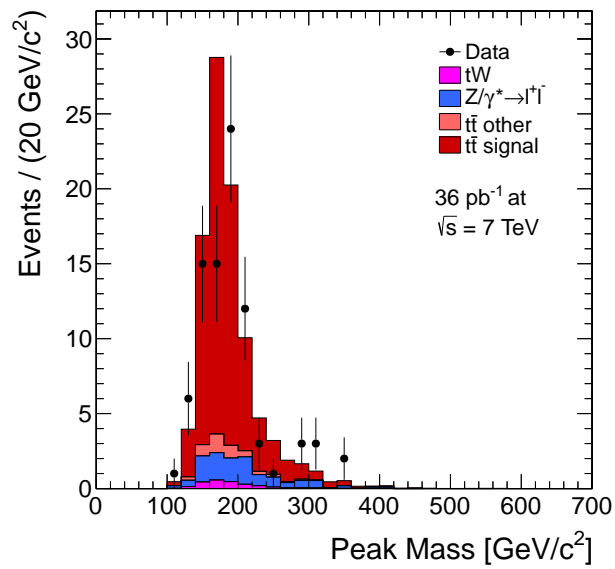


Figure 6.10: The peak mass distribution of all selected events in data and simulation.

Chapter 7

Template Fit

The mass of the top quark is measured by a maximum likelihood fit of the peak mass distribution to templates obtained from simulation. Templates were generated for masses of the top quark between $151 \text{ GeV}/c^2$ and $199 \text{ GeV}/c^2$ in intervals of $3 \text{ GeV}/c^2$. To maximize the number of signal events, all $t\bar{t}$ events in the templates were decayed via the dilepton channel. Figure 7.1 shows the $t\bar{t}$ templates for all seventeen mass points.

As shown in Section 7.3, it is beneficial to split the data sample into multiple categories and use different templates for each category. There are two different ways to classify the events. In the first, the classification is done according to the lepton pair in the decay: e^+e^- , $\mu^+\mu^-$ or $e^\pm\mu^\mp$. In the second, the events are divided based on the number of b -tagged jets used to reconstruct the top quarks. In either case, the templates are fit to the data for each top quark mass hypothesis. All of the events are fitted together in a single likelihood fit, but different templates are used according to the category of the event.

Due to limited computing resources, the total number of events in each template is only about 100,000 and peak mass points that are more than $100 \text{ GeV}/c^2$ away from the input mass are populated with very few events. As a result of this, the tails

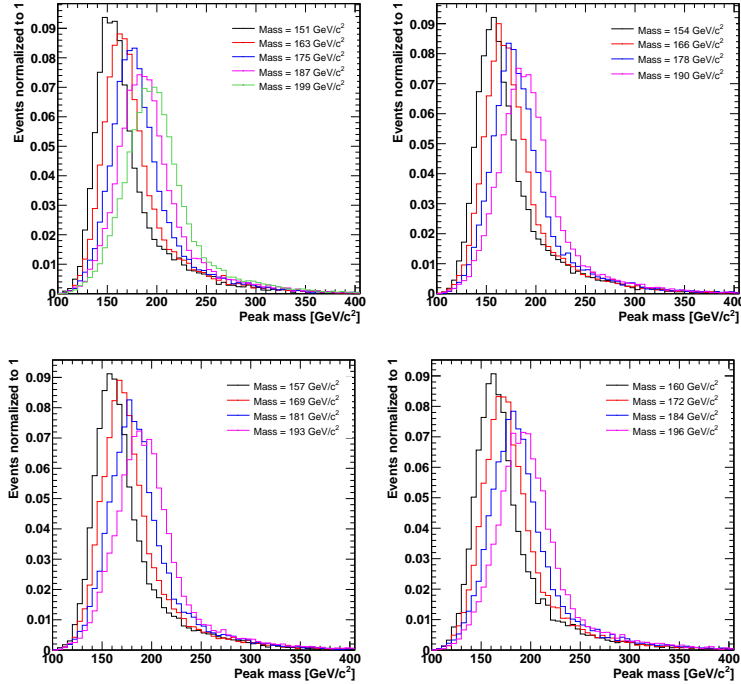


Figure 7.1: Templates for $t\bar{t}$ events generated at different top quark mass values.

of the templates suffer from large statistical fluctuations and fitting the entire peak mass range from 0 to $700 \text{ GeV}/c^2$ introduces a significant amount of noise into the likelihood. To eliminate this problem, we exclude all events with a peak mass above $300 \text{ GeV}/c^2$ from the fits. In the data, this requirement removes 7 events leaving a total of 80 events for the fit.

7.1 Background Estimate

The background of the $t\bar{t}$ sample can be distinguished into two varieties:

- Irreducible backgrounds with two real isolated leptons, such as Drell-Yan, single top in the tW channel and diboson production.
- Instrumental backgrounds with one or two fake isolated leptons. These include the multijet background, W +Jets (where a leptonically decaying W boson occurs in combination with a jet that fakes a lepton and at least two other jets)

and semileptonic $t\bar{t}$ decays in which the second lepton originates from one of the b hadrons.

As shown in [85], the multijet and W +Jets backgrounds are small because of the excellent lepton identification at CMS. The diboson production background has two isolated leptons, but its cross section is more than an order of magnitude smaller than that of $t\bar{t}$ so it is likewise negligible. Thus, the main backgrounds for the top quark mass measurement are Drell-Yan, single top in the tW channel and non-dilepton $t\bar{t}$.

To estimate the effect of each background on the mass measurement, we need the shape of its template and the number of events satisfying our selection requirements. For single top, non-dilepton $t\bar{t}$ and Drell-Yan in the $e^\pm\mu^\mp$ channel, both of these are taken from simulation. Drell-Yan production of leptons of the same flavor is the single largest background and, as shown in section 4.7, it is not well described by the simulation. Therefore, we estimate it using the data-driven $R_{in/out}$ method [85].

7.1.1 The $R_{in/out}$ Method for the Drell-Yan Background

The Drell-Yan background estimate in the e^+e^- and $\mu^+\mu^-$ channels is performed using the numbers of events for which the dilepton invariant mass falls inside and outside the Z -mass window ($76 \text{ GeV}/c^2 < M_{\ell^+\ell^-} < 106 \text{ GeV}/c^2$). These are labeled N_{in} and N_{out} and we assume that their ratio, $R_{in/out} = N_{in}/N_{out}$, is accurately described by the simulation. The numbers of e^+e^- and $\mu^+\mu^-$ events outside the Z -mass window in data are then:

$$N_{out}^{e^+e^-} = R_{in/out}^{e^+e^-} \left(N_{in}^{e^+e^-} - \frac{N_{in}^{e^\pm\mu^\mp}}{2} \times \sqrt{\frac{N_{loose}^{e^+e^-}}{N_{loose}^{\mu^+\mu^-}}} \right), \quad (7.1a)$$

$$N_{out}^{\mu^+\mu^-} = R_{in/out}^{\mu^+\mu^-} \left(N_{in}^{\mu^+\mu^-} - \frac{N_{in}^{e^\pm\mu^\mp}}{2} \times \sqrt{\frac{N_{loose}^{\mu^+\mu^-}}{N_{loose}^{e^+e^-}}} \right). \quad (7.1b)$$

Here, $N_{in}^{e^\pm\mu^\mp}$ is the number of events in the $e^\pm\mu^\mp$ channel and it is subtracted to account for the presence of signal inside the Z -mass window. $N_{in}^{e^\pm\mu^\mp}$ is divided by 2 to account for the different branching ratio of the $e^\pm\mu^\mp$ channel compared to the e^+e^- or $\mu^+\mu^-$ channels. The multiplication by the square root of the ratio of numbers of events with a loose selection is done to correct for difference in reconstruction efficiency between electrons and muons. $N_{loose}^{l^+l^-}$ is the number of events with oppositely charged leptons of the specified flavor without any further selections.

The method was first tested in simulation using single top, dilepton $t\bar{t}$ and Drell-Yan events. We compared the prediction of the method in detector simulation to the number of events at the level of the Monte-Carlo generator and found a good agreement. The results of the tests in simulation and the estimate in data are summarized in Table 7.1. Only statistical uncertainties are presented. To verify the robustness of the method, it was also used on a sample of events obtained by removing the \cancel{E}_T selection. The results are also shown in Table 7.1 and demonstrate a good agreement between data, simulation and Monte-Carlo truth.

After Final Selection				
Samples	Monte-Carlo Truth	Simulation	Data	
e^+e^-	1.6 ± 0.3	1.4 ± 0.6	3.3 ± 0.7	
$\mu^+\mu^-$	3.5 ± 0.4	3.1 ± 1.2	8.4 ± 1.6	
No \cancel{E}_T Selection				
Samples	Monte-Carlo Truth	Simulation	Data	
e^+e^-	23.6 ± 1.0	21.7 ± 1.3	21.9 ± 1.3	
$\mu^+\mu^-$	31.1 ± 1.2	28.6 ± 1.5	31.8 ± 1.6	

Table 7.1: Estimated Drell-Yan background contamination.

The results presented in Table 7.1 do not account for the probability for an event to not have any solutions or to fail the minimum peak weight requirement. The fractions of simulated events that satisfy this requirement in each lepton channel are shown in Table 7.2. With these factors properly accounted for, the predicted numbers of Drell-Yan background events are 2.1 ± 0.7 events in the e^+e^- channel and 5.6 ± 1.7

events in the $\mu^+\mu^-$ channel.

e^+e^-	0.658 ± 0.077
$e^\pm\mu^\mp$	0.836 ± 0.050
$\mu^+\mu^-$	0.670 ± 0.051

Table 7.2: Fractions of simulated Drell-Yan events that satisfy the minimum peak weight requirement.

7.1.2 Peak Mass Template for the Drell-Yan Background

In addition to the number of Drell-Yan events, we also need the shape of the peak mass template for Drell-Yan. To obtain it, we use simulation to verify that the shapes inside and outside the Z -mass window are similar and then derive the shape from data events satisfying all selection requirements except for the Z -veto of the dilepton invariant mass. The peak mass distributions for the e^+e^- and $\mu^+\mu^-$ channels are similar so they are combined to increase the statistics. In order to get a smooth distribution for the template, we fit the peak mass with a Landau distribution convoluted with a Gaussian distribution as shown in Figure 7.2. The final Drell-Yan peak mass template is then produced using 5 million random values drawn from the fitted function.

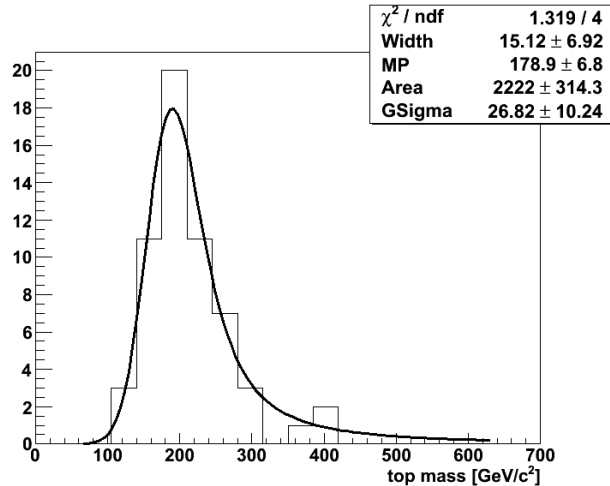


Figure 7.2: Drell-Yan peak mass distribution from data fitted with a Landau convoluted with a Gaussian.

7.1.3 b -tagging Classification for Drell-Yan

Since most Drell-Yan events are not expected to have bottom quarks, it is reasonable to assume that the template derived from data does not change with the number of b -tagged jets. Thus, the Drell-Yan template for each b -tagging category is constructed by reweighting the overall template by the expected fraction of events in each category. The number of expected events for each b -tagging category is shown in Table 7.3. Single top and $t\bar{t}$ decays result in real b -jets, so simulated samples of these processes are used without reweighting.

Sample	PF		
	0 b -tags	1 b -tag	2 b -tags
single top tW	0.4	1.3	0.7
Z +Jets	7.0	1.9	0.5
$t\bar{t}$ background	0.4	1.7	2.1
$t\bar{t}$ signal	5.0	27.7	39.3

Table 7.3: Expected number of events in each sample according to the number of b -tagged jets used.

7.2 Likelihood

To perform the likelihood fit, we first define the probability density function

$$P(x) = f_s S(x) + (1 - f_s) B(x). \quad (7.2)$$

In this context, f_s is the fraction of signal in the data, x corresponds to the peak mass, $S(x)$ is the peak mass template of a signal sample normalized to 1 as in Figure 7.1 and $B(x)$ is the peak mass distribution of the background normalized to 1. The fit can be done with f_s set to the value found using simulation and the data-driven estimate

or f_s can be allowed to vary. In either case, the likelihood function is

$$\mathcal{L} = \prod_{i=1}^N P(x_i). \quad (7.3)$$

Here, N is the number of events in data and $P(x_i)$ is the peak mass is the probability density function evaluated at the peak mass value of the i^{th} event. If f_s is fixed to the expected value, then there are no free parameters and the likelihood is simply the above product. If f_s is allowed to vary, then there is one free parameter and the $-\log(\text{likelihood})$ needs to be minimized for each of the signal templates. The minimization is performed using MINUIT [86].

Once we have obtained the likelihood for all of the signal templates, we fit a quadratic polynomial to the $-\log(\text{likelihood})$ distribution. This final fit is performed over a range of $\pm 12 \text{ GeV}/c^2$ in top quark mass around the lowest of the seventeen mass points. The $\pm 12 \text{ GeV}/c^2$ range was chosen because it consistently yields pull widths closer to unity.

7.3 Study of the Method in Simulation

To study the likelihood fit, we perform several ensemble tests corresponding to different integrated luminosities. For each test, a large number of pseudo-experiments is generated for different hypotheses of the top quark mass. In each pseudo-experiment, signal and background events are generated in each channel using Poisson statistics with the mean set to the number of expected events in each channel. The total number of events is constrained to be 80 as observed in the data and a multinomial is used to determine the number of events from each process for each pseudo-experiment. The likelihood fit is performed as described in Section 7.2 and the measured top quark mass is compared to the hypothesis. To characterize the residual distributions, a Gaussian is fitted to the distribution and the mean of this Gaussian is taken to be

the mean measured mass. The standardized residual (or pull) distribution is likewise fitted with a Gaussian and the standard deviation is taken to be the pull width. Pull distributions for the $172 \text{ GeV}/c^2$ mass point with the events classified by lepton channel and by b -tagging multiplicity are shown in Figure 7.3.

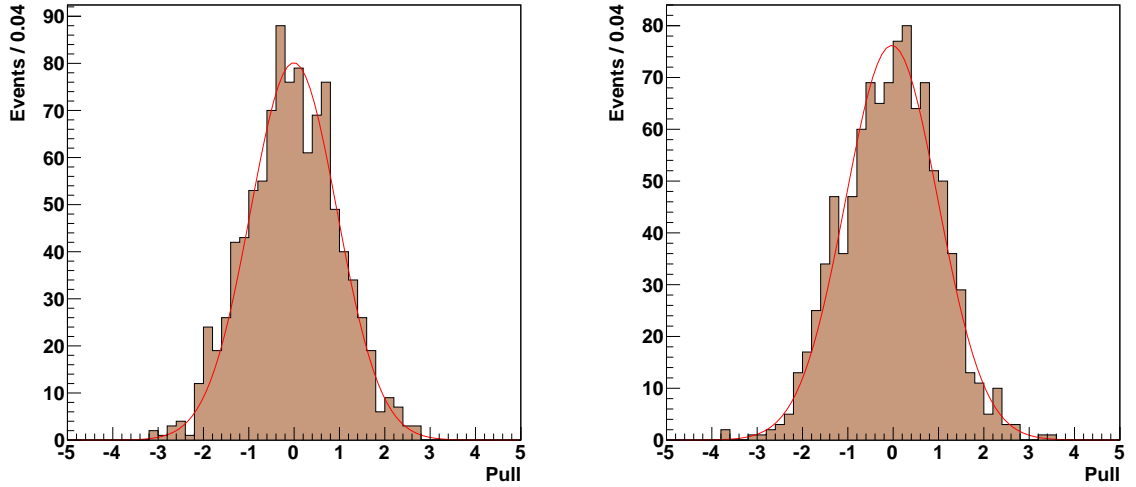


Figure 7.3: Pull distributions for $172 \text{ GeV}/c^2$ mass point with the events classified by b -tagging multiplicity (left) and by lepton channel (right).

The ensemble tests were used to compare the two data classification methods described above. The results for classification by lepton pair and by b -tag multiplicity are shown in Figures 7.4 and 7.5 respectively. Their performance is similar when comparing the mean fitted mass and the mean pull width, but the mean uncertainty is lower when classifying the events according to the number of b -tagged jets used to reconstruct the $t\bar{t}$ system. In fact, the uncertainty using lepton classification is approximately the same as without any classification at all. The uncertainties are summarized in Table 7.4. Hereafter, we classify the data using b -tag multiplicity to minimize the statistical uncertainty.

Further studies of the likelihood fit have been performed for integrated luminosities of 35 and 100 pb^{-1} . For these studies, the total number of events is taken from a Poisson distribution with the mean equal to the expected number of events with the

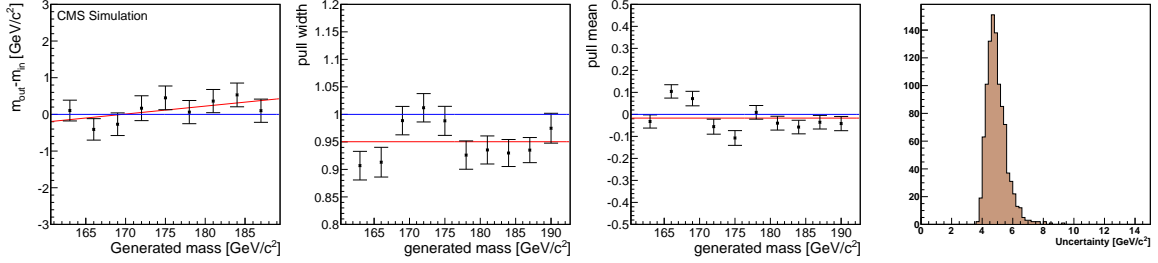


Figure 7.4: Mean measured mass (left), pull (middle left) width and pull mean (middle right) for different mass hypotheses with 80 events, when classifying the events according to the lepton decay channel. Right: distribution of uncertainties of the ensemble tests for a mass hypothesis of $172 \text{ GeV}/c^2$.

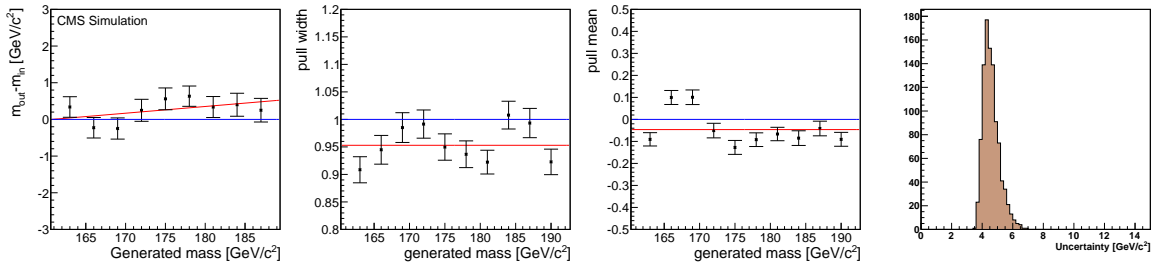


Figure 7.5: Mean measured mass (left), pull (middle left) width and pull mean (middle right) for different mass hypotheses with 80 events, when classifying the events according to the number of b -tagged jets used to reconstruct the $t\bar{t}$ system (0, 1 or 2 b -tags). Right: distribution of uncertainties of the ensemble tests for a mass hypothesis of $172 \text{ GeV}/c^2$.

Classification	Mean Uncertainty
None	5.0 GeV/ c^2
Lepton Channels	5.0 GeV/ c^2
<i>b</i> -tag Categories	4.6 GeV/ c^2

Table 7.4: Expected mean uncertainty from ensemble tests with different methods of event classification.

given luminosity. The results are shown in Figures 7.6 to 7.9. Three different fits are done, with the number of background events left as a free parameter in the fit (Figures 7.6 and 7.7), fixed to zero (Figures 7.8 and 7.9) or fixed to the expected number of events as derived in Section 7.1 (Figures 7.10 and 7.11). No significant bias is observed when the number of background events is fixed to the expected value. When the background is neglected, a bias is introduced for higher integrated luminosities. Finally, when the number of background events is left floating, this bias is reduced but not entirely eliminated. Thus, we fix the number of background events to the expected values.

7.4 Result with Data

Using the 80 events found in our data sample, the top quark mass is measured to be $m_t = 176.1 \pm 5.2$ GeV/ c^2 . The distribution of the $-\log(\text{likelihood})$ is shown in figure 7.12 and the fit to the closest template (with simulated $m_t = 175$ GeV/ c^2) is shown in figure 7.13. This result must be corrected for the bias introduced by the fit. The correction is derived from the calibration curves shown in Figure 7.5. We fit a straight line to the calibration curve and evaluate the bias correction to be 0.3 GeV/ c^2 . The average pull width indicates that the uncertainties are overestimated by 4%. With these corrections, the mass of the top quark is measured to be $m_t = 175.8 \pm 4.9$ GeV/ c^2 .

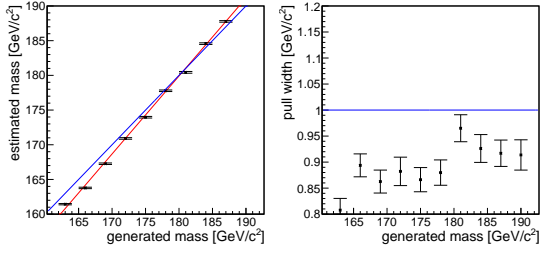


Figure 7.6: Mean measured mass and pull width for different mass hypotheses for an integrated luminosity of 100 pb^{-1} . The background is left floating.

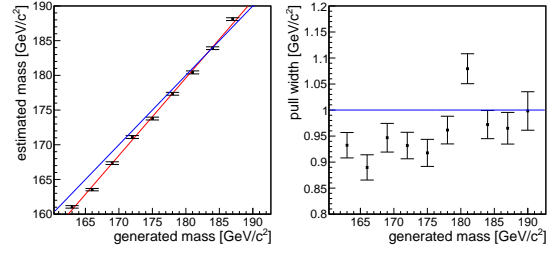


Figure 7.7: Mean measured mass and pull width for different mass hypotheses for an integrated luminosity of 35 pb^{-1} . The background is left floating.

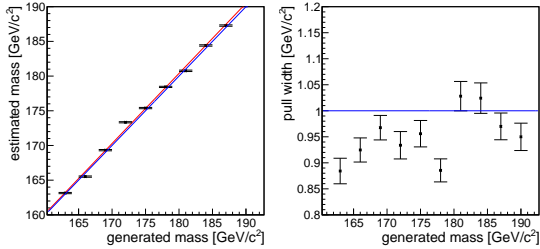


Figure 7.8: Mean measured mass and pull width for different mass hypotheses for an integrated luminosity of 100 pb^{-1} . The background is set to the number of expected events in the likelihood fit.

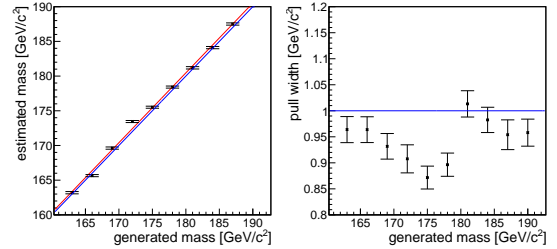


Figure 7.9: Mean measured mass and pull width for different mass hypotheses for an integrated luminosity of 35 pb^{-1} . The background is set to the number of expected events in the likelihood fit.

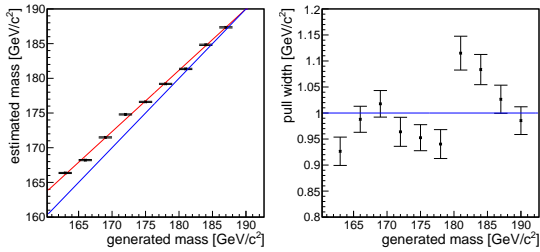


Figure 7.10: Mean measured mass and pull width for different mass hypotheses for an integrated luminosity of 100 pb^{-1} . The background is set to 0 in the likelihood fit.

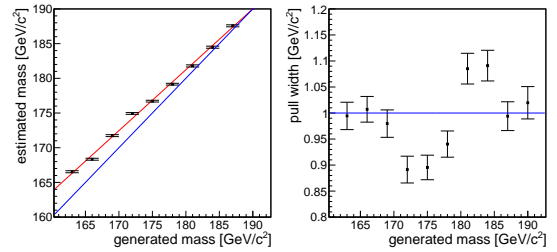


Figure 7.11: Mean measured mass and pull width for different mass hypotheses for an integrated luminosity of 35 pb^{-1} . The background is set to 0 in the likelihood fit.

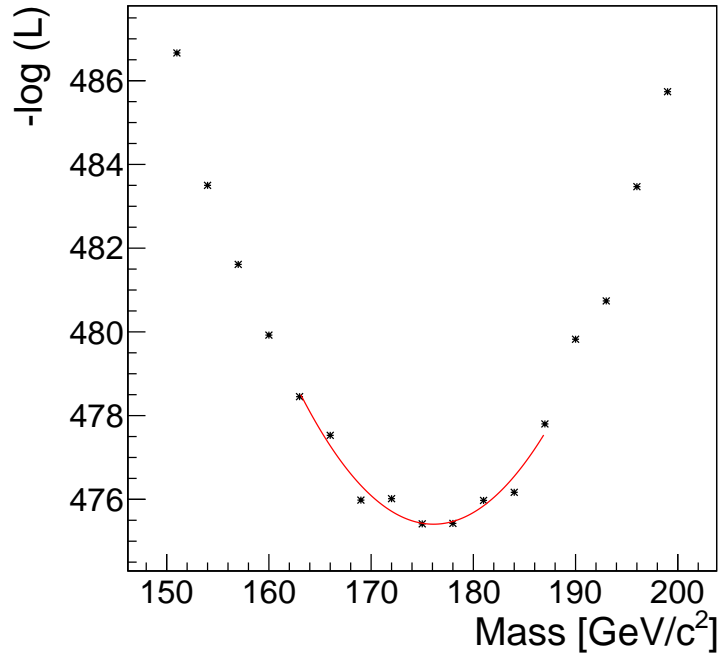


Figure 7.12: Distribution of the $-\log(\text{likelihood})$ points for data.

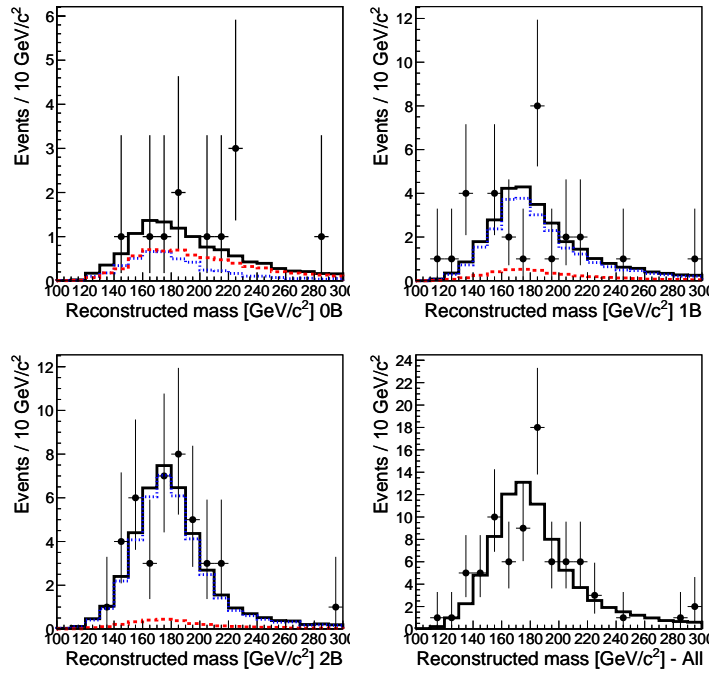


Figure 7.13: Fit of the data to the templates obtained in the simulation for a top mass hypothesis of $175 \text{ GeV}/c^2$.

Chapter 8

Systematic Uncertainties

All systematic uncertainties are evaluated using pseudo-experiments. For each uncertainty, a peak mass template is generated with the relevant changes and the top quark mass from this template is measured using 1000 pseudo-experiments with 80 events each. The uncertainty is taken to be the difference of the average mass in the varied template and the average mass in a reference template. When a parameter is varied in opposite directions and the variation in the positive and negative uncertainties is within the uncertainty due to template statistics, the mean of the positive and negative uncertainties is used.

8.1 Jet Energy Scale

The dominant systematic uncertainty is due to the energy scale of b-jets used for the reconstruction of the $t\bar{t}$ system. It is computed in two steps. First, an uncertainty for all flavors of jets is calculated by varying each jet based on its p_T and η as described in [74]. The average variation in the energy of the jets is approximately 3% and this results in a $3.0 \text{ GeV}/c^2$ uncertainty in the measured top quark mass. In the second step, we derive the uncertainty specific to b-jets by varying the jets used in $t\bar{t}$ reconstruction by 2% if they fall within $|\eta| < 2$ and $50 < p_T < 200 \text{ GeV}/c$ or by

3% if they do not. The resulting uncertainty of $2.5 \text{ GeV}/c^2$ is added in quadrature to the inclusive jet uncertainty.

8.1.1 Jet Energy Scale Cross-Check

To measure the top quark mass using fits to simulated templates, it is essential that the jets from data and simulation are calibrated to the same relative energy scale. In the dilepton channel, there are no absolute mass constraints that involve jets. Thus, the absolute calibration of the jet energy scale is of secondary importance because any miscalibration in the data would be compensated by a corresponding miscalibration in the simulation.

Events with Z decays to two leptons (e^+e^- , $\mu^+\mu^-$) that recoil against a single jet provide an ideal laboratory to cross-check the calibration of the jet energy scale. The precisely reconstructed leptons provide a measurement of the p_T of the Z boson which has to be balanced by the p_T of the jet against which it recoils. Figure 8.1 shows the invariant mass spectrum of the two-lepton system. Here and in all other plots in this section, black points represent data and histograms with a solid line represent the simulation of Drell-Yan Z/γ^* production.

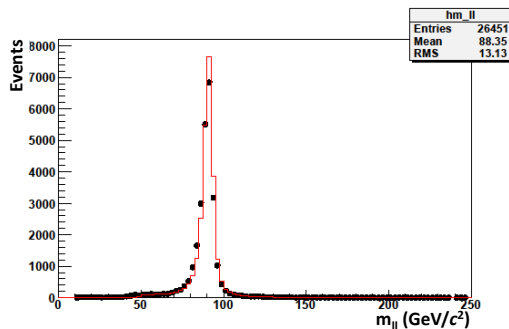


Figure 8.1: Dilepton mass spectrum from events with e^+e^- or $\mu^+\mu^-$.

In order to minimize contamination from other processes that have leptons in the final state, we restrict the invariant mass of the dilepton system to the interval $80 \text{ GeV}/c^2 < M_{\ell^+\ell^-} < 100 \text{ GeV}/c^2$. The jets and leptons used for this study must

satisfy the same requirements as those used for reconstruction of the $t\bar{t}$ system, but to reduce biases, the jet p_T requirement is relaxed to $p_T > 10 \text{ GeV}/c$ and the dilepton p_T is required to be more than $20 \text{ GeV}/c$. There is fairly good agreement between data and simulation as shown in Figure 8.2.

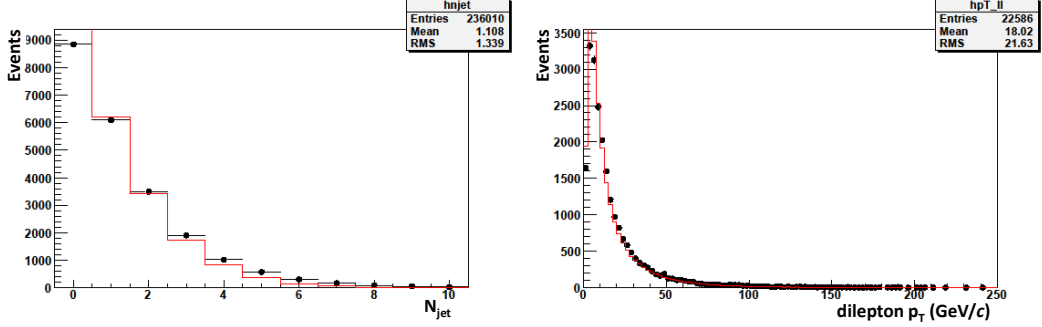


Figure 8.2: Jet multiplicity (left) and dilepton p_T spectra (right).

Events in which a single jet recoils against the dilepton system are selected. To suppress events in which an additional soft jet was radiated, we require $\cos(\Delta\phi)$ to be less than -0.99 where $\Delta\phi$ is the azimuthal difference between the dilepton and jet momenta. Figure 8.3 shows the distribution of $\cos(\Delta\phi)$ for events with exactly one jet.

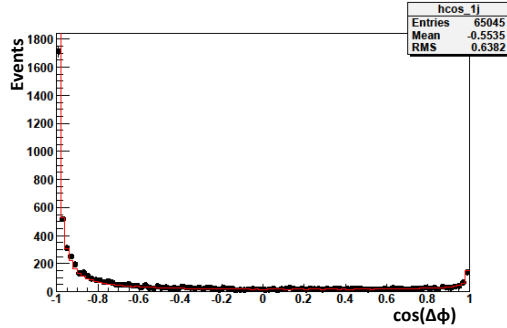


Figure 8.3: Distribution of $\cos(\Delta\phi)$ for events with exactly one jet.

We now project the jet momentum onto the direction of the dilepton p_T and add the dilepton p_T and the jet momentum projection $\vec{p}^{jet} \cdot \vec{p}_T^{\ell\ell} / |\vec{p}_T^{\ell\ell}|$. The quantity $\Delta p_T = p_T^{\ell\ell} + \vec{p}^{jet} \cdot \vec{p}_T^{\ell\ell} / |\vec{p}_T^{\ell\ell}|$ should be zero on average if the jet p_T scale is correctly calibrated relative to the lepton p_T scale. Figure 8.4 shows the observed distributions.

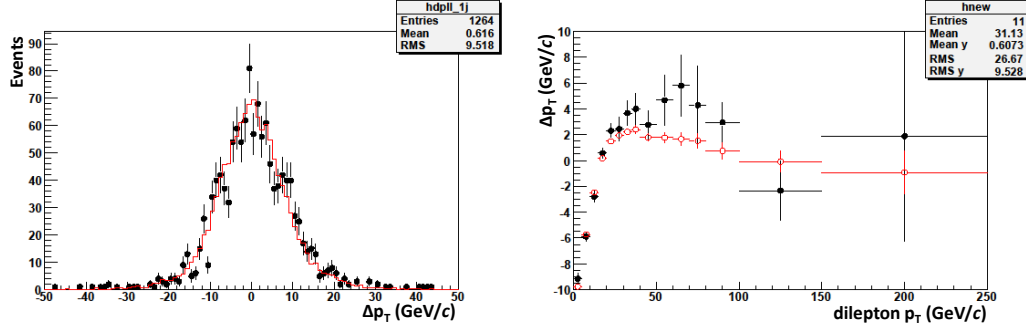


Figure 8.4: Distributions of $\Delta\phi$ (left) and mean $\Delta\phi$ in bins of dilepton p_T (right).

It is apparent in the right plot of Fig. 8.4 that there is a systematic difference between the mean Δp_T values from data and those from simulation. The points for dilepton $p_T < 20$ GeV/ c are biased by the 10 GeV/ c threshold for jet p_T and are not sensitive to the jet energy scale. We scale the jet energies in the simulated events by a factor f_{jes} and compute a χ^2 to characterize the consistency of data and simulation points in this plot. Only the points for dilepton $p_T > 20$ GeV are used to compute the χ^2 . The values of χ^2 obtained for different jet energy scale factors are plotted in Fig. 8.5. The superimposed quadratic fit to the χ^2 values is minimized for $f_{jes} = 0.975 \pm 0.009$.

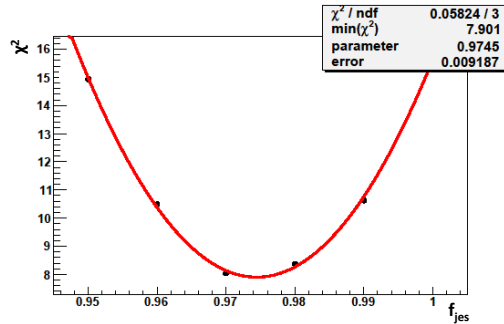


Figure 8.5: Values of χ^2 versus jet energy scale factor f_{jes} .

We thus conclude that there is a small but significant mismatch between the jet energy scales in data and simulation. This mismatch is covered, however, by the uncertainty assigned to the jet energy scale calibration.

8.2 Other Detector Objects

8.2.1 Jet Energy Resolution

The jet energy resolution is varied by changing the p_T difference between the fully simulated jets and the generator-level partons by $\pm 10\%$ [87]. This results in an uncertainty of $\pm 0.5 \text{ GeV}/c^2$.

8.2.2 Lepton Energy Scale

The energy scale of electrons in the ECAL barrel region and of all muons is known to within less than 1% and the associated systematic uncertainty is assumed to be small. As mentioned in Section 4.4, the scale of electrons in the endcap region is slightly worse. Thus, the energy scale of electrons in the ECAL endcaps is varied by $\pm 2.5\%$. This leads to a $\pm 0.3 \text{ GeV}/c^2$ uncertainty.

8.2.3 Missing Transverse Energy

For all above variations of the leptons and jets, the \vec{E}_T is varied to remain consistent with the rest of the event. In addition, the unclustered \vec{E}_T is changed by $\pm 10\%$ [88]. The effect of the latter is only $\pm 0.1 \text{ GeV}/c^2$ so most of the \vec{E}_T uncertainty is included in the jet energy scale uncertainty.

8.2.4 b -tagging

b -tagging relies on the precise measurement of many parameters of tracks originating from jets. While CMS simulation reproduces the data to a remarkable degree, these parameters are difficult to control. Discrepancies between b -tagging in data and in simulation may cause variation in the jets selected for $t\bar{t}$ reconstruction and thus alter the measured top quark mass. To estimate the uncertainty due to b -tagging, we vary

the efficiency of the algorithm by 15% and the mistag rate by 30% [89]. The resulting uncertainty is $\pm 0.5 \text{ GeV}/c^2$.

8.3 Pile-up

As discussed in Section 2.1, the LHC can attain higher instantaneous luminosities by increasing the proton density of the colliding bunches. However, this also increases the number of interactions in a single bunch crossing which causes extra particles in the event. This phenomenon is referred to as “pile-up” and it can be studied by measuring the number of primary vertices in each event. As shown in Figure 8.6, there is more pile-up in data than in simulation. This can result in additional jets and degrade the resolution of $\vec{\cancel{E}}_T$. To account for it, we use a dedicated simulation sample where the amount of pile-up has been increased to an average of approximately two extra events per bunch crossing. The systematic uncertainty due to pile-up is measured to be $\pm 1.1 \text{ GeV}/c^2$.

8.4 Background

To estimate the influence of the number of background events on the fit, the uncertainties presented in Section 7.1 have been used for the number of e^+e^- and $\mu^+\mu^-$ events from Drell-Yan production. An uncertainty of 20% was used for the numbers predicted by simulation for single top and non-dilepton $t\bar{t}$. This value is based on the number of events passing the full selection in simulation. The systematic uncertainty is found to be $\pm 0.2 \text{ GeV}/c^2$. For the shape of the background templates, the Drell-Yan templates from simulation were used instead of those derived from data. The resulting uncertainty in the measured top quark mass is also $\pm 0.2 \text{ GeV}/c^2$.

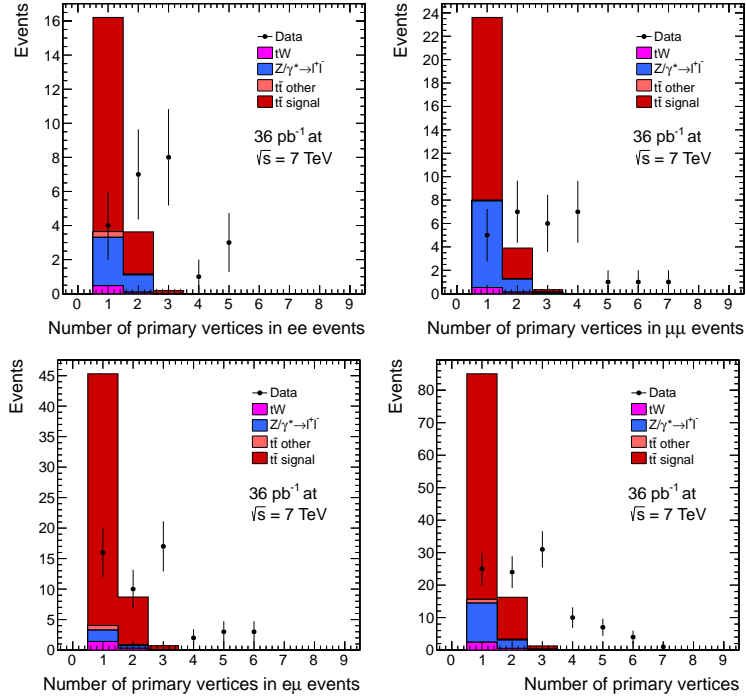


Figure 8.6: The number of vertices in events after the full selection.

8.5 Simulation

The systematic uncertainty in the simulation can be caused by several factors which are listed below. The uncertainties resulting from each of these is given in Table 8.1.

- The uncertainty due to MADGRAPH is estimated by using templates produced by a different Monte-Carlo generator, POWHEG.
- The scale used in the MLM parton-jet matching algorithm and PYTHIA's factorization scale are varied up and down by a factor of 2 and the resulting templates are used to compute the uncertainty due to each.
- The uncertainty resulting from the initial and final state radiation is likewise calculated using dedicated templates where the radiation is varied.
- The uncertainty due to PYTHIA's underlying event model is computed by comparing the Z2 and D6T tunes which are described in [61].

- The CTEQ6.1 parton distribution functions are varied using the 40 values included in the PDF set. The procedure is described in [90].

8.6 Template Fit

The results of the template fit are corrected for any bias in the fitting procedure itself by fitting a straight line to the results obtained from ensemble tests. The parameters of this line are varied by their uncertainties and the largest variation ($\pm 0.1 \text{ GeV}/c^2$) is taken to be the systematic uncertainty. To estimate the uncertainty due to the template statistics, we split the $172 \text{ GeV}/c^2$ sample into four independent templates. The $\pm 0.2 \text{ GeV}/c^2$ variation in the fitted mass of these is taken to be the systematic uncertainty.

8.7 Summary

The systematic uncertainties are summarized in Table 8.1. The total systematic uncertainty is $\pm 4.5 \text{ GeV}/c^2$.

Source	$\Delta m_t(\text{GeV}/c^2)$
Jet energy scale	± 3.0
b-jet energy scale	± 2.5
Jet energy resolution	± 0.5
Lepton energy scale	± 0.3
Missing E_T	± 0.1
b -tagging	± 0.5
Pile-up	± 1.1
Background level	± 0.2
Background shape	± 0.2
Monte-Carlo Generator	± 0.2
Underlying event	± 1.5
Matching	± 0.7
Factorization Scale	± 0.6
ISR/FSR	± 0.2
PDFs	± 0.6
Template statistics	± 0.2
Calibration	± 0.1
Total	± 4.5

Table 8.1: List of systematic uncertainties with their contribution to the total uncertainty.

Chapter 9

b-jet Energy Calibration

The largest contribution to the systematic uncertainty in our top quark mass measurement is the calibration of the *b*-jet energy scale. This scale cannot be measured simultaneously with the top quark mass, but since the latter is known very precisely from the Tevatron, we can reinterpret the analysis and use the top quark mass measurement from the Tevatron to constrain the *b*-jet energy scale. Top quarks decay almost exclusively to bottom quarks and *W*-bosons and while we do not always choose the correct jets, the measurement of the top quark mass is driven by *b*-jets.

To measure the mass of the top quark, we fix the jet energy scale at the value obtained for calibration of generic light quark jets. We then plot the likelihood of the template fits to the distribution of the reconstructed top quark mass from the data versus the top quark mass at which the templates are generated. To constrain the jet energy scale we introduce a single global jet energy scale factor called α . The nominal CMS jet energy scale calibration then corresponds to $\alpha = 1$. The world average value of the top quark mass is $173.3 \text{ GeV}/c^2$ [4]. If we had a template at this mass point, we could solve for the value of α that fits it best. However, since generation and simulation of event samples requires a great deal of computing resources, we lack a template at this exact value. Instead, we use our existing event samples to extrapolate α at the world average top quark mass.

Templates are generated at eight mass points with $163 \leq m_t \leq 184 \text{ GeV}/c^2$ for values of $\alpha = 0.85, 0.87, 0.89, 0.91, 0.93, 0.95, 0.97, 1.03, 1.05, 1.07, 1.09, 1.11, 1.13$ and 1.15 by scaling the jet energy scale in all events by α . We then fit the likelihood for each value of α as a function of the top quark mass and compute the result of the fit for $m_t = 173.3 \text{ GeV}/c^2$. As shown in Figure 9.1, the negative logarithm of the likelihood values at $m_t = 173.3 \text{ GeV}/c^2$ is plotted versus α and fit with a quadratic polynomial to find the minimum. We find that $\alpha = 1.014 \pm 0.047$ agrees best with the data.

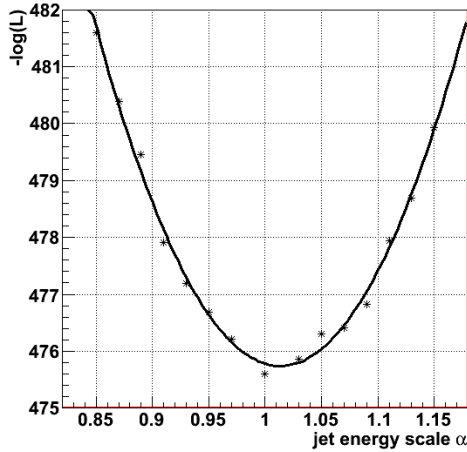


Figure 9.1: Negative logarithm of the likelihood from the fit of templates for $m_t = 173.3 \text{ GeV}/c^2$ to data versus jet energy scale α .

All systematic uncertainties from Section 8.7 except the jet energy scale itself give rise to a total uncertainty of 1.3%. Thus, we can constrain the b -jet energy scale to be

$$\alpha = 1.014 \pm 0.047(stat) \pm 0.013(syst) = 1.014 \pm 0.049. \quad (9.1)$$

With the present data sample, the uncertainty in the b -jet energy scale computed using dilepton $t\bar{t}$ decays is comparable to the same uncertainty calculated with the method from Section 8.1. However, the uncertainty from dilepton $t\bar{t}$ events is predominantly statistical and should rapidly improve with increasing luminosity.

Chapter 10

Conclusion

We have used the AMWT method to measure the mass of the top quark using dilepton $t\bar{t}$ events at the CMS experiment. The measured value of the top quark mass is $m_t = 175.8 \pm 4.9$ (stat) ± 4.5 (syst) GeV/ c^2 . We have also constrained the b-jet energy scale using $t\bar{t}$ events. This is the first such measurement.

10.1 Combination

A separate analysis measuring the top quark mass was performed using the same data. The event selection was identical, but the $t\bar{t}$ system was reconstructed using the KINb method rather than AMWT. Instead of using the mass of the top quark itself as the missing constraint, the KINb method uses the longitudinal balance of the $t\bar{t}$ system. A more detailed explanation of the KINb analysis can be found in [91].

The AMWT and KINb measurements were combined using the Best Linear Unbiased Estimate (BLUE) method [92]. Given a set of measurements m_i ($i = 1, \dots, n$), the combination \hat{m} is linear if it can be expressed as

$$\hat{m} = \sum_i \alpha_i m_i, \quad (10.1)$$

where α_i are constant weights for the individual measurements. If all of the m_i measurements are unbiased, then \hat{m} will also be unbiased if

$$\sum_i \alpha_i = 1. \quad (10.2)$$

Finally, “best” means that the uncertainty on the combined measurement is as low as possible which is equivalent to minimizing the variance:

$$\sigma^2 = \sum_i \sum_j E_{ij} \alpha_i \alpha_j. \quad (10.3)$$

Here, E_{ij} are the entries of the error matrix \mathbf{E} which has the variances of individual measurements as the diagonal elements and correlations between pairs of estimates as the off-diagonal elements. To construct \mathbf{E} , we assume that all of the uncertainties for each of the measurements are uncorrelated.

As described in [92], minimizing the variance is identical to minimizing

$$S = \sum_{ij} (m_i - m') H_{ij} (m_j - m'), \quad (10.4)$$

where \mathbf{H} is the inverse of \mathbf{E} . The value of \hat{m} is then given by

$$\hat{m} = \frac{\sum_{ij} H_{ij} m_j}{\sum_{ij} H_{ij}}. \quad (10.5)$$

The uncertainty from source k in the combined measurement can be obtained using error propagation

$$\delta^{(k)2} = \sum_{ij} \frac{\partial \hat{m}}{\partial m_i} E_{ij}^{(k)} \frac{\partial \hat{m}}{\partial m_j} = \frac{\sum_{imnj} H_{im} E_{mn}^{(k)} H_{nj}}{\left(\sum_{ij} H_{ij}\right)^2}. \quad (10.6)$$

If we add up all the uncertainties in quadrature we get the total uncertainty

$$\delta^2 = \sum_{k=1}^K \delta^{(k)2} = \frac{1}{\sum_{ij} H_{ij}}. \quad (10.7)$$

The statistical correlation between the two methods is determined using pseudo-experiments and found to be 0.57. Systematic uncertainties common to the two methods are assumed to be 100% correlated. A summary of the combination is presented in Table 10.1 and a more detailed description is expounded in [91].

Method	Measured m_t (in GeV/c^2)	Weight
AMWT	175.8 ± 4.9 (stat.) ± 4.5 (syst.)	0.65
KINb	174.8 ± 5.5 (stat.) $^{+4.5}_{-5.0}$ (syst.)	0.35
Combined	175.5 ± 4.6 (stat.) ± 4.6 (syst.)	

Table 10.1: Summary of measured top quark masses for the AMWT and KINb methods with the contributing weights to the combined mass value [91].

Thus, the combined top quark mass measurement from dilepton $t\bar{t}$ events in all data collected by the CMS experiment in 2010 is $m_t = 175.5 \pm 4.6$ (stat) ± 4.6 (syst) GeV/c^2 . This is the first measurement of the top quark mass at the LHC.

10.2 Prospects for the Top Quark Mass at CMS

Measurements of the top quark mass have previously been made at the Tevatron. The most recent of these results in the dilepton channel are $m_t = 171.2 \pm 2.7$ (stat) ± 2.9 (syst) GeV/c^2 for CDF [43] and $m_t = 174.7 \pm 4.4$ (stat) ± 2.0 (syst) GeV/c^2 for DØ [49]. The present measurement does not rival the precision of the Tevatron experiments. However, the dominant uncertainties in the present measurement are due to statistics and to the b -jet energy scale both of which are expected to be significantly reduced in the next iteration of the analysis.

The statistical uncertainty is expected to decrease as we accumulate more inte-

grated luminosity. As of July 2011, CMS has recorded over 1 fb^{-1} of luminosity which is nearly 30 times the 36 pb^{-1} collected in 2010. The LHC is projected to deliver considerably more data, but even with the data currently available, the statistical uncertainty in the top quark mass is expected to be less than $1 \text{ GeV}/c^2$.

The b -jet energy scale used in the measurement is based on an analysis of approximately 3 pb^{-1} of CMS data [74]. The associated uncertainty will diminish with improved jet energy corrections. For example, when the full 36 pb^{-1} of 2010 data are used, the JES uncertainty decreases by about a factor of 2 [93]. With the exception of pile-up, all other systematic uncertainties are likewise projected to decrease.

As described in Section 8.3, the pile-up uncertainty is the result of multiple interactions in a single beam crossing. In 2010, the average number of interactions was approximately 2, but this will increase by at least a factor of 3 in 2011. Pile-up introduces additional jets into the event and degrades the resolution of \vec{E}_T . In dilepton $t\bar{t}$ events, the impact of the extra jets can be mitigated by requiring most tracks from the two jets selected for event reconstruction to originate from the same primary vertex as the leptons. Furthermore, with over an order of magnitude more luminosity, we can afford to use only events with two b -tagged jets for the mass measurement. This will reduce the number of events by a factor of 2, but it will eliminate jets from pile-up since the latter are unlikely to be b -jets. These modifications should allow us to control the pile-up and the next iteration of the top quark mass measurement in the dilepton $t\bar{t}$ channel should exceed the precision of similar analyses at the Tevatron.

10.3 b -jet Energy Calibration

In addition to the measurement of the top quark mass, the method from our analysis can also be used for determining the energy scale of b -jets. This cannot be computed simultaneously with the top quark mass, but it may be useful for understanding other

processes, such as the decay of the Higgs boson to $b\bar{b}$. We have performed the first measurement of the b -jet energy scale using $t\bar{t}$ events. Since the uncertainty on the global b -jet energy factor is almost entirely statistical, we expect it to decrease below 1% with 1 fb^{-1} of integrated luminosity. With even more luminosity from the LHC, the b -jet energy can be determined in bins of p_T and η rather than a single overall factor.

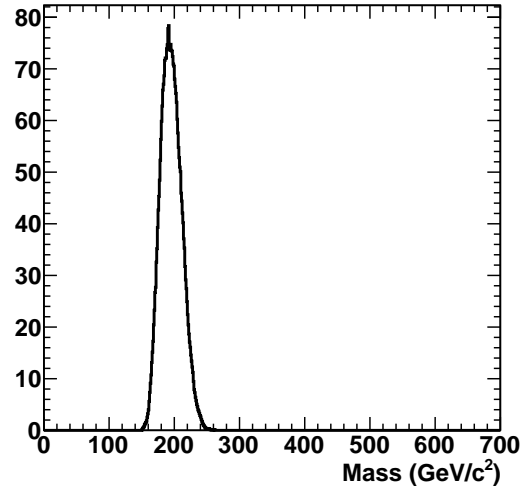
Appendix A

Data Events Used to Measure the Mass of the Top Quark

The properties of the 80 data events used to measure the mass of the top quark are listed below. The Lorentz vectors of the leptons and jets are given in terms of the p_T , η , ϕ and the energy (E) where the transverse momentum is in GeV/ c and the energy is in GeV. The missing transverse energy is likewise in units of GeV. The weight curve for each event is shown to the left of the event properties.

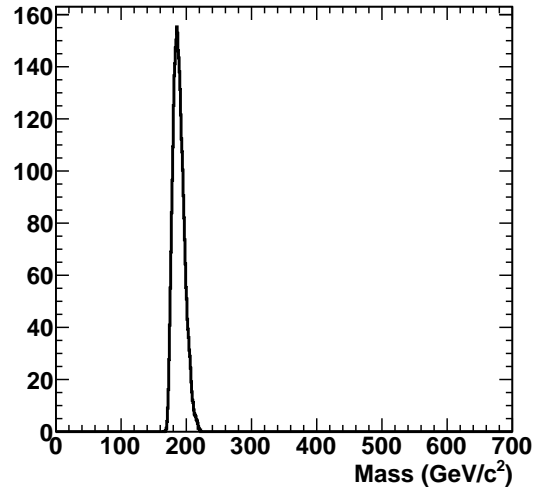
Run: 140379
 Lumi Section: 160
 Event: 136650665
 Peak Mass: 191 GeV/c²
 Peak Weight: 78.38
 b-tagged Jets: 2

	p _T	η	φ	E
μ ⁺	27.14	-2.04	-1.90	106.39
μ ⁻	56.77	-1.43	-2.13	125.09
Jet 1	53.80	0.72	0.03	69.30
Jet 2	52.39	-1.21	0.97	96.20
E _T	55.65		2.26	



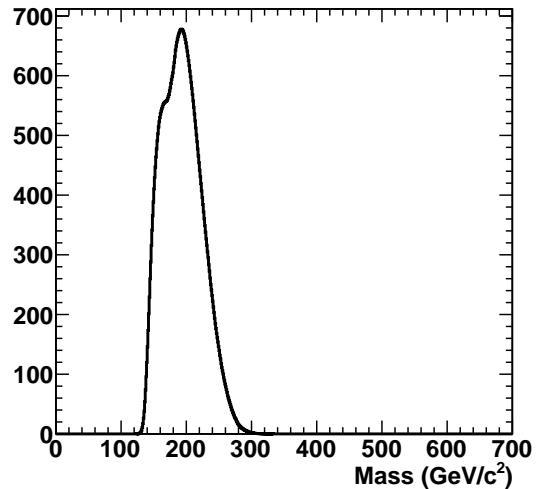
Run: 142305
 Lumi Section: 22
 Event: 15915819
 Peak Mass: 185 GeV/c²
 Peak Weight: 155.30
 b-tagged Jets: 1

	p _T	η	φ	E
μ ⁺	60.39	-0.67	-2.50	74.24
e ⁻	81.47	0.46	-2.91	90.43
Jet 1	81.53	0.51	-0.73	92.76
Jet 2	76.74	0.24	0.98	79.76
E _T	43.52		0.71	



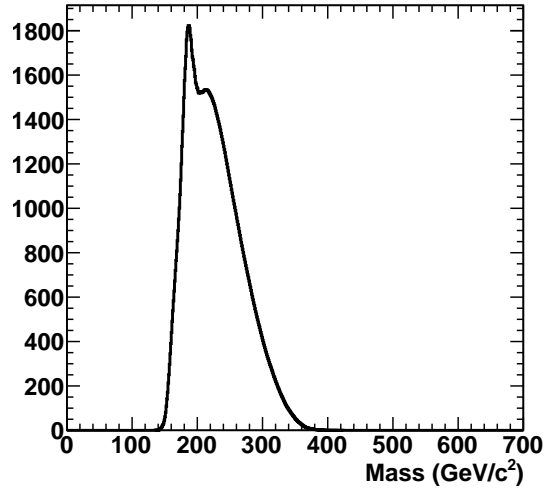
Run: 142971
 Lumi Section: 235
 Event: 222175234
 Peak Mass: 192 GeV/c²
 Peak Weight: 678.00
 b-tagged Jets: 2

	p _T	η	φ	E
e ⁺	46.40	-2.23	2.49	218.63
μ ⁻	50.73	-1.49	-2.28	118.50
Jet 1	51.61	-0.52	1.68	59.71
Jet 2	45.54	0.03	-0.64	45.76
E _T	35.28		-0.75	



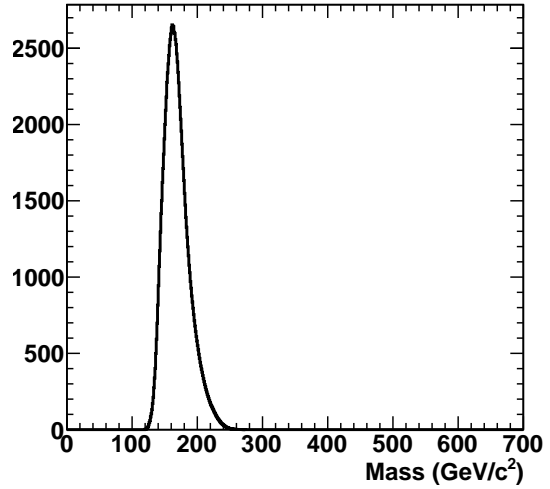
Run: 143657
 Lumi Section: 633
 Event: 584500498
 Peak Mass: 186 GeV/c²
 Peak Weight: 1822.87
 b-tagged Jets: 2

	p _T	η	φ	E
e ⁺	45.97	-0.52	-1.97	52.28
μ ⁻	44.21	-0.32	2.85	46.56
Jet 1	123.80	-0.56	-0.54	143.90
Jet 2	98.84	-0.33	1.63	104.71
E _T	34.78		-2.47	



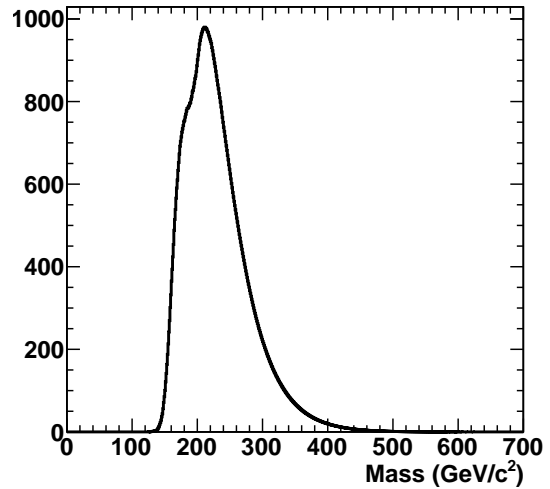
Run: 143953
 Lumi Section: 330
 Event: 319301054
 Peak Mass: 161 GeV/c²
 Peak Weight: 2653.36
 b-tagged Jets: 1

	p _T	η	φ	E
μ ⁺	29.84	0.67	-2.05	36.85
μ ⁻	21.96	1.01	-2.90	34.12
Jet 1	49.77	0.34	0.34	53.79
Jet 2	40.32	1.25	1.12	76.65
E _T	56.57		-2.49	



Run: 143962
 Lumi Section: 227
 Event: 244363110
 Peak Mass: 211 GeV/c²
 Peak Weight: 980.20
 b-tagged Jets: 2

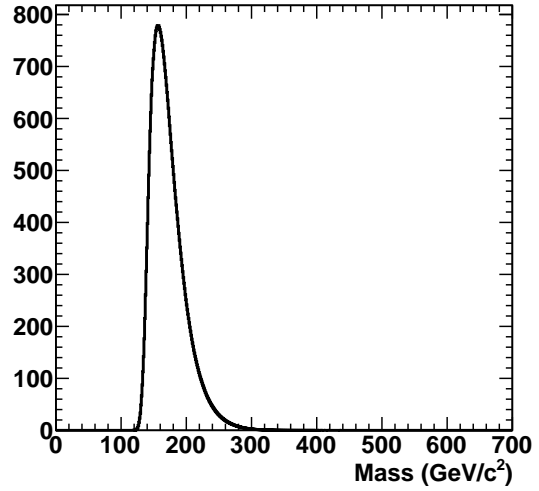
	p _T	η	φ	E
μ ⁺	87.17	0.18	-1.84	88.51
e ⁻	44.69	-0.82	0.58	60.71
Jet 1	88.52	-0.65	2.30	108.78
Jet 2	56.64	1.12	-0.05	96.97
E _T	22.55		-2.55	



Run: 144089
 Lumi Section: 1088
 Event: 1190110762

Peak Mass: 157 GeV/c²
 Peak Weight: 778.65
 b-tagged Jets: 1

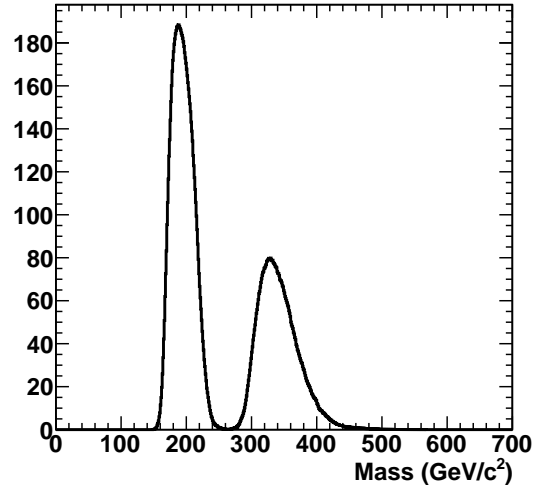
	p _T	η	φ	E
e ⁺	43.29	-0.22	3.00	44.38
e ⁻	62.34	-1.65	-0.11	167.94
Jet 1	37.94	-1.17	-2.64	67.27
Jet 2	44.00	-2.17	2.49	194.75
E _T	46.81		-2.36	



Run: 146511
 Lumi Section: 504
 Event: 365211311

Peak Mass: 188 GeV/c²
 Peak Weight: 188.39
 b-tagged Jets: 1

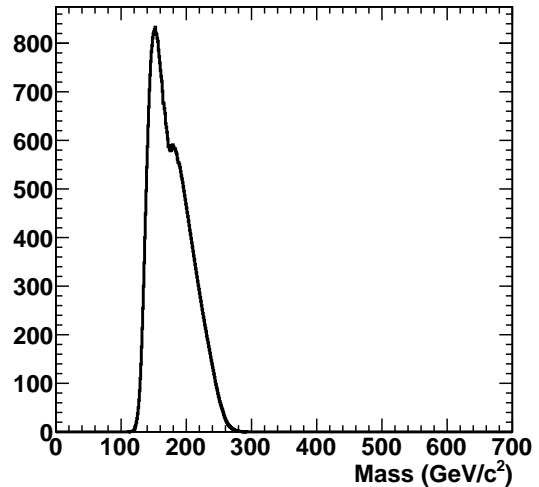
	p _T	η	φ	E
e ⁺	47.12	1.81	-2.19	148.17
e ⁻	132.46	-0.01	2.30	132.47
Jet 1	87.71	-0.71	1.28	111.72
Jet 2	114.30	0.84	-0.57	157.60
E _T	69.45		-1.50	



Run: 146644
 Lumi Section: 1633
 Event: 1255480064

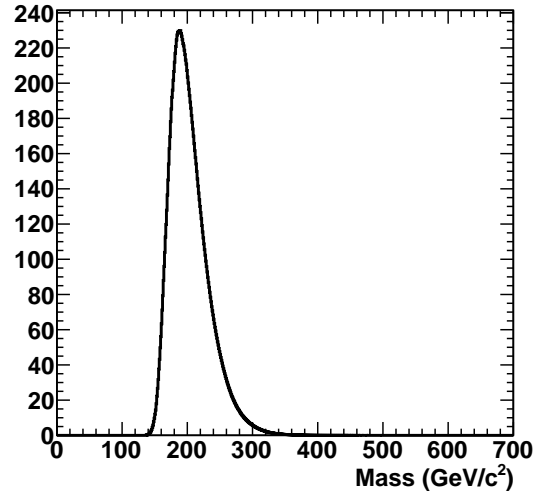
Peak Mass: 152 GeV/c²
 Peak Weight: 833.06
 b-tagged Jets: 1

	p _T	η	φ	E
μ ⁺	84.68	0.39	-0.58	91.13
e ⁻	24.09	0.89	-2.35	34.19
Jet 1	48.35	1.36	2.25	101.26
Jet 2	32.94	-0.70	-2.43	41.46
E _T	67.93		2.12	



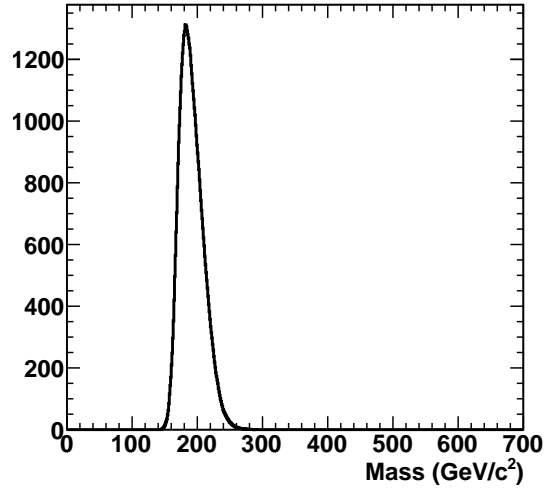
Run: 146644
 Lumi Section: 345
 Event: 307415775
 Peak Mass: 189 GeV/c²
 Peak Weight: 229.87
 b-tagged Jets: 2

	p _T	η	φ	E
μ ⁺	121.93	-1.33	1.90	247.27
μ ⁻	86.63	0.79	-1.22	115.18
Jet 1	65.35	0.15	0.05	66.42
Jet 2	36.45	0.36	2.57	39.67
E _T	71.54		-0.90	



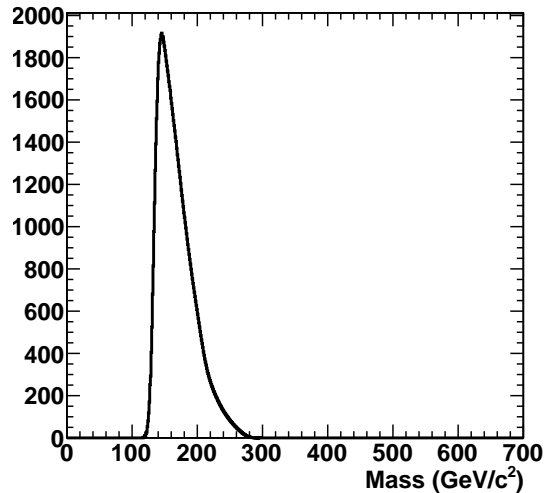
Run: 146804
 Lumi Section: 269
 Event: 212585078
 Peak Mass: 182 GeV/c²
 Peak Weight: 1311.88
 b-tagged Jets: 2

	p _T	η	φ	E
μ ⁺	44.47	0.48	-0.23	49.66
μ ⁻	72.00	-0.59	-2.06	85.08
Jet 1	112.77	0.40	1.71	122.77
Jet 2	62.72	-0.64	-0.21	76.62
E _T	60.04		-3.07	



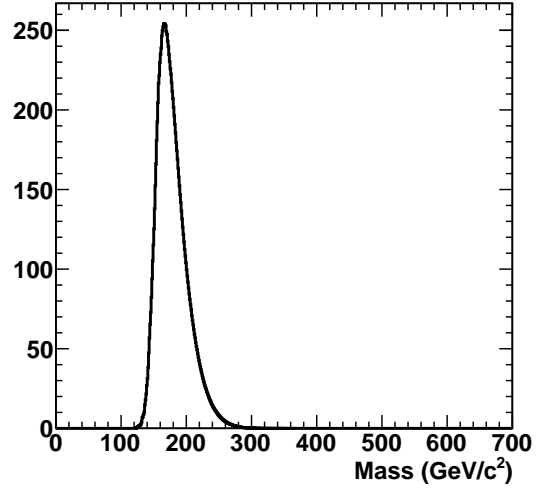
Run: 146804
 Lumi Section: 764
 Event: 739921506
 Peak Mass: 145 GeV/c²
 Peak Weight: 1916.01
 b-tagged Jets: 2

	p _T	η	φ	E
e ⁺	35.54	0.73	-2.96	45.34
e ⁻	20.40	-0.01	-1.48	20.40
Jet 1	70.96	0.49	-2.35	80.08
Jet 2	53.65	0.92	-0.04	78.57
E _T	73.54		1.50	



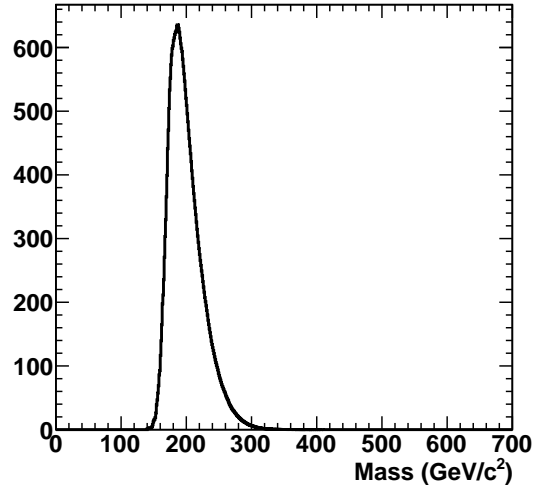
Run: 146807
 Lumi Section: 178
 Event: 183012929
 Peak Mass: 165 GeV/c²
 Peak Weight: 254.22
 b-tagged Jets: 1

	p _T	η	φ	E
μ ⁺	45.76	0.24	-0.66	47.09
e ⁻	140.48	-0.07	3.04	140.85
Jet 1	34.68	1.03	2.76	55.65
Jet 2	137.06	0.25	0.51	142.78
E _T	54.94		-1.18	



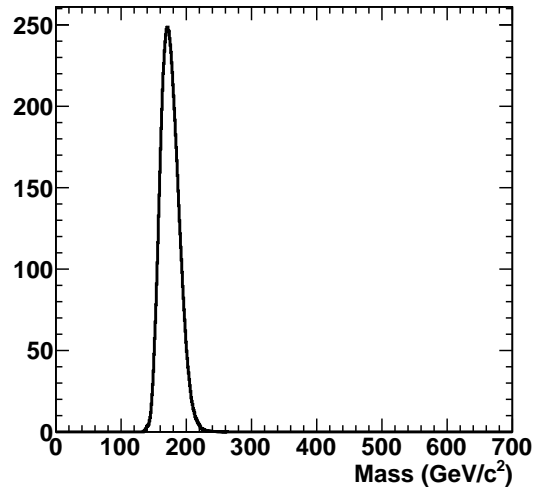
Run: 146807
 Lumi Section: 398
 Event: 399257984
 Peak Mass: 186 GeV/c²
 Peak Weight: 635.54
 b-tagged Jets: 0

	p _T	η	φ	E
μ ⁺	22.83	-0.82	-1.48	30.86
e ⁻	48.19	1.11	1.13	80.87
Jet 1	76.95	1.17	2.60	136.35
Jet 2	53.11	0.91	1.89	77.93
E _T	108.45		-1.17	



Run: 147048
 Lumi Section: 161
 Event: 134625993
 Peak Mass: 171 GeV/c²
 Peak Weight: 248.62
 b-tagged Jets: 2

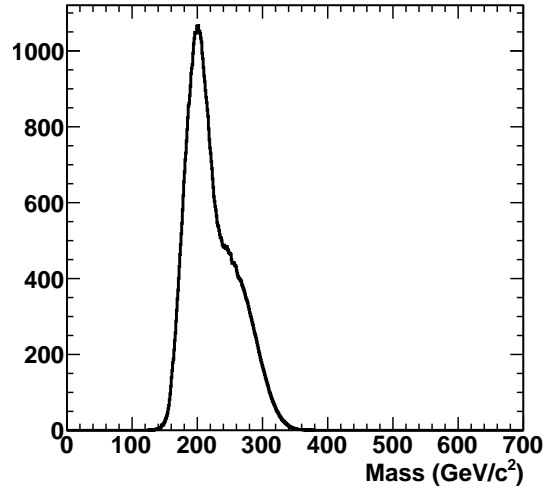
	p _T	η	φ	E
μ ⁺	104.29	0.18	1.17	105.96
e ⁻	45.35	-0.17	-2.95	46.02
Jet 1	166.97	0.49	-1.59	188.15
Jet 2	36.20	-0.42	0.12	39.96
E _T	108.10		1.92	



Run: 147114
 Lumi Section: 340
 Event: 276016381

Peak Mass: 200 GeV/c²
 Peak Weight: 1066.68
 b-tagged Jets: 2

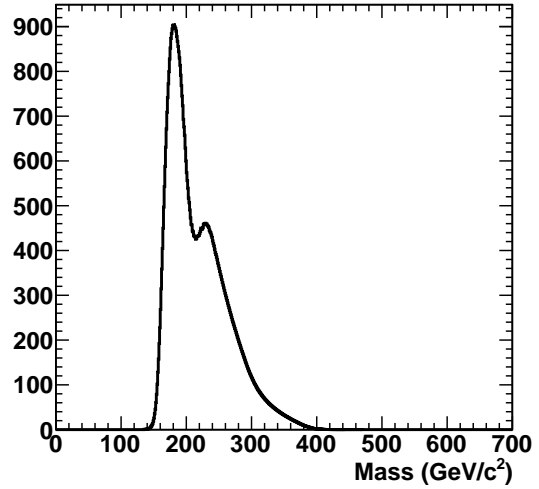
	p _T	η	φ	E
μ ⁺	42.04	-0.36	-2.49	44.83
e ⁻	36.15	0.73	-2.69	46.15
Jet 1	102.30	0.57	0.53	119.53
Jet 2	44.08	-1.27	-0.15	84.82
E _T	65.51		-2.88	



Run: 147115
 Lumi Section: 2
 Event: 878744

Peak Mass: 180 GeV/c²
 Peak Weight: 903.85
 b-tagged Jets: 1

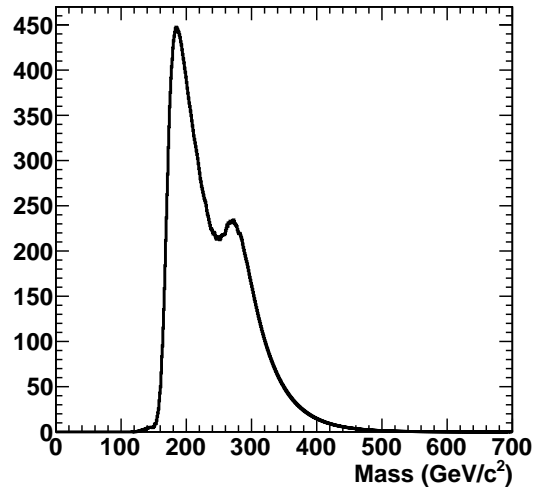
	p _T	η	φ	E
μ ⁺	30.33	-1.36	-2.09	62.90
e ⁻	23.26	0.78	-1.48	30.63
Jet 1	75.32	-0.54	2.74	88.85
Jet 2	144.09	-0.58	0.63	169.50
E _T	55.81		-1.91	



Run: 147115
 Lumi Section: 43
 Event: 53131618

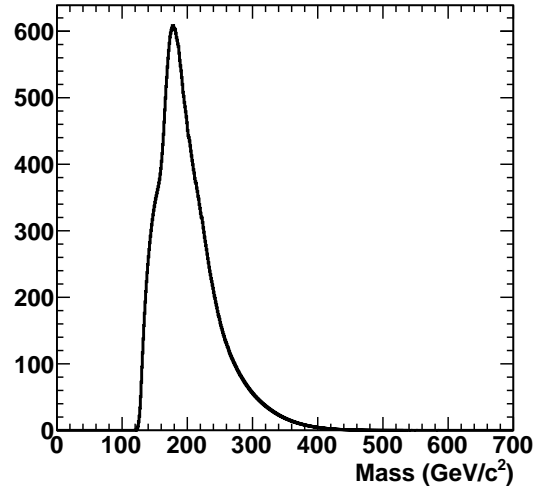
Peak Mass: 184 GeV/c²
 Peak Weight: 447.49
 b-tagged Jets: 0

	p _T	η	φ	E
e ⁺	61.79	-0.77	-2.77	81.25
e ⁻	21.89	0.04	1.08	21.91
Jet 1	50.55	1.02	-0.49	79.42
Jet 2	30.43	-2.41	0.82	171.00
E _T	35.25		-0.14	



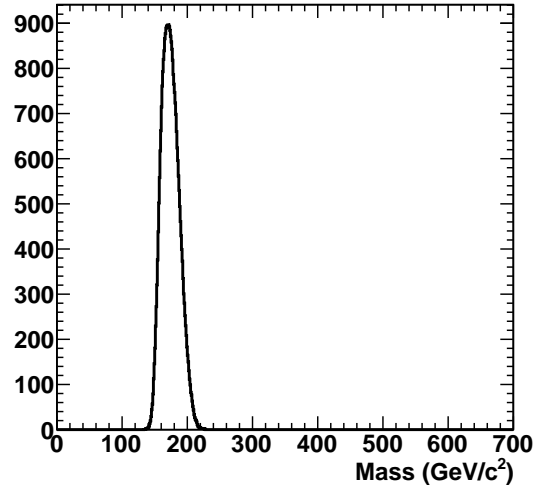
Run: 147216
 Lumi Section: 46
 Event: 34569448
 Peak Mass: 177 GeV/c²
 Peak Weight: 608.45
 b-tagged Jets: 2

	p _T	η	φ	E
e ⁺	37.49	-2.15	0.93	163.20
μ ⁻	20.13	0.23	2.08	20.65
Jet 1	112.65	-1.20	3.14	204.46
Jet 2	58.31	-2.02	-0.28	224.50
E _T	86.49		1.35	



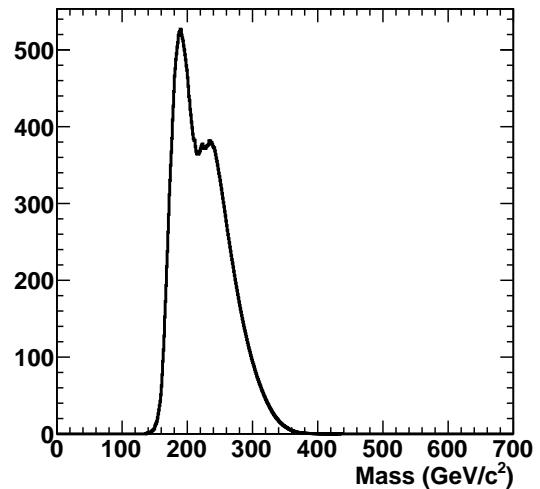
Run: 147217
 Lumi Section: 75
 Event: 55188718
 Peak Mass: 170 GeV/c²
 Peak Weight: 896.38
 b-tagged Jets: 0

	p _T	η	φ	E
μ ⁺	46.71	-0.62	-2.59	55.89
e ⁻	47.47	-1.46	-1.87	107.57
Jet 1	44.17	0.88	1.16	63.08
Jet 2	31.62	0.29	2.10	33.60
E _T	80.38		-0.08	



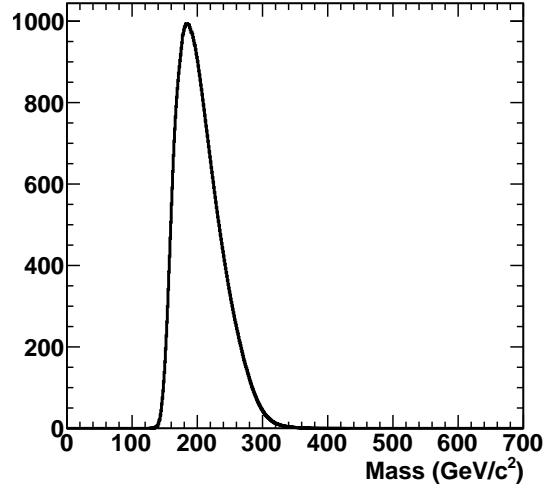
Run: 147217
 Lumi Section: 8
 Event: 5192291
 Peak Mass: 189 GeV/c²
 Peak Weight: 527.00
 b-tagged Jets: 2

	p _T	η	φ	E
μ ⁺	70.69	1.63	-1.59	187.27
e ⁻	49.08	0.29	0.38	51.15
Jet 1	104.41	0.38	2.85	116.03
Jet 2	45.89	1.77	2.33	139.79
E _T	40.57		-0.33	



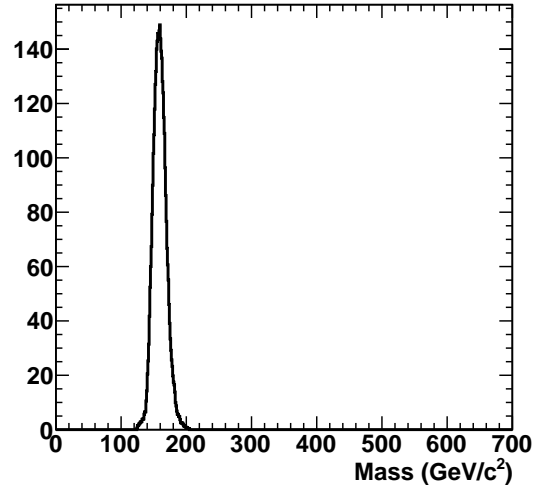
Run: 147219
 Lumi Section: 102
 Event: 69038984
 Peak Mass: 183 GeV/c²
 Peak Weight: 994.02
 b-tagged Jets: 2

	p _T	η	φ	E
μ ⁺	31.66	0.35	-2.49	33.62
μ ⁻	31.69	-1.24	1.91	59.48
Jet 1	104.79	-0.53	-1.70	120.25
Jet 2	63.36	1.05	1.63	102.24
E _T	71.88		0.39	



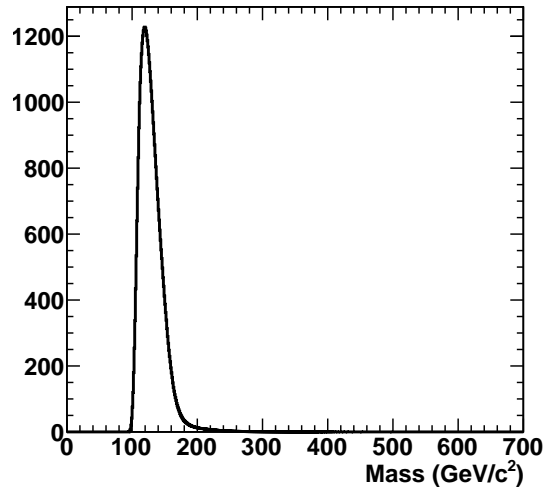
Run: 147219
 Lumi Section: 102
 Event: 69124299
 Peak Mass: 159 GeV/c²
 Peak Weight: 148.93
 b-tagged Jets: 1

	p _T	η	φ	E
μ ⁺	88.09	1.11	-2.88	148.28
e ⁻	58.38	0.40	-1.00	63.00
Jet 1	39.37	0.13	2.27	41.24
Jet 2	41.70	0.82	1.77	56.95
E _T	99.87		-0.00	



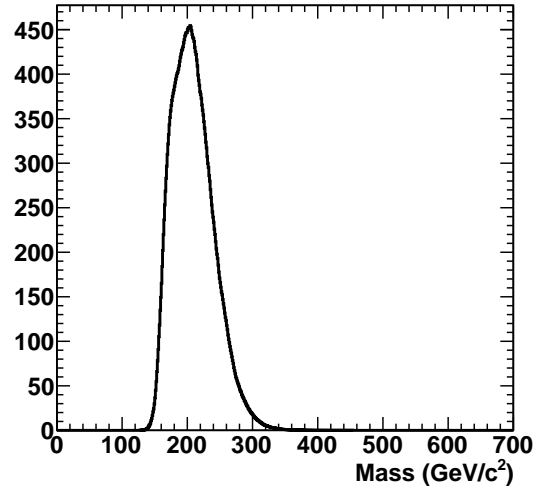
Run: 147219
 Lumi Section: 26
 Event: 17549801
 Peak Mass: 119 GeV/c²
 Peak Weight: 1227.69
 b-tagged Jets: 1

	p _T	η	φ	E
e ⁺	80.37	-0.30	2.67	83.96
e ⁻	59.86	-0.79	-0.42	79.38
Jet 1	33.95	-1.92	-0.83	118.74
Jet 2	35.31	-0.68	1.78	44.37
E _T	41.53		2.16	



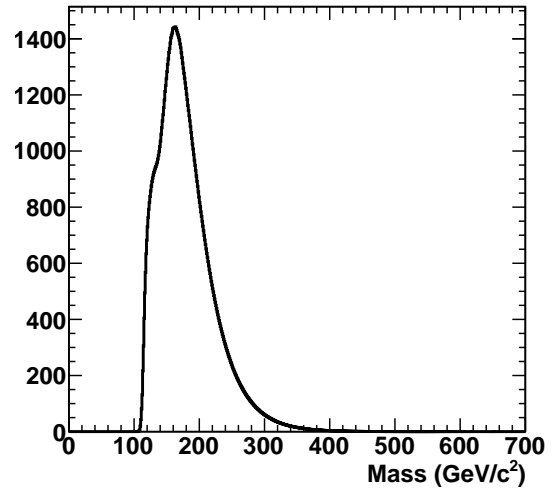
Run: 147390
 Lumi Section: 701
 Event: 564227635
 Peak Mass: 204 GeV/c²
 Peak Weight: 454.53
 b-tagged Jets: 1

	p _T	η	φ	E
e ⁺	133.59	-0.06	-0.40	133.86
μ ⁻	65.49	0.41	-2.91	70.99
Jet 1	48.28	-0.65	1.99	60.38
Jet 2	41.94	-1.57	0.23	105.29
E _T	40.04		2.18	



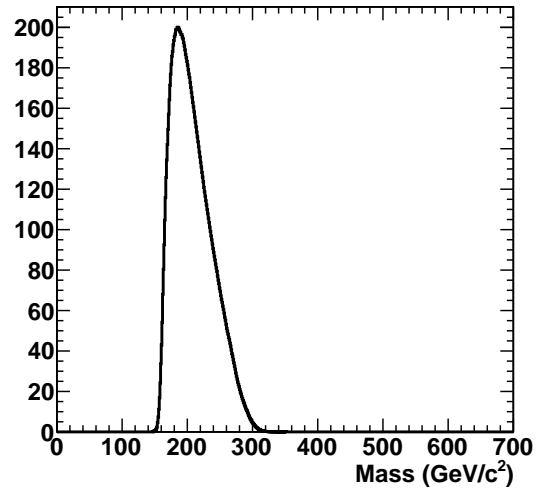
Run: 147451
 Lumi Section: 120
 Event: 139902700
 Peak Mass: 163 GeV/c²
 Peak Weight: 1442.49
 b-tagged Jets: 2

	p _T	η	φ	E
μ ⁺	40.18	1.27	-0.60	77.46
e ⁻	31.29	-0.24	-3.04	32.20
Jet 1	78.53	0.49	-2.76	88.94
Jet 2	69.45	0.27	-0.08	72.69
E _T	49.31		1.14	



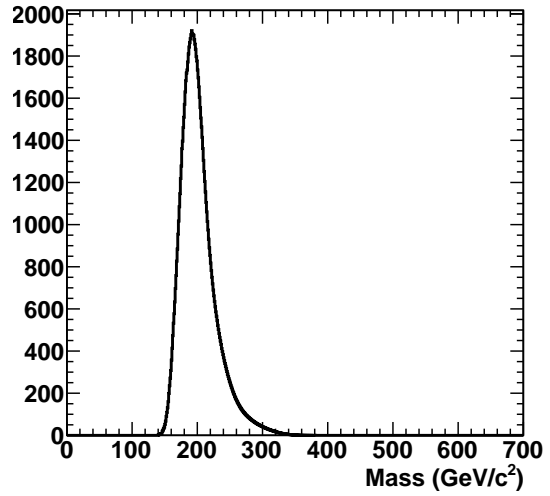
Run: 147754
 Lumi Section: 47
 Event: 58840276
 Peak Mass: 185 GeV/c²
 Peak Weight: 200.12
 b-tagged Jets: 1

	p _T	η	φ	E
μ ⁺	24.13	1.98	-2.67	88.64
μ ⁻	42.81	-1.10	2.44	71.63
Jet 1	81.46	0.55	2.49	95.03
Jet 2	81.11	-2.16	-0.20	356.82
E _T	67.77		-0.59	



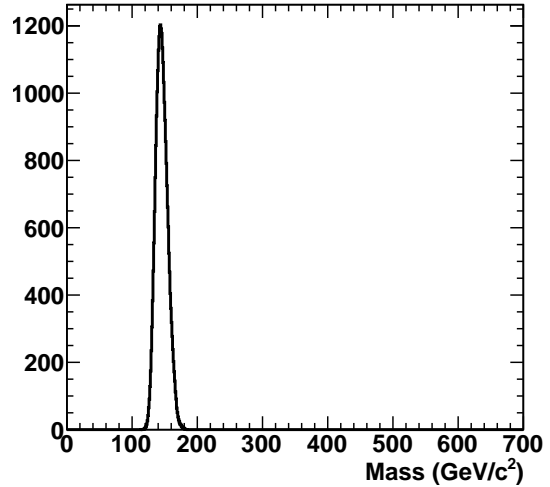
Run: 147926
 Lumi Section: 137
 Event: 102435902
 Peak Mass: 191 GeV/c²
 Peak Weight: 1920.73
 b-tagged Jets: 2

	p _T	η	φ	E
μ ⁺	31.94	-0.01	0.10	31.94
μ ⁻	22.22	-0.52	-1.49	25.25
Jet 1	65.63	-0.37	1.68	70.91
Jet 2	60.79	-1.08	1.92	100.48
E _T	81.10		-1.73	



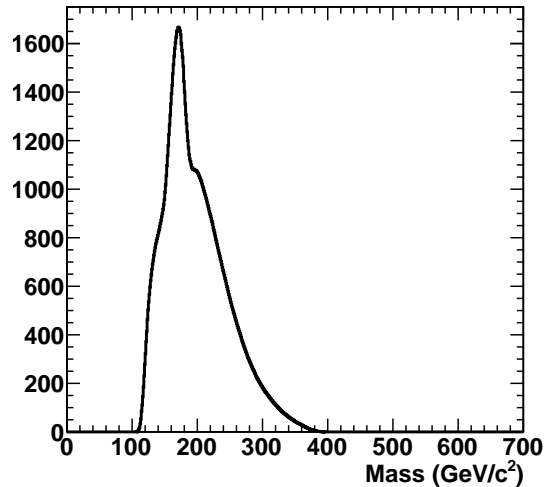
Run: 147926
 Lumi Section: 190
 Event: 174596074
 Peak Mass: 143 GeV/c²
 Peak Weight: 1202.97
 b-tagged Jets: 2

	p _T	η	φ	E
μ ⁺	125.87	0.19	-2.40	128.12
e ⁻	81.74	0.35	-3.03	86.87
Jet 1	53.18	0.50	-1.70	60.52
Jet 2	36.87	-0.29	-1.07	39.22
E _T	121.77		-2.50	



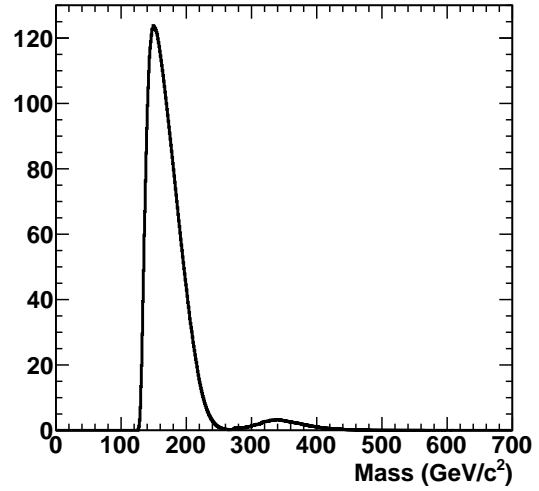
Run: 147926
 Lumi Section: 357
 Event: 380430462
 Peak Mass: 171 GeV/c²
 Peak Weight: 1667.63
 b-tagged Jets: 2

	p _T	η	φ	E
e ⁺	28.53	0.27	-1.73	29.58
μ ⁻	34.27	-0.01	-0.26	34.27
Jet 1	123.26	0.53	-2.32	142.17
Jet 2	117.38	0.00	0.74	117.79
E _T	62.30		2.26	



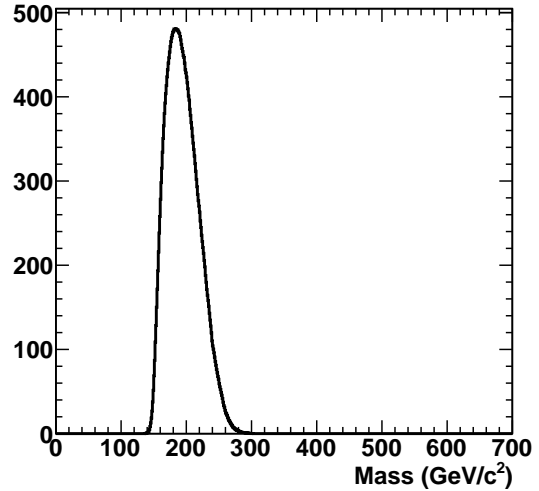
Run: 147926
 Lumi Section: 493
 Event: 531114775
 Peak Mass: 149 GeV/c²
 Peak Weight: 123.81
 b-tagged Jets: 2

	p _T	η	φ	E
e ⁺	56.17	-0.89	0.79	79.64
μ ⁻	65.52	-2.29	-1.82	327.14
Jet 1	154.86	-0.66	1.57	191.30
Jet 2	133.98	-1.66	-1.33	364.98
E _T	57.76		-2.65	



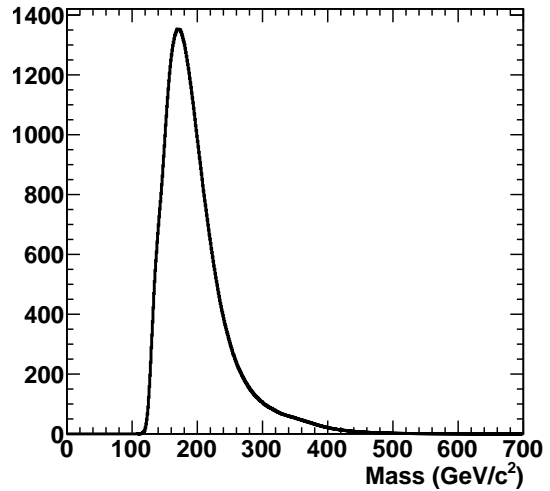
Run: 147927
 Lumi Section: 4
 Event: 2196303
 Peak Mass: 184 GeV/c²
 Peak Weight: 480.70
 b-tagged Jets: 1

	p _T	η	φ	E
e ⁺	62.82	-0.33	-2.49	66.25
μ ⁻	31.92	0.37	2.07	34.17
Jet 1	87.67	0.06	-0.78	88.65
Jet 2	172.58	-0.95	2.03	257.34
E _T	66.83		-1.35	



Run: 148029
 Lumi Section: 251
 Event: 189180291
 Peak Mass: 170 GeV/c²
 Peak Weight: 1352.89
 b-tagged Jets: 1

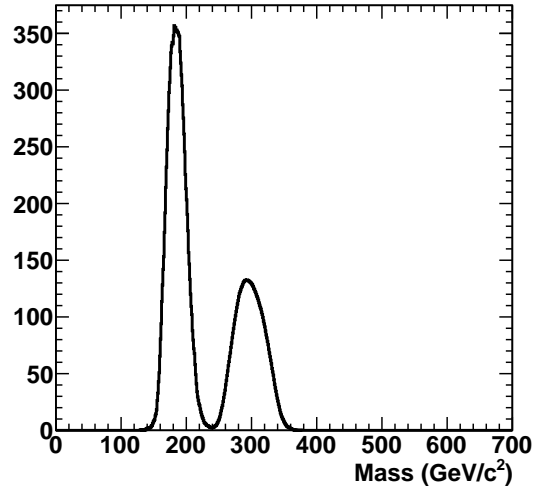
	p _T	η	φ	E
e ⁺	25.59	0.99	-1.10	39.28
e ⁻	31.00	-0.05	1.51	31.04
Jet 1	73.62	-0.96	0.14	110.72
Jet 2	89.28	1.07	-2.71	146.10
E _T	59.02		0.07	



Run: 148029
 Lumi Section: 457
 Event: 357580841

Peak Mass: 181 GeV/c²
 Peak Weight: 356.88
 b-tagged Jets: 2

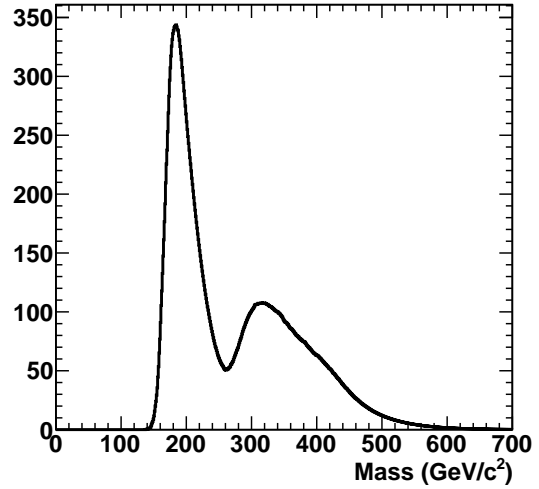
	p _T	η	φ	E
μ ⁺	26.75	1.35	2.13	55.07
e ⁻	51.54	-1.11	-2.87	86.70
Jet 1	91.37	1.29	-0.28	179.80
Jet 2	86.24	-0.24	1.61	89.25
E _T	83.84		-1.57	



Run: 148029
 Lumi Section: 512
 Event: 398160572

Peak Mass: 184 GeV/c²
 Peak Weight: 343.73
 b-tagged Jets: 2

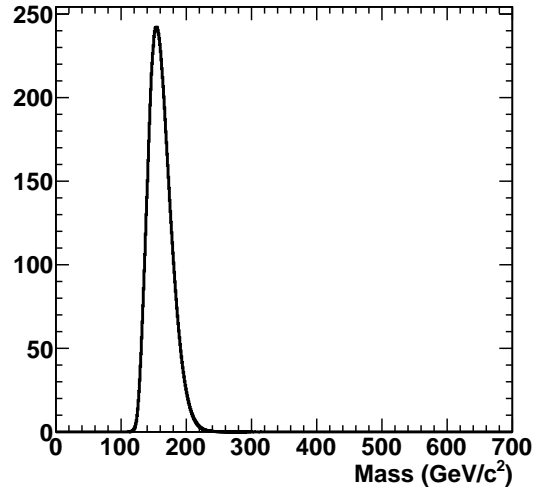
	p _T	η	φ	E
μ ⁺	76.31	-1.27	-1.04	146.92
μ ⁻	40.98	1.15	1.60	71.42
Jet 1	113.43	-0.11	-0.75	115.00
Jet 2	64.36	1.36	-2.84	133.70
E _T	79.35		1.77	



Run: 148031
 Lumi Section: 272
 Event: 230563364

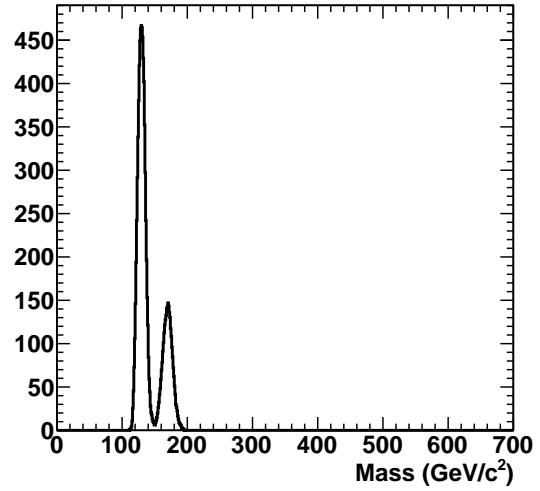
Peak Mass: 154 GeV/c²
 Peak Weight: 242.16
 b-tagged Jets: 2

	p _T	η	φ	E
e ⁺	58.18	-2.31	-1.77	295.26
e ⁻	28.51	-1.88	2.27	95.66
Jet 1	68.91	-2.34	2.67	359.80
Jet 2	54.25	-1.59	-0.11	139.13
E _T	49.70		-0.59	



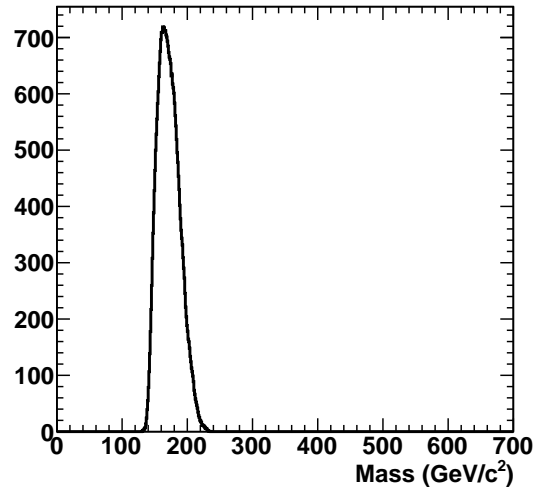
Run: 148031
 Lumi Section: 323
 Event: 271917202
 Peak Mass: 129 GeV/c²
 Peak Weight: 466.83
 b-tagged Jets: 1

	p _T	η	φ	E
e ⁺	25.64	-1.19	-2.16	46.01
e ⁻	60.57	-1.02	-1.87	94.60
Jet 1	42.49	-0.18	-1.77	43.86
Jet 2	60.91	-2.08	1.37	247.36
E _T	74.21		1.43	



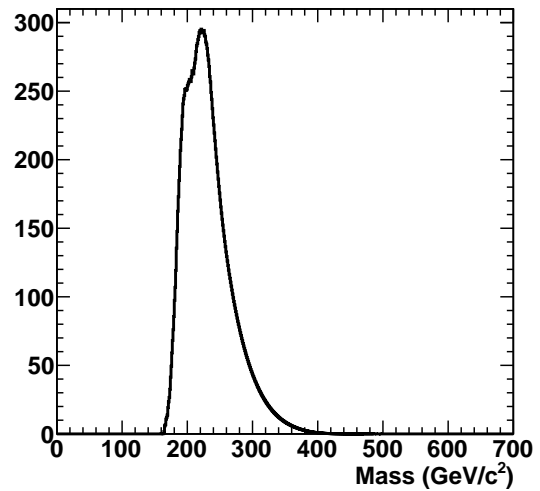
Run: 148031
 Lumi Section: 604
 Event: 479681918
 Peak Mass: 162 GeV/c²
 Peak Weight: 718.92
 b-tagged Jets: 0

	p _T	η	φ	E
e ⁺	70.36	-0.21	-0.53	71.88
e ⁻	28.58	-0.92	-0.49	41.68
Jet 1	74.67	0.10	2.07	76.00
Jet 2	30.73	1.17	1.94	54.76
E _T	70.29		-3.12	



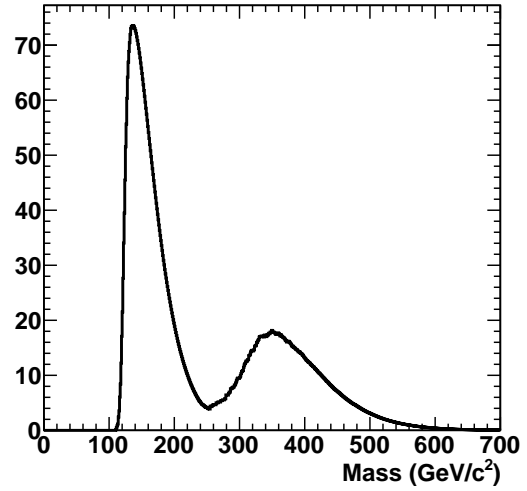
Run: 148829
 Lumi Section: 155
 Event: 153397876
 Peak Mass: 221 GeV/c²
 Peak Weight: 295.22
 b-tagged Jets: 0

	p _T	η	φ	E
e ⁺	27.20	-1.81	2.88	85.14
μ ⁻	36.73	-1.16	-1.92	64.24
Jet 1	115.01	-0.07	0.94	116.76
Jet 2	33.90	0.15	-1.57	34.74
E _T	45.05		-2.63	



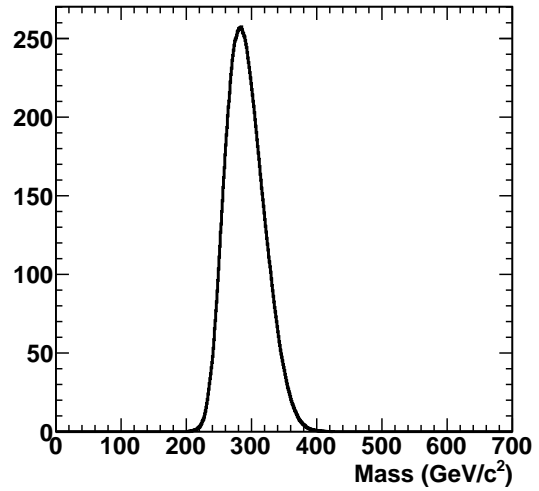
Run: 148829
 Lumi Section: 226
 Event: 222070925
 Peak Mass: 136 GeV/c²
 Peak Weight: 73.55
 b-tagged Jets: 2

	p _T	η	φ	E
μ ⁺	90.02	1.19	-2.29	161.05
μ ⁻	30.46	0.25	1.20	31.40
Jet 1	160.33	1.74	-2.15	470.73
Jet 2	58.10	-0.94	1.66	86.08
E _T	143.27		0.84	



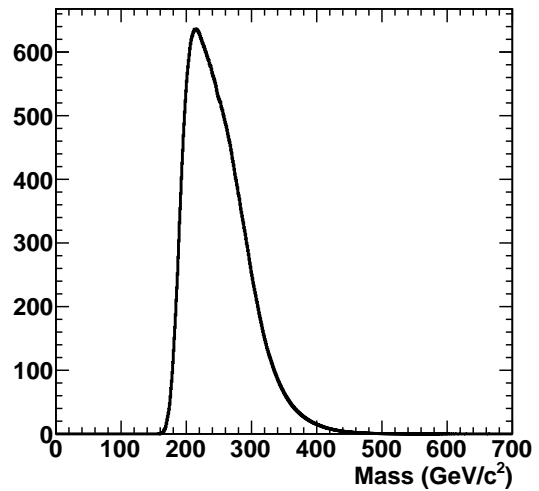
Run: 148829
 Lumi Section: 271
 Event: 265238495
 Peak Mass: 284 GeV/c²
 Peak Weight: 257.41
 b-tagged Jets: 0

	p _T	η	φ	E
e ⁺	29.94	-1.25	-2.41	56.76
e ⁻	102.39	-1.14	2.42	175.92
Jet 1	127.64	-0.62	-0.05	153.23
Jet 2	76.60	0.87	-2.00	108.37
E _T	32.46		0.56	



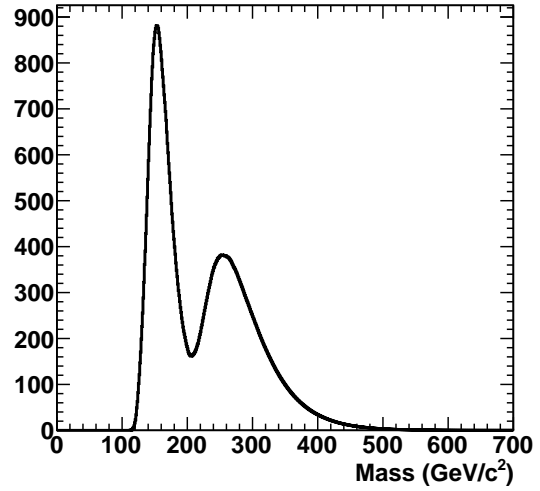
Run: 148829
 Lumi Section: 275
 Event: 269274931
 Peak Mass: 213 GeV/c²
 Peak Weight: 635.98
 b-tagged Jets: 0

	p _T	η	φ	E
μ ⁺	24.89	-1.72	-1.44	71.43
μ ⁻	44.85	-1.90	1.53	152.64
Jet 1	45.10	0.34	-1.90	48.40
Jet 2	41.55	1.40	-1.61	89.51
E _T	49.99		1.43	



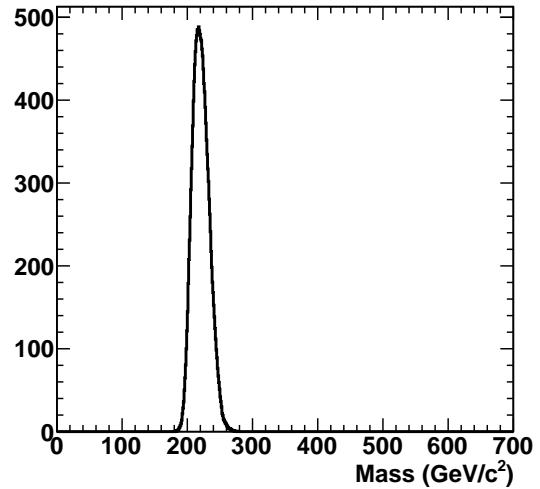
Run: 148829
 Lumi Section: 280
 Event: 273430518
 Peak Mass: 153 GeV/c²
 Peak Weight: 881.31
 b-tagged Jets: 2

	p _T	η	φ	E
μ ⁺	92.26	0.54	-0.87	106.19
e ⁻	55.67	-0.86	2.75	77.71
Jet 1	96.95	-0.37	1.69	103.96
Jet 2	31.51	1.55	-2.20	77.96
E _T	29.79		-0.55	



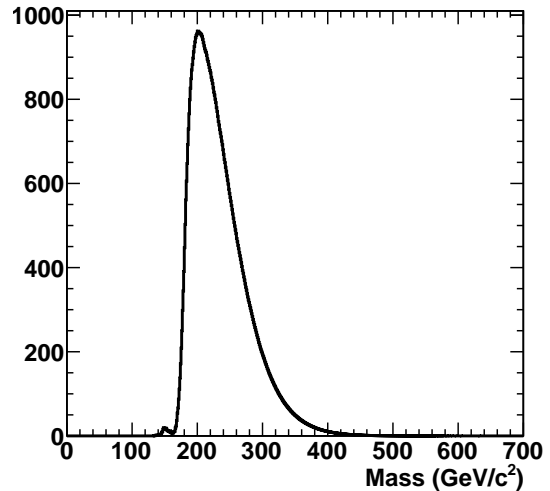
Run: 148829
 Lumi Section: 284
 Event: 277421650
 Peak Mass: 217 GeV/c²
 Peak Weight: 488.43
 b-tagged Jets: 1

	p _T	η	φ	E
e ⁺	38.54	-0.28	2.49	40.01
e ⁻	70.76	-1.17	2.62	125.05
Jet 1	88.92	-0.38	-0.18	97.20
Jet 2	99.72	0.20	-1.63	105.04
E _T	93.91		0.99	



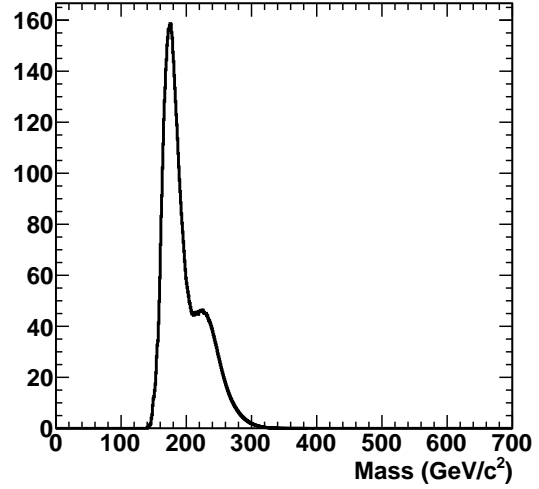
Run: 148862
 Lumi Section: 233
 Event: 351142513
 Peak Mass: 201 GeV/c²
 Peak Weight: 961.98
 b-tagged Jets: 2

	p _T	η	φ	E
μ ⁺	40.33	-1.19	2.40	72.25
μ ⁻	90.18	-0.56	-1.22	104.56
Jet 1	94.13	-0.43	0.23	103.79
Jet 2	65.01	-0.52	1.82	76.70
E _T	39.19		-2.82	



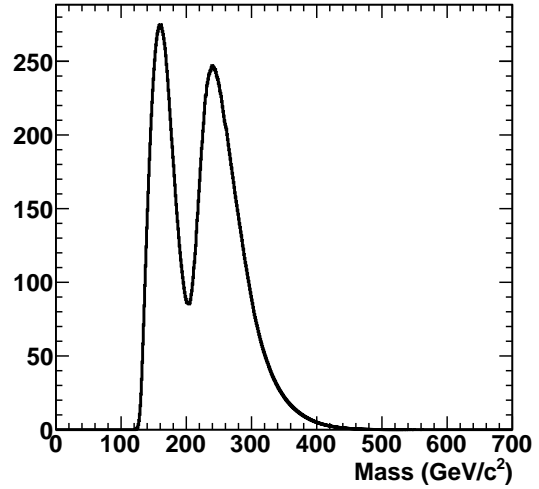
Run: 148862
 Lumi Section: 235
 Event: 353232017
 Peak Mass: 175 GeV/c²
 Peak Weight: 158.66
 b-tagged Jets: 2

	p _T	η	φ	E
μ ⁺	46.51	-0.30	2.54	48.64
μ ⁻	73.93	-1.39	-1.22	157.40
Jet 1	137.84	-1.69	-0.43	387.12
Jet 2	62.78	-1.15	1.19	109.80
E _T	122.22		2.86	



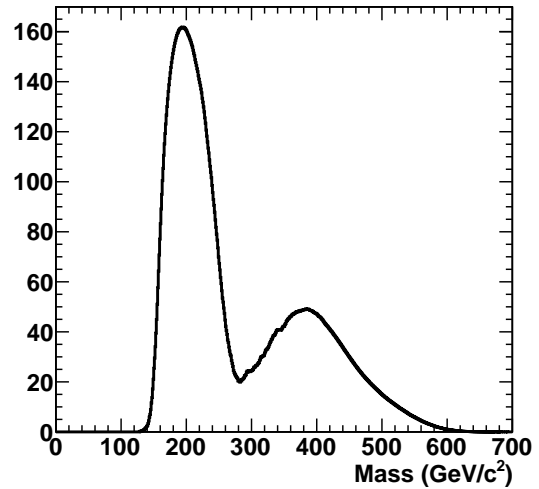
Run: 148862
 Lumi Section: 357
 Event: 532196916
 Peak Mass: 160 GeV/c²
 Peak Weight: 274.73
 b-tagged Jets: 2

	p _T	η	φ	E
e ⁺	52.95	-0.19	2.34	53.95
μ ⁻	23.43	-2.17	-2.13	103.84
Jet 1	119.00	-1.25	-0.64	225.21
Jet 2	112.57	-1.37	2.14	237.76
E _T	87.70		-1.16	



Run: 148862
 Lumi Section: 417
 Event: 616863960
 Peak Mass: 194 GeV/c²
 Peak Weight: 161.81
 b-tagged Jets: 2

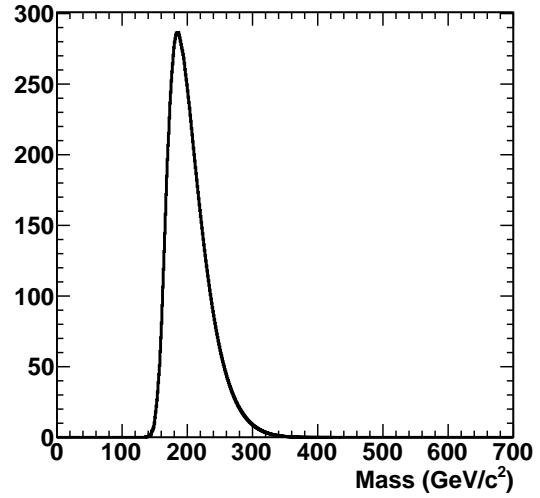
	p _T	η	φ	E
μ ⁺	20.58	1.21	-2.34	37.66
e ⁻	34.34	-0.37	-3.01	36.78
Jet 1	191.47	1.36	0.73	397.66
Jet 2	56.80	-1.44	-2.11	126.59
E _T	91.39		-1.60	



Run: 148862
Lumi Section: 82
Event: 131576801

Peak Mass: 185 GeV/c²
Peak Weight: 286.44
b-tagged Jets: 1

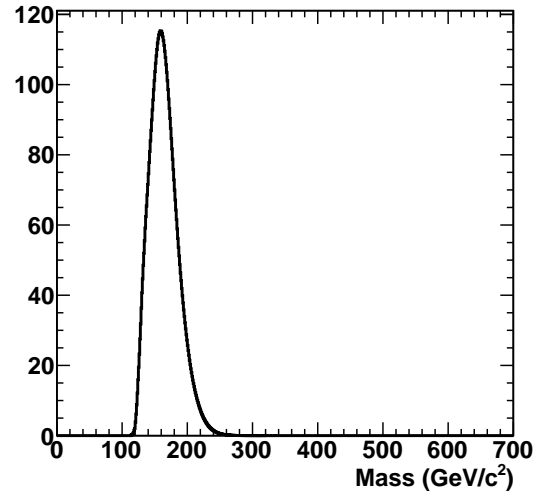
	p _T	η	φ	E
e ⁺	54.19	-1.90	2.80	184.73
μ ⁻	29.66	-2.13	0.40	125.97
Jet 1	42.92	0.01	0.77	44.10
Jet 2	62.59	-2.49	-0.58	378.84
E _T	74.09		-3.11	



Run: 148864
Lumi Section: 225
Event: 267767817

Peak Mass: 159 GeV/c²
Peak Weight: 115.31
b-tagged Jets: 2

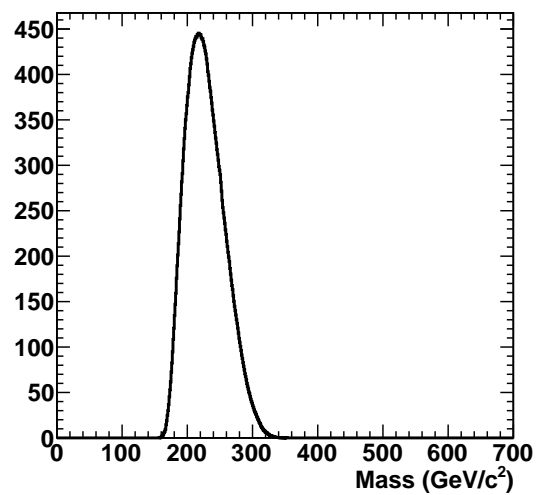
	p _T	η	φ	E
e ⁺	87.72	0.39	2.53	94.41
μ ⁻	135.89	0.05	-0.21	136.03
Jet 1	262.02	-0.16	2.71	266.11
Jet 2	49.27	0.73	-0.72	63.82
E _T	188.54		-0.51	



Run: 148864
Lumi Section: 284
Event: 334989072

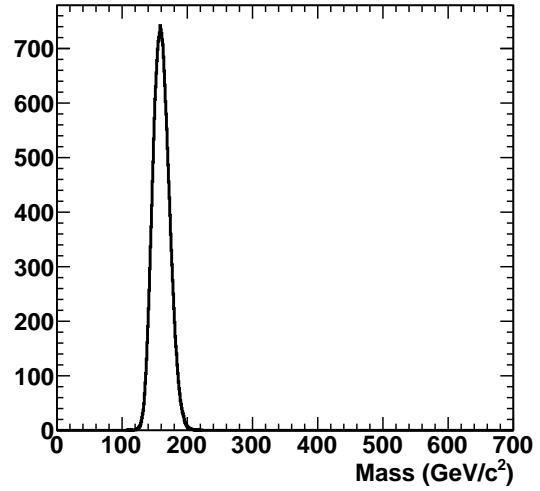
Peak Mass: 217 GeV/c²
Peak Weight: 445.45
b-tagged Jets: 2

	p _T	η	φ	E
e ⁺	31.29	-0.53	-0.10	35.81
μ ⁻	60.03	-0.94	-1.03	88.26
Jet 1	150.85	0.67	-1.15	188.32
Jet 2	84.08	-0.91	2.56	122.36
E _T	153.88		-1.89	



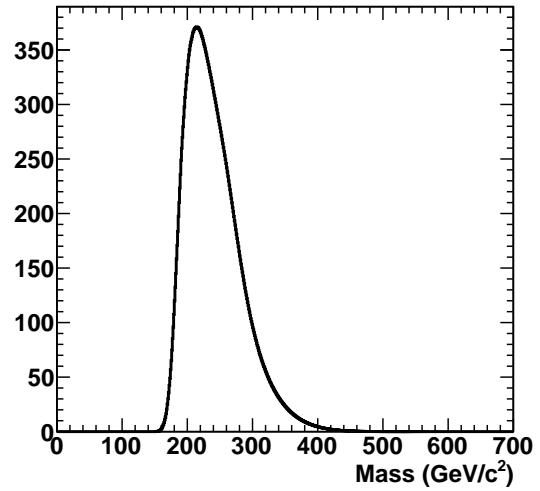
Run: 148864
 Lumi Section: 579
 Event: 654374646
 Peak Mass: 158 GeV/c²
 Peak Weight: 742.01
 b-tagged Jets: 3

	p _T	η	φ	E
μ ⁺	27.37	-1.44	-2.84	61.07
e ⁻	56.48	-2.02	2.76	217.25
Jet 1	52.55	-1.51	-0.75	125.25
Jet 2	41.14	-0.51	-0.77	47.05
E _T	64.68		1.13	



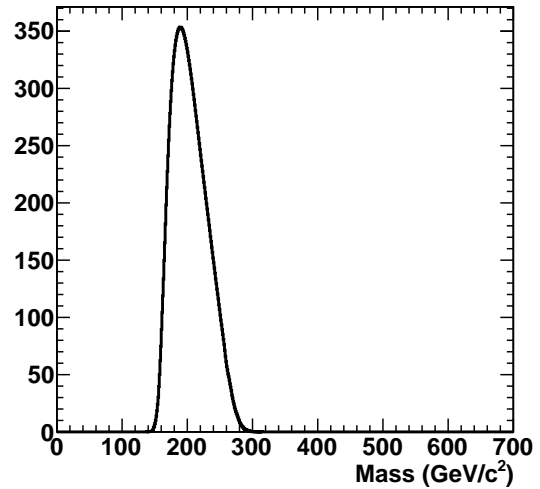
Run: 149003
 Lumi Section: 176
 Event: 170643045
 Peak Mass: 214 GeV/c²
 Peak Weight: 371.15
 b-tagged Jets: 1

	p _T	η	φ	E
μ ⁺	34.09	2.37	-2.98	183.46
e ⁻	30.35	1.31	-1.20	60.58
Jet 1	76.55	0.41	-1.99	84.38
Jet 2	151.20	0.12	1.28	152.81
E _T	23.45		-0.53	



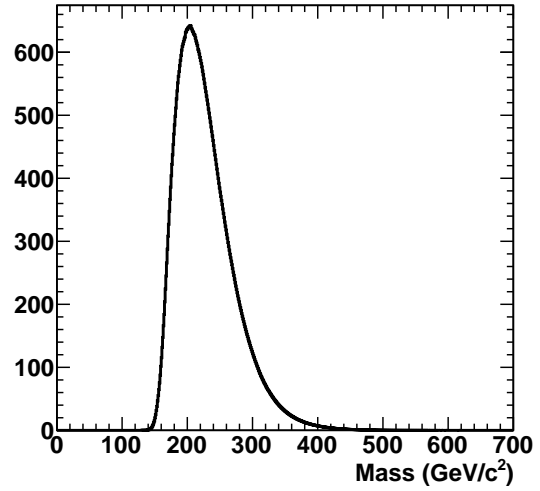
Run: 149003
 Lumi Section: 233
 Event: 251972444
 Peak Mass: 189 GeV/c²
 Peak Weight: 353.51
 b-tagged Jets: 1

	p _T	η	φ	E
μ ⁺	20.51	0.39	1.30	22.11
e ⁻	49.16	1.99	1.58	182.41
Jet 1	72.15	0.79	-0.87	96.74
Jet 2	46.99	-1.68	1.63	130.64
E _T	75.84		-2.30	



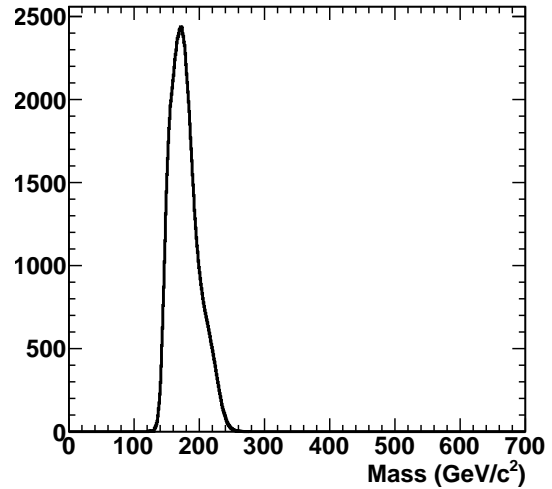
Run: 149011
 Lumi Section: 107
 Event: 167973020
 Peak Mass: 204 GeV/c²
 Peak Weight: 642.29
 b-tagged Jets: 0

	p _T	η	φ	E
e ⁺	27.87	1.47	2.46	64.03
e ⁻	46.41	1.47	-1.65	106.50
Jet 1	105.32	2.00	0.89	396.37
Jet 2	33.51	-1.09	-1.12	56.43
E _T	51.51		-0.88	



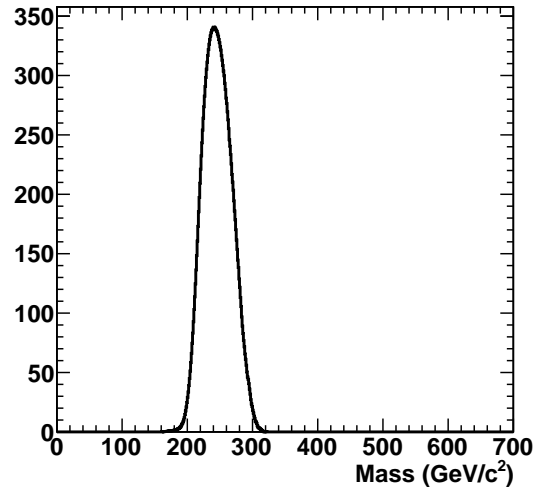
Run: 149011
 Lumi Section: 252
 Event: 386082768
 Peak Mass: 171 GeV/c²
 Peak Weight: 2437.59
 b-tagged Jets: 3

	p _T	η	φ	E
e ⁺	29.65	-0.12	-2.25	29.89
e ⁻	35.89	0.42	-1.98	39.07
Jet 1	52.08	0.51	0.33	60.30
Jet 2	41.57	-1.28	1.19	81.24
E _T	57.84		3.14	



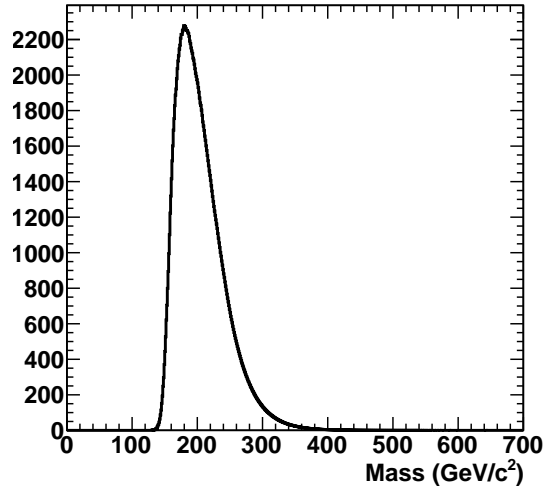
Run: 149011
 Lumi Section: 310
 Event: 468304925
 Peak Mass: 240 GeV/c²
 Peak Weight: 340.70
 b-tagged Jets: 1

	p _T	η	φ	E
μ ⁺	31.58	-0.78	2.15	41.70
μ ⁻	95.54	-1.48	0.89	220.54
Jet 1	57.39	0.93	-2.51	84.32
Jet 2	50.53	0.26	-2.21	52.55
E _T	57.63		-0.27	



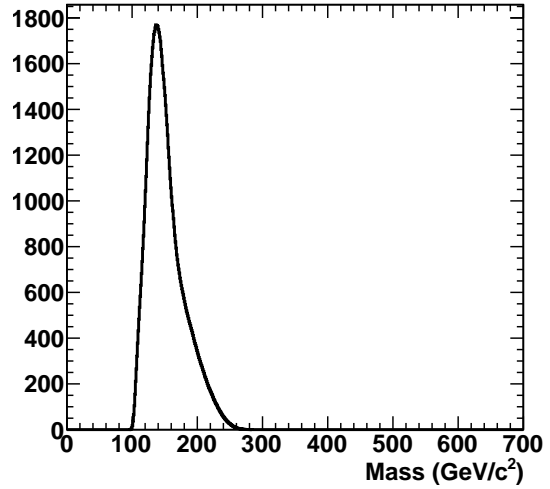
Run: 149011
 Lumi Section: 596
 Event: 839574880
 Peak Mass: 179 GeV/c²
 Peak Weight: 2278.36
 b-tagged Jets: 2

	p _T	η	φ	E
e ⁺	65.82	-0.33	1.86	69.45
μ ⁻	53.11	0.38	-0.91	56.99
Jet 1	67.79	0.28	-2.66	71.96
Jet 2	38.75	-1.56	-1.73	96.89
E _T	44.97		0.81	



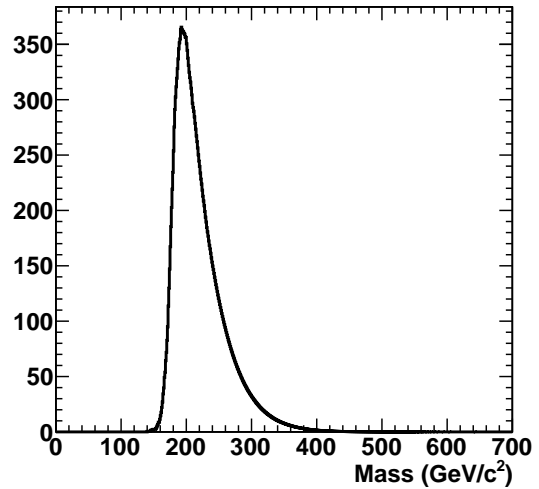
Run: 149011
 Lumi Section: 652
 Event: 907531907
 Peak Mass: 136 GeV/c²
 Peak Weight: 1769.56
 b-tagged Jets: 1

	p _T	η	φ	E
μ ⁺	21.82	-1.96	1.29	78.97
μ ⁻	25.20	-1.32	0.39	50.32
Jet 1	63.74	-0.71	-1.06	80.93
Jet 2	53.67	-1.90	2.93	183.25
E _T	79.94		-1.96	



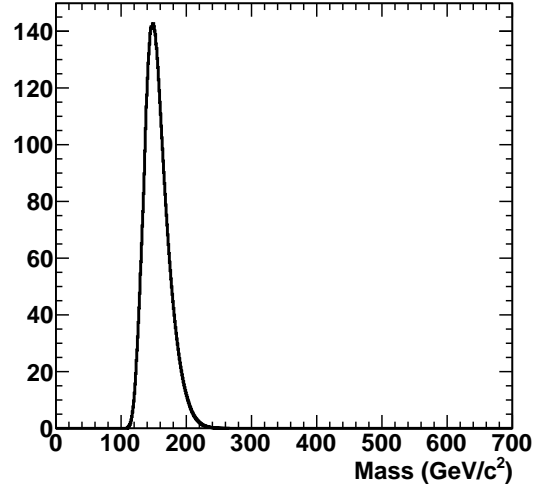
Run: 149011
 Lumi Section: 70
 Event: 109889592
 Peak Mass: 192 GeV/c²
 Peak Weight: 365.52
 b-tagged Jets: 1

	p _T	η	φ	E
μ ⁺	36.51	-0.78	-2.55	48.24
μ ⁻	54.44	0.81	0.89	73.13
Jet 1	52.40	-0.00	-2.11	53.62
Jet 2	86.70	-1.90	-2.33	296.64
E _T	102.23		0.88	



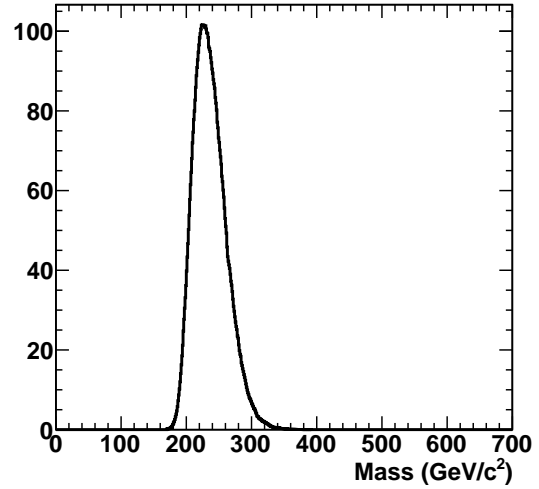
Run: 149063
 Lumi Section: 84
 Event: 98375451
 Peak Mass: 149 GeV/c²
 Peak Weight: 142.69
 b-tagged Jets: 2

	p _T	η	φ	E
μ ⁺	126.55	-0.48	1.30	141.18
e ⁻	89.30	-0.40	-1.38	96.58
Jet 1	212.19	0.09	-1.85	213.47
Jet 2	31.76	0.45	1.73	36.27
E _T	95.95		2.10	



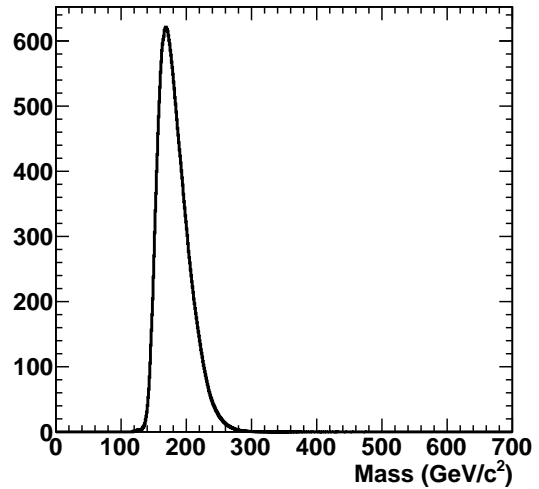
Run: 149181
 Lumi Section: 1194
 Event: 1175707454
 Peak Mass: 225 GeV/c²
 Peak Weight: 101.59
 b-tagged Jets: 0

	p _T	η	φ	E
μ ⁺	39.10	-0.42	-0.48	42.63
e ⁻	69.43	1.96	1.57	251.12
Jet 1	68.71	0.10	-0.30	70.04
Jet 2	66.05	-1.40	-2.42	142.41
E _T	30.33		2.47	



Run: 149181
 Lumi Section: 1340
 Event: 1311956829
 Peak Mass: 168 GeV/c²
 Peak Weight: 621.22
 b-tagged Jets: 2

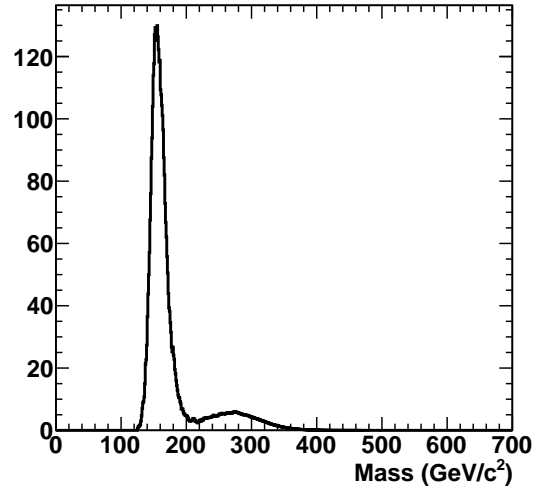
	p _T	η	φ	E
e ⁺	29.96	0.62	-2.60	35.91
μ ⁻	82.10	-0.23	1.05	84.27
Jet 1	71.72	-0.09	-2.56	72.63
Jet 2	50.62	1.07	2.32	82.56
E _T	85.21		-0.55	



Run: 149181
 Lumi Section: 1345
 Event: 1316743403

Peak Mass: 155 GeV/c²
 Peak Weight: 129.94
 b-tagged Jets: 2

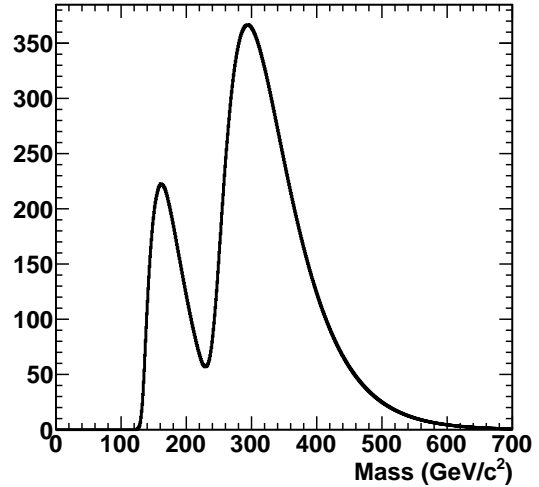
	p _T	η	φ	E
μ ⁺	59.74	1.43	-2.87	132.22
e ⁻	23.20	0.95	0.25	34.57
Jet 1	86.83	-0.04	0.77	88.37
Jet 2	49.50	0.47	0.84	55.21
E _T	33.22		1.88	



Run: 149181
 Lumi Section: 1577
 Event: 1520159957

Peak Mass: 293 GeV/c²
 Peak Weight: 366.60
 b-tagged Jets: 2

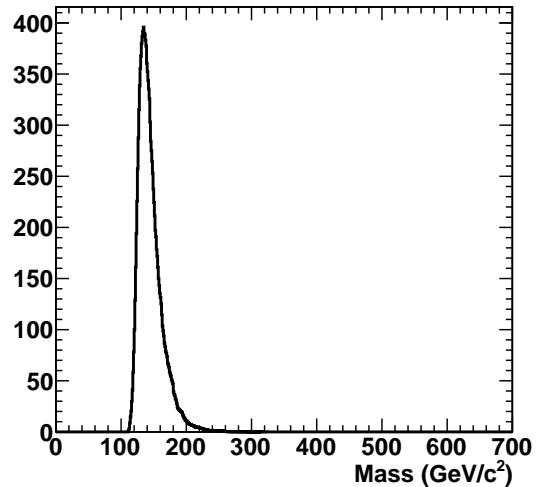
	p _T	η	φ	E
μ ⁺	30.14	1.99	2.85	112.51
μ ⁻	38.20	-1.26	0.59	72.80
Jet 1	138.90	-0.21	-0.37	142.70
Jet 2	113.48	1.03	2.55	180.70
E _T	40.10		-1.83	



Run: 149181
 Lumi Section: 1706
 Event: 1626022411

Peak Mass: 134 GeV/c²
 Peak Weight: 395.88
 b-tagged Jets: 1

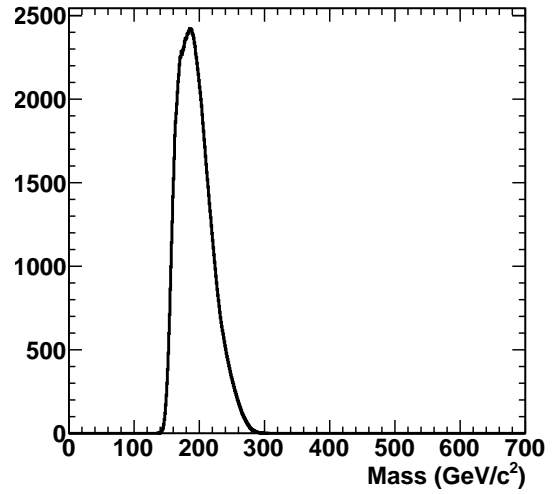
	p _T	η	φ	E
e ⁺	31.77	-1.01	-2.01	49.59
μ ⁻	27.58	-1.00	1.32	42.62
Jet 1	56.10	0.86	-2.72	78.72
Jet 2	34.22	-1.00	0.33	53.34
E _T	23.23		0.43	



Run: 149181
 Lumi Section: 1854
 Event: 1742001447

Peak Mass: 186 GeV/c²
 Peak Weight: 2422.31
 b-tagged Jets: 2

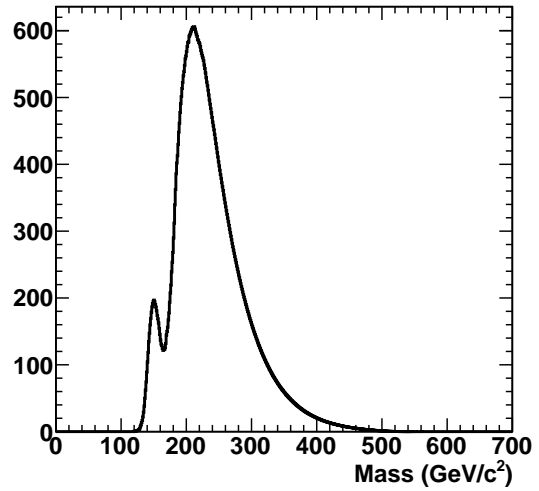
	p _T	η	φ	E
μ ⁺	45.22	0.54	-1.18	51.99
μ ⁻	32.07	1.26	-0.25	60.97
Jet 1	81.76	0.19	-3.00	84.34
Jet 2	62.69	-0.20	2.01	64.60
E _T	33.63		0.20	



Run: 149181
 Lumi Section: 245
 Event: 68403528

Peak Mass: 211 GeV/c²
 Peak Weight: 605.68
 b-tagged Jets: 2

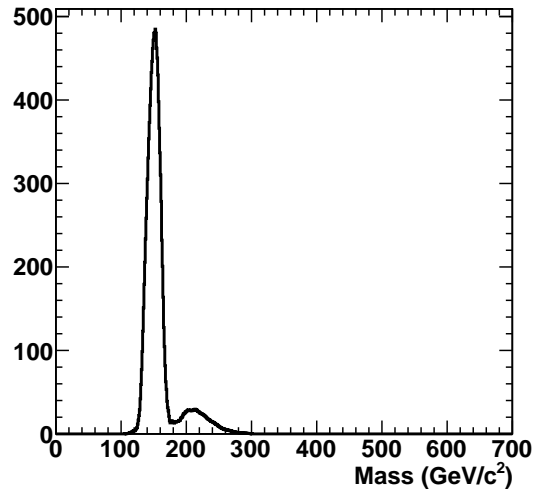
	p _T	η	φ	E
e ⁺	34.17	0.90	1.30	49.08
μ ⁻	37.40	-0.53	-0.70	42.83
Jet 1	120.04	-0.59	1.82	142.80
Jet 2	79.38	-0.38	-1.48	86.10
E _T	63.34		-2.09	



Run: 149181
 Lumi Section: 253
 Event: 80693186

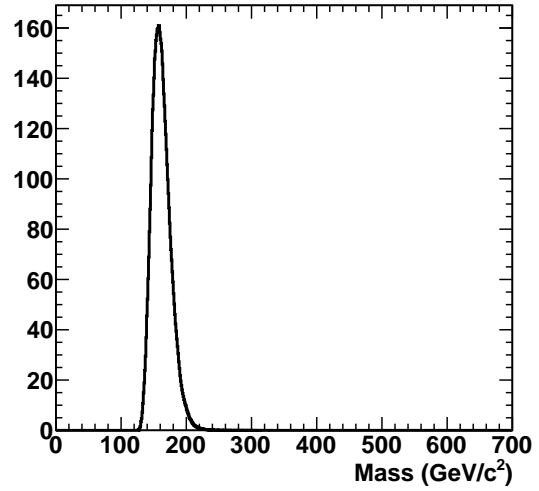
Peak Mass: 152 GeV/c²
 Peak Weight: 484.89
 b-tagged Jets: 2

	p _T	η	φ	E
μ ⁺	23.19	-0.38	-2.46	24.89
μ ⁻	75.98	0.26	2.51	78.62
Jet 1	104.70	-0.09	1.44	105.63
Jet 2	49.31	-0.69	-1.90	61.84
E _T	98.65		-1.57	



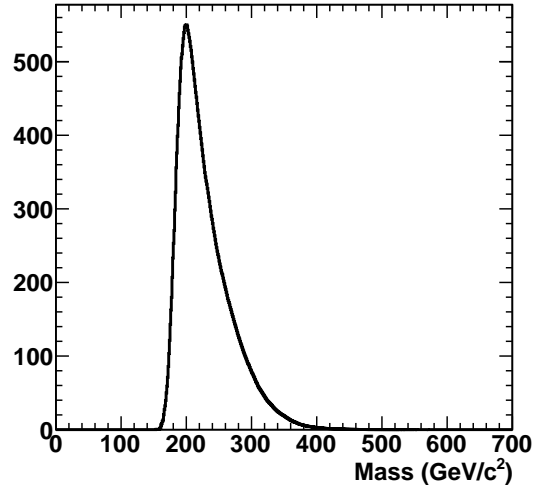
Run: 149181
 Lumi Section: 512
 Event: 436588272
 Peak Mass: 158 GeV/c²
 Peak Weight: 160.95
 b-tagged Jets: 1

	p _T	η	φ	E
μ ⁺	93.90	-1.09	-1.72	155.05
μ ⁻	126.79	-1.16	1.42	221.26
Jet 1	174.97	-1.78	-1.73	533.44
Jet 2	43.37	-1.30	2.70	85.64
E _T	69.10		1.23	



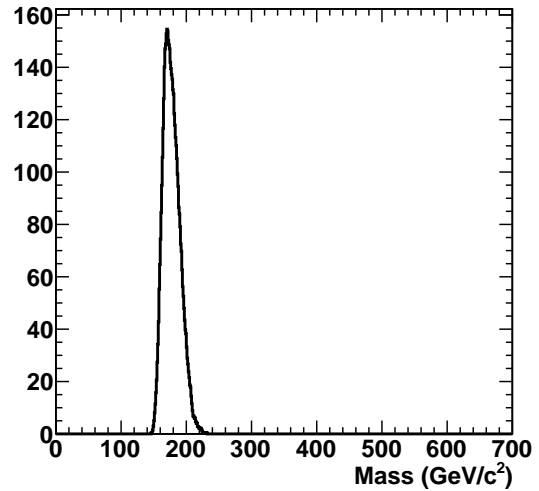
Run: 149181
 Lumi Section: 754
 Event: 723595683
 Peak Mass: 200 GeV/c²
 Peak Weight: 550.02
 b-tagged Jets: 1

	p _T	η	φ	E
e ⁺	48.51	0.12	-1.86	48.83
μ ⁻	57.59	0.69	1.82	71.68
Jet 1	88.36	0.88	0.20	125.40
Jet 2	93.61	-1.05	-1.46	150.63
E _T	96.44		2.30	



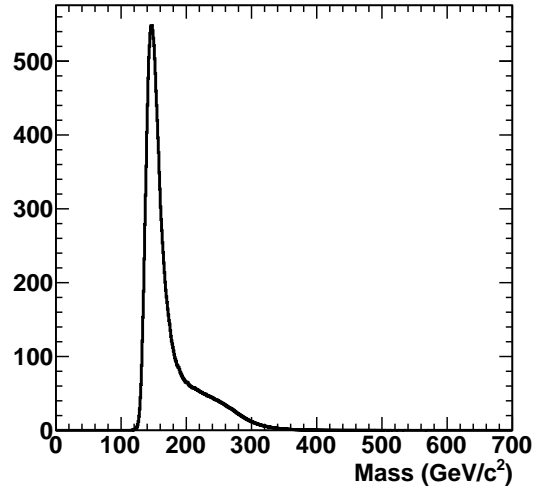
Run: 149181
 Lumi Section: 769
 Event: 740703741
 Peak Mass: 170 GeV/c²
 Peak Weight: 154.57
 b-tagged Jets: 2

	p _T	η	φ	E
μ ⁺	52.78	-0.70	2.96	66.15
μ ⁻	59.88	0.98	-2.80	91.02
Jet 1	118.76	0.35	-2.31	127.21
Jet 2	66.77	0.41	0.55	74.26
E _T	60.74		0.13	



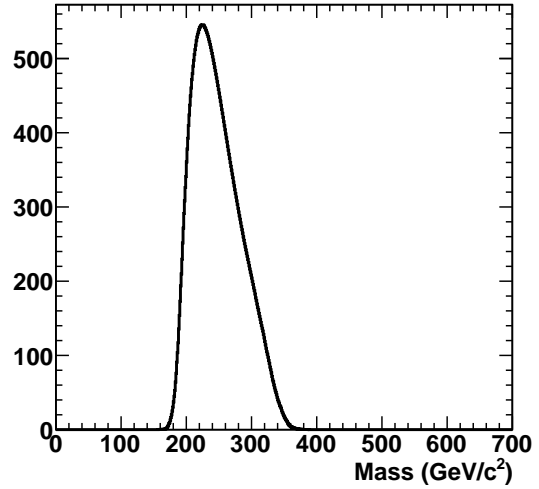
Run: 149182
 Lumi Section: 26
 Event: 21483106
 Peak Mass: 146 GeV/c²
 Peak Weight: 548.14
 b-tagged Jets: 0

	p _T	η	φ	E
e ⁺	44.58	0.44	-0.03	49.03
μ ⁻	73.84	-0.68	-3.01	91.36
Jet 1	41.59	2.11	0.50	173.62
Jet 2	37.62	-0.33	0.89	40.15
E _T	22.08		-2.61	



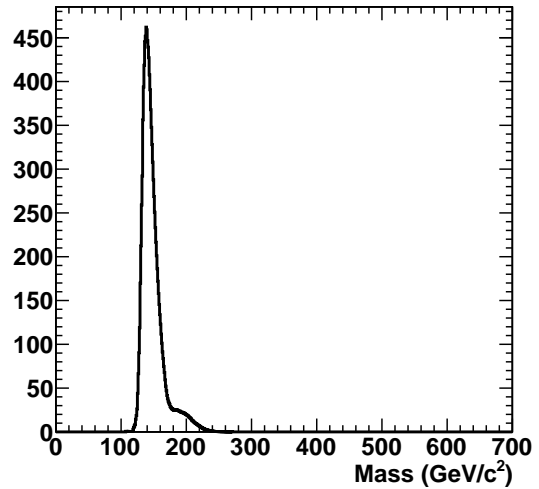
Run: 149182
 Lumi Section: 60
 Event: 51319857
 Peak Mass: 225 GeV/c²
 Peak Weight: 545.36
 b-tagged Jets: 0

	p _T	η	φ	E
μ ⁺	26.69	-1.12	0.83	45.08
μ ⁻	42.11	-2.04	0.72	164.22
Jet 1	66.88	0.29	-0.36	71.01
Jet 2	36.31	1.84	2.79	118.03
E _T	66.50		-2.39	



Run: 149291
 Lumi Section: 362
 Event: 387551026
 Peak Mass: 138 GeV/c²
 Peak Weight: 462.08
 b-tagged Jets: 1

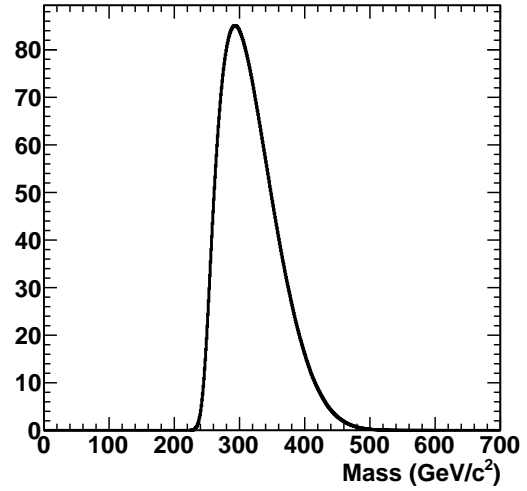
	p _T	η	φ	E
μ ⁺	25.44	0.44	-2.20	27.96
e ⁻	32.05	-2.49	-2.95	195.51
Jet 1	53.77	-2.03	2.29	207.82
Jet 2	30.46	-0.83	1.13	41.76
E _T	121.25		-0.65	



Run: 149291
 Lumi Section: 430
 Event: 460704901

Peak Mass: 293 GeV/c^2
 Peak Weight: 85.08
 b-tagged Jets: 1

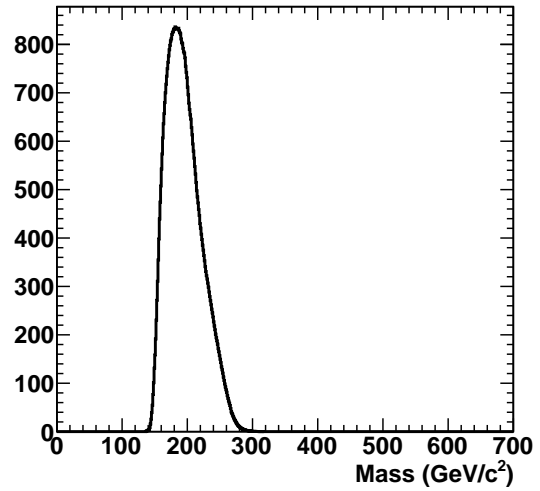
	p_T	η	ϕ	E
e^+	54.74	-1.47	1.81	125.23
e^-	118.52	-1.74	-0.76	348.44
Jet 1	122.07	0.72	1.45	157.10
Jet 2	153.43	-0.93	-2.37	226.57
\cancel{E}_T	53.86		1.49	



Run: 149291
 Lumi Section: 664
 Event: 683687535

Peak Mass: 181 GeV/c^2
 Peak Weight: 836.25
 b-tagged Jets: 1

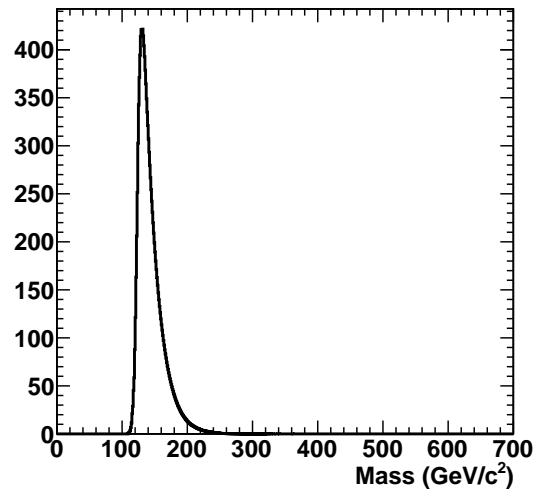
	p_T	η	ϕ	E
e^+	22.63	2.01	-1.75	85.60
μ^-	83.25	1.33	-1.10	168.39
Jet 1	30.50	-0.77	1.61	40.96
Jet 2	31.09	-0.31	0.38	33.74
\cancel{E}_T	65.26		2.61	



Run: 149291
 Lumi Section: 683
 Event: 700663787

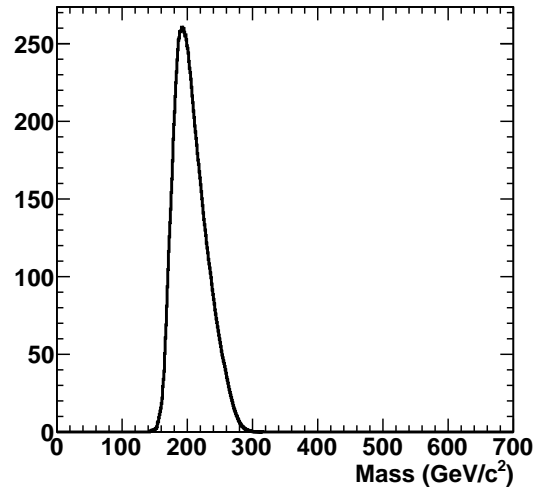
Peak Mass: 131 GeV/c^2
 Peak Weight: 421.46
 b-tagged Jets: 1

	p_T	η	ϕ	E
e^+	150.95	-0.22	1.79	154.48
μ^-	49.51	0.69	-1.03	61.70
Jet 1	100.23	-0.15	-1.08	102.29
Jet 2	34.66	0.22	0.84	36.86
\cancel{E}_T	74.79		-2.23	



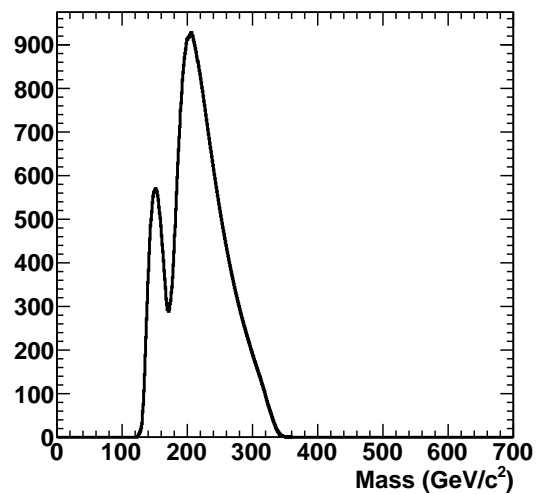
Run: 149291
 Lumi Section: 751
 Event: 759541584
 Peak Mass: 191 GeV/c^2
 Peak Weight: 260.60
 b-tagged Jets: 2

	p_T	η	ϕ	E
e^+	21.20	-2.13	2.44	90.39
μ^-	48.37	-1.52	2.90	115.75
Jet 1	173.33	-0.66	-2.44	213.41
Jet 2	90.57	-1.06	-0.42	147.13
\cancel{E}_T	123.65		0.77	



Run: 149291
 Lumi Section: 89
 Event: 37887806
 Peak Mass: 206 GeV/c^2
 Peak Weight: 928.19
 b-tagged Jets: 2

	p_T	η	ϕ	E
e^+	42.47	0.78	-2.57	55.97
μ^-	35.24	-0.05	2.22	35.29
Jet 1	99.02	0.47	-1.99	110.83
Jet 2	73.97	-1.03	2.78	116.92
\cancel{E}_T	78.76		0.45	



Bibliography

- [1] K. Nakamura et al. (Particle Data Group) *J. Phys. G* **37** (2010) 075021.
- [2] D. Griffiths, *Introduction to Elementary Particles*. Wiley & Sons, USA, 1987.
- [3] F. Halzen and A. Martin, *Quarks and Leptons: An Introductory Course in Modern Particle Physics*. Wiley & Sons, USA, 1984.
- [4] **CDF, D0** Collaboration, Tevatron Electroweak Working Group, “Combination of CDF and D0 Results on the Mass of the Top Quark,” [arXiv:1007.3178](#) [hep-ex].
- [5] C. Degrande, J.-M. Gerard, C. Grojean, F. Maltoni, and G. Servant, “Non-resonant New Physics in Top Pair Production at Hadron Colliders,” *JHEP* **03** (2011) 125, [arXiv:1010.6304](#) [hep-ph].
- [6] J. M. Campbell and R. K. Ellis, “MCFM for the Tevatron and the LHC,” [arXiv:1007.3492](#) [hep-ph].
- [7] N. Kidonakis, “Next-to-next-to-leading soft-gluon corrections for the top quark cross section and transverse momentum distribution,” *Phys. Rev.* **D82** (2010) 114030.
- [8] “Combination of top pair production cross sections in pp collisions at 7 TeV and comparisons with theory,” *CMS PAS TOP-11-001* (2011) .

- [9] **CMS** Collaboration, S. Chatrchyan *et al.*, “Measurement of the Top-antitop Production Cross Section in pp Collisions at $\sqrt{s} = 7$ TeV using the Kinematic Properties of Events with Leptons and Jets,” [arXiv:1106.0902](#) [[hep-ex](#)].
- [10] **D0** Collaboration, V. M. Abazov *et al.*, “Determination of the width of the top quark,” *Phys. Rev. Lett.* **106** (2011) 022001, [arXiv:1009.5686](#) [[hep-ex](#)].
- [11] F. Maltoni and T. Stelzer, “MadEvent: Automatic event generation with MadGraph,” *JHEP* **02** (2003) 027, [arXiv:hep-ph/0208156](#).
- [12] T. Sjöstrand, S. Mrenna, and P. Skands, “PYTHIA 6.4 physics and manual,” *JHEP* **05** (2006) 026, [arXiv:hep-ph/0603175](#).
- [13] **D0** Collaboration, V. Abazov *et al.*, “First measurement of the forward-backward charge asymmetry in top quark pair production,” *Phys.Rev.Lett.* **100** (2008) 142002, [arXiv:0712.0851](#) [[hep-ex](#)].
- [14] **CDF** Collaboration, T. Aaltonen *et al.*, “Forward-Backward Asymmetry in Top Quark Production in $p\bar{p}$ Collisions at $\sqrt{s} = 1.96$ TeV,” *Phys.Rev.Lett.* **101** (2008) 202001, [arXiv:0806.2472](#) [[hep-ex](#)].
- [15] **D0** Collaboration, “Measurement of the forward-backward production asymmetry of t and \bar{t} quarks in $pp \rightarrow t\bar{t}$ events,” *D0 Conference Note* **T90** .
- [16] **CDF** Collaboration, “Measurement of the Inclusive Forward-Backward Asymmetry and its Rapidity Dependence $A_{fb}(\Delta y)$ in $t\bar{t}$ Production in $5.3 fb^{-1}$ of Tevatron Data,” *CDF Conference Note* **10224** .
- [17] **CMS** Collaboration, “Measurement of the charge asymmetry in top quark pair production with the CMS experiment,” *CMS PAS* **TOP-10-010** (2011) .

- [18] **D0** Collaboration, V. M. Abazov *et al.*, “Measurement of spin correlation in $t\bar{t}$ production using a matrix element approach,” *Phys.Rev.Lett.* **107** (2011) 032001, arXiv:1104.5194 [hep-ex].
- [19] **The CDF** Collaboration, T. Aaltonen *et al.*, “Measurement of W –Boson Polarization in Top-quark Decay in $p\bar{p}$ Collisions at $\sqrt{s} = 1.96$ TeV,” *Phys. Rev. Lett.* **105** (2010) 042002, arXiv:1003.0224 [hep-ex].
- [20] **D0** Collaboration, V. M. Abazov *et al.*, “Measurement of the W boson helicity in top quark decays using 5.4 fb^{-1} of $p\bar{p}$ collision data,” *Phys. Rev.* **D83** (2011) 032009, arXiv:1011.6549 [hep-ex].
- [21] C. Collaboration, *CMS Physics Technical Design Report Volume II: Physics Performance*. Technical Design Report CMS. CERN, Geneva, 2006.
- [22] **CDF** Collaboration, T. Aaltonen *et al.*, “Search for the Flavor Changing Neutral Current Decay $t \rightarrow Zq$ in $p\bar{p}$ Collisions at $\sqrt{s} = 1.96$,” *Phys. Rev. Lett.* **101** (2008) 192002, arXiv:0805.2109 [hep-ex].
- [23] **D0** Collaboration, V. M. Abazov *et al.*, “Search for flavor changing neutral currents in decays of top quarks,” *Phys. Lett.* **B701** (2011) 313–320, arXiv:1103.4574 [hep-ex].
- [24] **CDF** Collaboration, T. Aaltonen *et al.*, “Search for top-quark production via flavor-changing neutral currents in $W+1$ jet events at CDF,” *Phys. Rev. Lett.* **102** (2009) 151801, arXiv:0812.3400 [hep-ex].
- [25] **CDF** Collaboration, F. Abe *et al.*, “Observation of top quark production in $p\bar{p}$ collisions,” *Phys. Rev. Lett.* **74** (1995) 2626, arXiv:hep-ex/9503002.
- [26] **D0** Collaboration, S. Abachi *et al.*, “Observation of the top quark,” *Phys. Rev. Lett.* **74** (1995) 2632, arXiv:hep-ex/9503003.

- [27] **ALEPH** Collaboration, “Precision Electroweak Measurements and Constraints on the Standard Model,” [arXiv:1012.2367](https://arxiv.org/abs/1012.2367) [hep-ex].
- [28] **UA1** Collaboration, C. Albajar *et al.*, “Search for $B_0 - \bar{B}_0$ oscillations at the CERN proton-antiproton collider. oai:cds.cern.ch:173668,” *Phys. Lett. B* **186** no. CERN-EP-86-209, (Dec, 1986) 247–254. 16 p.
- [29] **ARGUS** Collaboration, H. Albrecht *et al.*, “Observation of B_0 - anti- B_0 Mixing,” *Phys. Lett.* **B192** (1987) 245.
- [30] J. R. Ellis, J. Hagelin, and S. Rudaz, “Reexamination of the Standard Model in the Light of B Meson Mixing,” *Phys.Lett.* **B192** (1987) 201.
- [31] P. Antilogus, “A combination of preliminary LEP electroweak measurements and constraints on the standard model,” *CERN-PPE-95-172. CERN-L3-088* (Nov, 1995) .
- [32] B. Jacobsen, “Top mass from electroweak measurements,” *CERN-PPE-94-97. CERN-ALEPH-PUB-94-149* (Jun, 1994) 8 p, [arXiv:hep-ex/9407002](https://arxiv.org/abs/hep-ex/9407002).
- [33] **CDF** Collaboration, A. Abulencia *et al.*, “Precision top quark mass measurement in the lepton + jets topology in p anti-p collisions at $s^{*(1/2)} = 1.96$ -TeV,” *Phys. Rev. Lett.* **96** (2006) 022004, [arXiv:hep-ex/0510049](https://arxiv.org/abs/hep-ex/0510049).
- [34] **D0** Collaboration, V. Abazov *et al.*, “Measurement of the top quark mass in the lepton+jets channel using the Ideogram Method,” *Phys. Rev.* **D75** (2007) 092001, [arXiv:hep-ex/0702018](https://arxiv.org/abs/hep-ex/0702018).
- [35] **D0** Collaboration, V. M. Abazov *et al.*, “A precision measurement of the mass of the top quark,” *Nature* **429** (2004) 638–642, [arXiv:hep-ex/0406031](https://arxiv.org/abs/hep-ex/0406031).

- [36] **CDF** Collaboration, A. Abulencia *et al.*, “Precision top quark mass measurement in the lepton + jets topology in p anti-p collisions at $\sqrt{s} = 1.96$ -TeV,” *Phys. Rev. Lett.* **96** (2006) 022004, [arXiv:hep-ex/0510049](#).
- [37] **CDF** Collaboration, F. Abe *et al.*, “First observation of the all hadronic decay of t anti-t pairs,” *Phys. Rev. Lett.* **79** (1997) 1992–1997.
- [38] **D0** Collaboration, V. M. Abazov *et al.*, “Measurement of the top quark mass in all-jet events,” *Phys. Lett.* **B606** (2005) 25–33, [arXiv:hep-ex/0410086](#).
- [39] **CDF** Collaboration, T. Aaltonen *et al.*, “Measurement of the top-quark mass in all-hadronic decays in p anti-p collisions at CDF II,” *Phys. Rev. Lett.* **98** (2007) 142001, [arXiv:hep-ex/0612026](#).
- [40] **CDF** Collaboration, T. Aaltonen *et al.*, “Top Quark Mass Measurement in the t anti-t All Hadronic Channel using a Matrix Element Technique in p anti-p Collisions at $\sqrt{s} = 1.96$ -TeV,” *Phys. Rev.* **D79** (2009) 072010, [arXiv:0811.1062 \[hep-ex\]](#).
- [41] **The CDF** Collaboration, T. Aaltonen *et al.*, “Measurement of the Top Quark Mass and $p\bar{p} \rightarrow t\bar{t}$ Cross Section in the All-Hadronic Mode with the CDFII Detector,” *Phys. Rev.* **D81** (2010) 052011, [arXiv:1002.0365 \[hep-ex\]](#).
- [42] **D0** Collaboration, V. M. Abazov *et al.*, “Measurement of $t\bar{t}$ production in the $\tau + jets$ topology using $p\bar{p}$ collisions at $\sqrt{s} = 1.96$ TeV,” *Phys. Rev. D* **82** no. 7, (Oct, 2010) 071102.
- [43] **CDF** Collaboration, T. Aaltonen *et al.*, “Measurement of the top quark mass with dilepton events selected using neuroevolution at CDF,” *Phys. Rev. Lett.* **102** (2009) 152001, [arXiv:0807.4652 \[hep-ex\]](#).

- [44] **D0** Collaboration, V. M. Abazov *et al.*, “Precise measurement of the top quark mass in the dilepton channel at D0,” [arXiv:1105.0320 \[hep-ex\]](#).
- [45] **CDF** Collaboration, F. Abe *et al.*, “Measurement of the top quark mass and t anti-t production cross-section from dilepton events at the collider detector at Fermilab,” *Phys. Rev. Lett.* **80** (1998) 2779–2784, [arXiv:hep-ex/9802017](#).
- [46] **D0** Collaboration, B. Abbott *et al.*, “Measurement of the top quark mass using dilepton events,” *Phys.Rev.Lett.* **80** (1998) 2063–2068, [arXiv:hep-ex/9706014 \[hep-ex\]](#).
- [47] **CDF** Collaboration, F. Abe *et al.*, “Measurement of the top quark mass with the collider detector at Fermilab,” *Phys.Rev.Lett.* **82** (1999) 271–276, [arXiv:hep-ex/9810029 \[hep-ex\]](#).
- [48] **CDF** Collaboration, A. Abulencia *et al.*, “Measurement of the top quark mass using template methods on dilepton events in proton antiproton collisions at $\sqrt{s} = 1.96$ TeV.,” *Phys.Rev.* **D73** (2006) 112006, [arXiv:hep-ex/0602008 \[hep-ex\]](#).
- [49] **D0** Collaboration, V. M. Abazov *et al.*, “Measurement of the top quark mass in final states with two leptons,” *Phys. Rev.* **D80** (2009) 092006, [arXiv:0904.3195 \[hep-ex\]](#).
- [50] CERN Communications Group, “CERN FAQ: LHC the Guide,” *CERN-Brochure-2008-001-Eng* **January 2008** .
- [51] O. S. Brning, P. Collier, P. Lebrun, S. Myers, R. Ostojic, J. Poole, and P. Proudlock, *LHC Design Report*. CERN, Geneva, 2004.
- [52] C. Collaboration, “The CMS experiment at the CERN LHC,” *JINST* **3** (2008) .

- [53] CMS Collaboration, S. Chatrchyan *et al.*, “Performance of the CMS Hadron Calorimeter with Cosmic Ray Muons and LHC Beam Data,” *JINST* **5** (2010) T03012, [arXiv:0911.4991](#) [[physics.ins-det](#)].
- [54] M. L. Mangano, M. Moretti, F. Piccinini, R. Pittau, and A. D. Polosa, “ALPGEN, a generator for hard multiparton processes in hadronic collisions,” *JHEP* **07** (2003) 001, [arXiv:hep-ph/0206293](#).
- [55] S. Frixione, P. Nason, and C. Oleari, “Matching NLO QCD computations with parton shower simulations: the POWHEG method,” *JHEP* **11** (2007) 070, [arXiv:0709.2092](#) [[hep-ph](#)].
- [56] S. Hoche *et al.*, “Matching parton showers and matrix elements,” [arXiv:hep-ph/0602031](#).
- [57] N. Davidson, G. Nanava, T. Przedzinski, E. Richter-Was, and Z. Was, “Universal interface of TAUOLA technical and physics documentation,” [arXiv:1002.0543](#) [[hep-ph](#)].
- [58] G. Corcella *et al.*, “HERWIG 6.5 release note,” [arXiv:hep-ph/0210213](#).
- [59] J. Allison *et al.*, “Geant4 developments and applications,” *IEEE Trans. Nucl. Sci.* **53** (2006) 270.
- [60] G. Petrucciani *et al.*, “PAT: the CMS Physics Analysis Toolkit,” *CR* **2009-083**.
- [61] Field, Rick, “Early LHC underlying event data - findings and surprises,” [arXiv:1010.3558](#) [[hep-ph](#)].
- [62] CMS Collaboration, V. Khachatryan *et al.*, “CMS Tracking Performance Results from early LHC Operation,” *Eur.Phys.J.* **C70** (2010) 1165–1192, [arXiv:1007.1988](#) [[physics.ins-det](#)].

- [63] CMS Collaboration, S. Chatrchyan *et al.*, “Identification and Filtering of Uncharacteristic Noise in the CMS Hadron Calorimeter,” *JINST* **5** (2010) T03014, [arXiv:0911.4881 \[physics.ins-det\]](#).
- [64] CMS Collaboration, “Muon Reconstruction in the CMS Detector,” *CMS AN AN-08-097* (2009) .
- [65] R. Fruhwirth, “Application of Kalman filtering to track and vertex fitting,” *Nucl. Instrum. Meth.* **A262** (1987) 444–450.
- [66] CMS Collaboration, W. Adam, B. Mangano, T. Speer, and T. Todorov, “Track Reconstruction in the CMS Tracker,” *CMS Note-2006/041* (2006) .
- [67] CMS Collaboration, “Performance of muon identification in pp collisions at $\sqrt{s} = 7$ TeV,” *CMS PAS MUO-10-002* (2010) .
- [68] CMS Collaboration, “Commissioning of the Particle-flow Event Reconstruction with the first LHC collisions recorded in the CMS detector,” *CMS PAS PFT-10-001* (2010) .
- [69] S. Baffioni, C. Charlot, F. Ferri, D. Futyan, P. Meridiani, I. Puljak, C. Rovelli, R. Salerno, and Y. Sirois, “Electron reconstruction in CMS,”.
- [70] W. Adam, R. Fruhwirth, A. Strandlie, and T. Todorov, “Reconstruction of electrons with the Gaussian-sum filter in the CMS tracker at LHC,” *J. Phys. G* **31** (2005) N9.
- [71] CMS Collaboration, “Electron reconstruction and identification at $\sqrt{s} = 7$ TeV,” *CMS PAS EGM-10-004* (2010) .
- [72] CMS Collaboration, “Particle-Flow Event Reconstruction in CMS and Performance for Jets, Taus, and MET,” *CMS PAS PFT-09-001* (2009) .

- [73] M. Cacciari, G. P. Salam, and G. Soyez, “The anti- k_t jet clustering algorithm,” *JHEP* **04** (2008) 063, [arXiv:0802.1189 \[hep-ph\]](#).
- [74] CMS Collaboration, “Jet Energy Corrections determination at 7 TeV,” *CMS PAS JME-10-010* (2010) .
- [75] “Algorithms for b Jet identification in CMS,” *CMS PAS BTV-09-001* (2009) .
- [76] “Commissioning of b-jet identification with pp collisions at $\sqrt{s} = 7$ TeV,” *CMS PAS BTV-10-001* (2010) .
- [77] D0 Collaboration, V. M. Abazov *et al.*, “Measurement of the top quark mass in final states with two leptons,” *Phys. Rev.* **D80** (2009) 092006, [arXiv:0904.3195 \[hep-ex\]](#).
- [78] Sonnenschein, Lars , “Analytical solution of $t\bar{t}$ dilepton equations,” *Phys. Rev.* **D73** (2006) 054015, [arXiv:hep-ph/0603011](#).
- [79] Sonnenschein, Lars , “Erratum: Analytical solution of $t\bar{t}$ dilepton equations [Phys. Rev. **D73**, 054015 (2006)],” *Phys. Rev.* **D78** (2008) 079902.
- [80] Sonnenschein, Lars , “Algebraic approach to solve $t\bar{t}$ dilepton equations,” *Phys. Rev.* **D72** no. 9, (2005) 095020, [arXiv:hep-ph/0510100](#).
- [81] Dalitz, R. H. and Goldstein, Gary R., “Decay and polarization properties of the top quark,” *Phys. Rev. D* **45** no. 5, (Mar, 1992) 1531–1543.
- [82] Pumplin, J. and others, “New generation of parton distributions with uncertainties from global QCD analysis,” *JHEP* **07** (2002) 012, [arXiv:hep-ph/0201195](#).
- [83] Whalley, M.R. and Bourilkov, D. and Group, R.C., “The Les Houches accord PDFs (LHAPDF) and LHAGLUE,” [arXiv:hep-ph/0508110 \[hep-ph\]](#).

- [84] “Jet Performance in pp Collisions at 7 TeV,” *CMS PAS JME-10-003* (2010) .
- [85] CMS Collaboration, V. Khachatryan *et al.*, “First Measurement of the Cross Section for Top-Quark Pair Production in Proton-Proton Collisions at $\sqrt{s} = 7$ TeV,” *Phys. Lett.* **B695** (2011) 424, [arXiv:1010.5994 \[hep-ex\]](#) .
- [86] F. James *et al.*, “MINUIT,”
<http://seal.web.cern.ch/seal/work-packages/mathlibs/minuit/index.html> .
- [87] “Jet Energy Resolution in CMS at $\sqrt{s} = 7$ TeV,” *CMS PAS JME-10-014* (2011) .
- [88] CMS Collaboration, CMS Collaboration, “Missing transverse energy performance of the cms detector.,” [arXiv:1106.5048 \[hep-ex\]](#) .
- [89] “Private communication with a convener of the CMS *b*-tagging and vertexing Physics Object Group. Our uncertainty on *b*-tagging is conservative.” 2010.
- [90] P. Biallass *et al.*, “Parton Distribution Uncertainty Determination within CMSSW,” *CMS AN* **2009/048** (2009) .
- [91] CMS Collaboration, S. Chatrchyan *et al.*, “Measurement of the $t\bar{t}$ production cross section and the top quark mass in the dilepton channel in pp collisions at $\sqrt{s} = 7$ TeV,” *Accepted by JHEP* (2011) , [arXiv:1105.5661 \[hep-ex\]](#) .
- [92] L. Lyons, D. Gibaut, and P. Clifford, “How to combine correlated estimates of a single physical quantity,” *Nucl. Instrum. Meth.* **A270** (1988) 110.
<http://www.sciencedirect.com/science/article/B6TJM-473DBY1-M/2/b585b7c1896787399c53868631a2376c>.
- [93] “Measurement of the top quark mass in the l+jets channel,” *CMS PAS TOP-10-009* (2011) .